

# Turbulent premixed combustion: Flamelet structure and its effect on turbulent burning velocities

James F. Driscoll\*

*Department of Aerospace Engineering, University of Michigan, Ann Arbor, MI 48109-2140, USA*

Received 16 June 2006; accepted 19 April 2007

Available online 20 July 2007

---

## Abstract

This review paper addresses the following question: what is the structure of flamelets within premixed turbulent combustion and how does this structure affect the turbulent burning velocity? We also ask: how accurately can new models predict the flamelet structure as well as the values of turbulent burning velocity? Flamelet structure is defined to include the following quantities: reaction layer surface area per unit volume ( $\Sigma$ ), the brush thickness ( $\delta_T$ ) and the stretch factor ( $I_0$ ). One equation that is commonly used to relate these flamelet structure parameters to the burning velocity  $S_T$  is

$$\frac{S_T}{S_{L0}} = I_0 \int_{-\infty}^{\infty} \Sigma d\eta = I_0 \Sigma_{\max} \delta_T.$$

Recent results obtained using laser imaging methods and direct numerical simulation (DNS) are reviewed in order to demonstrate the relationships between  $S_T$ ,  $\Sigma$ ,  $I_0$  and  $\delta_T$ .  $\eta$  is the direction normal to the brush. Measurements of  $\Sigma$  show that the wrinkling process is not local but has a “memory” of wrinkling that occurs elsewhere. The stretch factor  $I_0$  depends on differential diffusion (Markstein number) even at large turbulence intensities. Thus the concepts associated with the theory of flame stretch have been found to be valid even for highly turbulent flames. Thin flamelets exist for nearly all cases for which images of the reaction zone have been obtained. Evidence of “non-flamelet” behavior is sparse. DNS now can successfully predict realistic values of turbulent burning velocity for laboratory-scale Reynolds numbers and for the realistic geometries of Bunsen and V-flames using complex chemistry and no empirical constants. Large eddy simulations (LES) also have predicted reasonable values of  $S_T$ , but some empirical constants are required. A number of current research issues are discussed.

© 2007 Elsevier Ltd. All rights reserved.

**Keywords:** Turbulent; Premixed; Combustion; Burning velocity; Flamelet

---

## Contents

1. Introduction: Why do we need to know the structure of premixed turbulent combustion?	92
1.1. General concepts: flamelet wrinkling by flame–vortex interactions	96
1.2. Turbulent burning velocities—definitions	98
2. Images of thin flamelets	99
2.1. Flamelets exist for Karlovitz numbers exceeding ten	103
2.2. Images of flame–eddy interactions in turbulent flames	105
3. Flamelet structure ( $\Sigma$ , $\delta_T$ )	107
3.1. Surface density ( $\Sigma$ )—measurements and DNS computations	107
3.2. Brush thickness ( $\delta_T$ )	112
3.3. Surface area of flamelets—proportional to turbulent burning velocity?	113

\*Tel.: +1 734 936 0101; fax: +1 734 763 0578.

E-mail address: [jamesfd@umich.edu](mailto:jamesfd@umich.edu)

4.	How well can we predict the turbulent burning velocity? . . . . .	113
4.1.	Burning velocities predicted by DNS . . . . .	113
4.2.	Burning velocities predicted by LES and the CFM . . . . .	115
4.3.	Thermodiffusive (Markstein number) effects and the stretch factor $I_0$ . . . . .	119
4.4.	What turbulent burning velocity measurements to use for model assessment? . . . . .	122
5.	Some research issues . . . . .	125
6.	Conclusions . . . . .	131
	Acknowledgments . . . . .	131
	References . . . . .	131

---

## 1. Introduction: Why do we need to know the structure of premixed turbulent combustion?

We begin our discussion with the question: why do we need to know the structure of the flamelets that exist within turbulent premixed flames? The word “structure” here refers to quantities such as  $\Sigma$ ,  $\delta_T$  and  $I_0$ , which are defined to be the flamelet surface area per unit volume, the brush thickness, and a stretch factor that is defined below. The answer to our question is that we need to know the structure because the turbulent burning velocity  $S_T$  depends on the flamelet wrinkling process which is geometry-dependent. That is, in real flames the wrinkling is not some “universal” process that depends only on the local turbulence level. Instead wrinkling depends on the complex geometry of shear layers, walls, flame-flame interactions and the location where the flame is anchored. Wrinkling has a “memory” of any wrinkling that might have occurred upstream. Therefore, models must be able to use differential equations to relate the wrinkling process to the burner geometry. Measurements of  $\Sigma$ ,  $\delta_T$  and  $I_0$  are needed to determine if direct numerical simulation (DNS) or large eddy simulation (LES) can accurately predict these quantities using no adjustable parameters or a few parameters, respectively. For a model to be considered to be robust is not sufficient to show that the predicted burning velocity matches an experiment by adjusting some parameters. A robust simulation must predict the correct intermediate parameters such as  $\Sigma$  and  $\delta_T$  as well as  $S_T$ .

One may ask: is it possible for any model to correctly predict the complex wrinkling process that occurs a real burner that is operated at a realistic Reynolds number? Fortunately new advances in DNS and LES provide a positive answer to that question.

**Fig. 1** illustrates DNS results of Bell et al. [1,2] and Sankaran et al. [3]. Also shown are LES computations of Pitsch and Duchamp de Lagenest [4]. The DNS studies used no adjustable parameters and were able to include complex methane-air chemistry with 20 species and 84 reactions, realistic burner dimensions (from 1 to 5 cm) and realistic Reynolds numbers that are associated with laboratory-scale burners operated at mean velocities of 3–60 m/s. Values of  $u'/S_{L0}$  varied between 0.69 and 10; this is sufficient to cause the extreme degree of wrinkling that is seen in **Fig. 1**. The DNS and LES results are discussed in Section 4.

An important equation that relates the turbulent burning velocity to the flamelet structure is one that has been discussed by Bray and Cant [5]:

$$\frac{S_T}{S_{L0}} = I_0 \int_{-\infty}^{\infty} \Sigma d\eta. \quad (1)$$

The coordinate  $\eta$  is normal to the brush, and the integral in Eq. (1) is proportional to the product of the maximum value of  $\Sigma$  (which occurs near the center of the brush) and the brush thickness  $\delta_T$ . This equation indicates that to achieve a rapidly propagating turbulent flame, it is desirable to have a large value of the product of the maximum surface density and the brush thickness.

Because of the importance of Eq. (1) its derivation is briefly reviewed. Damköhler [6] predicted that for one regime of conditions (which is now called the flamelet regime) the primary result of turbulence is to wrinkle the thin reaction layers, which retain the local characteristics of a laminar flame. For this regime he predicted that the ratio of turbulent to laminar burning velocity ( $S_T/S_{L0}$ ) is equal to the area ratio ( $A_T/A_L$ ). **Fig. 2** illustrates the areas  $A_T$  and  $A_L$  of a wrinkled and an unwrinkled flamelet, respectively. In **Fig. 2** each point along the wrinkled surface propagates at the flamelet consumption speed  $S_{F,C}$  which has a time-averaged value of  $\bar{S}_{F,C}$ . The time-averaged volume per second of reactants that is traversed by a flamelet is  $\bar{S}_{F,C} A_T$ . The reactants have the constant density  $\rho_R$ . Therefore, the mass per second of reactants traversed by the wrinkled surface inside the control volume is  $\rho_R \bar{S}_{F,C} A_T$ . Now consider the dotted line in **Fig. 2**; it propagates at the turbulent burning velocity  $S_T$ . The volume of reactants traversed per second by the dotted line is  $S_T A_L$  and the mass/s of reactants traversed is  $\rho_R S_T A_L$ . Equating these two values yields

$$\frac{S_T}{S_{L0}} = \frac{A_T}{A_L} \frac{\bar{S}_{F,C}}{S_{L0}} = \frac{A_T}{A_L} I_0. \quad (2)$$

Bray and Cant defined the stretch factor  $I_0$  and the flamelet consumption speed to be

$$I_0 = \bar{S}_{F,C}/S_{L0}, \quad S_{F,C} = \rho_R^{-1} \int \omega_R d\xi. \quad (3)$$

The instantaneous volumetric reaction rate is  $\omega_R$  and  $\xi$  is the direction normal to each reaction layer. A slice of the

## Nomenclature

$A_T$	area of wrinkled flame surface
$A_L$	area of unwrinkled flame surface (= area of $\bar{c} = 0.5$ surface)
$c$	reactedness = $(T - T_R)/(T_P - T_R)$
$D$	molecular diffusivity
$D_T$	turbulent diffusivity
$d$	eddy diameter
$I_0$	stretch factor, Eqs. (1)–(3)
$K$	stretch rate, Eq. (11)
$Ka$	Karlovitz number, Eq. (21)
$\ell$	streamwise integral scale
$Ma_L$	Markstein number of a laminar flame Eq. (35)
$Ma_F$	Markstein number of flamelet in a turbulent flame, Eq. (36)
$Ma_T$	turbulent Markstein number, Eq. (37)
$S_{F,C}$	local consumption speed of a flamelet, Eq. (3)
$S_{L0}$	laminar unstretched burning velocity
$S_{T,GC}$	turbulent burning velocity (global consumption speed), Eq. (15)

$S_{T,LC}$	turbulent burning velocity (local consumption speed), Eq. (16)
$S_{T,LD}$	turbulent burning velocity, (local displacement speed, Eq. (17))
$u'$	r.m.s. streamwise velocity fluctuation
$U$	mean streamwise velocity
$\alpha_0$	thermal diffusivity of reactants
$\delta_{L0}$	unstretched laminar flame thickness
$\delta_T$	turbulent brush thickness
$\delta_{PRE}$	preheat zone average thickness
$\delta_{CH}$	CH layer average thickness
$\eta$	coordinate normal to $\bar{c} = 0.5$ contour
$\Gamma_K$	stretch efficiency factor, Eq. (13)
$\lambda_{\min}$	minimum wrinkle wavelength
$\Sigma$	flame surface density
$\Sigma_{\max}$	surface density at center of brush
$\xi$	direction normal to the flamelet, Eq. (37)
$\omega_R$	volumetric mean reaction rate

## Subscripts

R	reactants
P	products

volume of the control volume ( $dV$ ) in Fig. 2 is  $(A_L d\eta)$ .  $A_T$  is

$$A_T = \int_{-\infty}^{\infty} \Sigma dV = \int_{-\infty}^{\infty} \Sigma (A_L d\eta). \quad (4)$$

Therefore, Eq. (1) is derived by combining Eqs. (2) and (4).

A major obstacle to progress in the field of premixed turbulent combustion has been the expectation that segments of real flames should have the properties of an ideal “geometry-independent” turbulent flame. A hypothetical ideal flame is shown in Fig. 3a; it is one for which the wrinkling process (and the resulting values of  $S_T$ ,  $\Sigma$  and  $\delta_T$ ) depend only on the local values of  $u'$  and integral scale just ahead of the segment of the brush where  $S_T$  is measured. For the ideal flame the following correlation is expected to hold:

$$\frac{S_T}{S_{L0}} = f\left(\frac{u'}{S_{L0}}, \frac{\ell}{\delta_{L0}}, Ma_T\right). \quad (5)$$

$Ma_T$  is the turbulent Markstein number that is defined below and  $S_{L0}$  is the unstretched laminar burning velocity. Eq. (5) often has been used to attempt to correlate measured values of burning velocity. It was assumed that the normalized burning velocities of segments along the brush of any type of flame (spherical, Bunsen, or rod-stabilized) are identical, as long as the values of  $u'/S_{L0}$ ,  $\ell/\delta_{L0}$  and  $Ma_T$  in front of the segments are the same.

However, experiments indicate that wrinkling process is “geometry-dependent” and has a “memory” of whatever wrinkling occurred at upstream locations.  $S_T$ ,  $I_0$ ,  $\Sigma$  and  $\delta_T$  normally vary in space (or time) and they depend on the geometry of the burner that is used. Fig. 3b and c represent

real Bunsen and spherical flames. Near the base region of the Bunsen flame it is found that there is less wrinkling (and a lower value of  $S_T$ ) than near the tip region, as described in Section 3.1. This difference is due to the boundary condition that requires the flame base to be anchored to the burner rim. Note that the values of  $u'$  and  $\ell$  may be nearly identical at the base and at the tip, yet the values of  $S_T$  are different, so the ideal “geometry-independent” correlation given by Eq. (5) cannot be valid. The degree of wrinkling at any streamwise  $x$ -location depends on the “memory” of wrinkling at upstream  $x$ -locations. For this reason, tall Bunsen flames that are stabilized on large diameter burners have more distance for wrinkling to occur, and become more wrinkled than short flames that are stabilized on small diameter burners. Thus burner size  $W$  can be an additional parameter. The spherically expanding flame in Fig. 3c often is subjected to a constant value of  $u'$  and  $\ell$  in the reactants, yet as time progresses the degree of wrinkling and the value of  $S_T$  both increase [11]. For the spherical flame the wrinkling process also has a memory. It follows that Eq. (5) is not sufficient; additional parameters should be added such as the non-dimensional burner width ( $W/\ell$ ) or time ( $t/(\ell/u')$ ) so that for a realistic geometry-dependent wrinkling process:

$$\frac{S_T}{S_{L0}} = f\left(\frac{u'}{S_{L0}}, \frac{\ell}{\delta_{L0}}, Ma_T, \frac{W}{\ell}, \text{ or } \frac{t}{(\ell/u')}\right). \quad (6)$$

One argument that is often heard is that experimentalists should create flames that are closer to the ideal case, such that wrinkling is “geometry-independent” and depends only on the local  $u'$  and  $\ell$  so that Eq. (5) is valid. There is

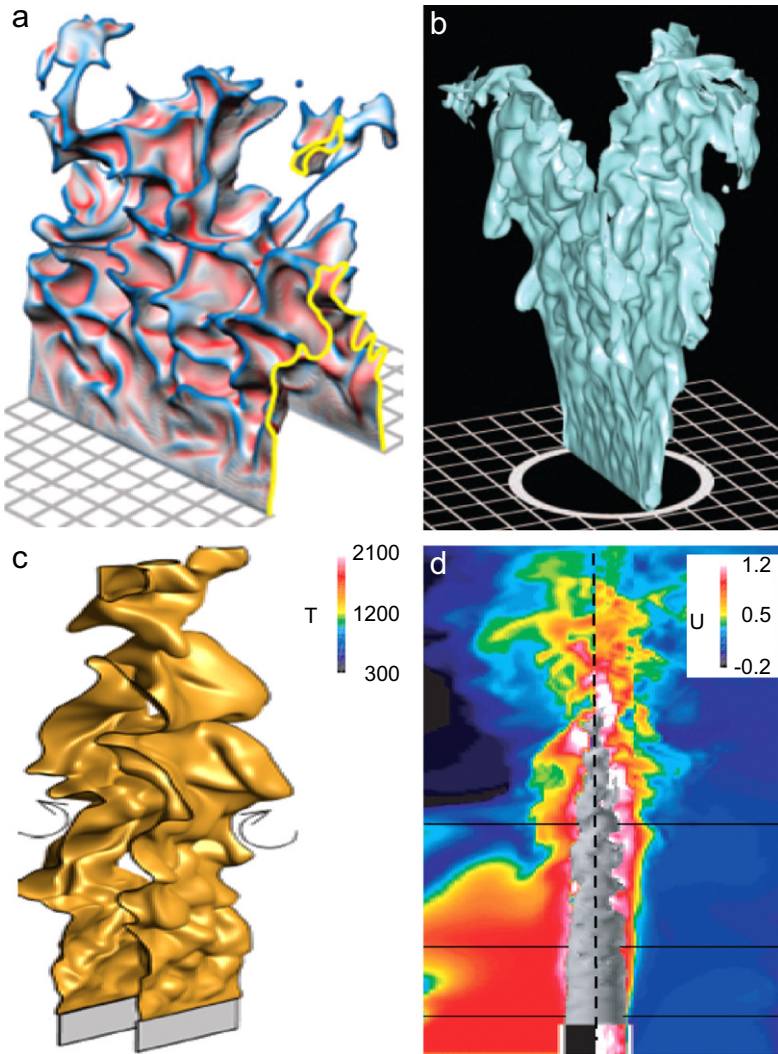


Fig. 1. DNS results of (a) Bell et al. [1], (b) Bell et al. [2] and (c) Sankaran et al. [3] for premixed turbulent Bunsen and V-flames. DNS now can simulate the realistic Reynolds numbers that are associated with laboratory-scale burners ( $2.5 \times 5.0 \text{ cm}$  [1]) and velocities of  $80 \text{ m/s}$  [3]) with complex methane chemistry and a grid of  $62\text{--}100 \mu\text{m}$  that resolves the Kolmogorov scale: (a)  $1684 \text{ K}$  isotherm, (b) isoline of temperature gradient =  $1000 \text{ K/mm}$ , (c) isocontour of reactedness =  $0.65$  and (d) LES of Pitsch and Duchamp de Lagenest [4] for complex methane chemistry,  $U = 30 \text{ m/s}$ ,  $u'/S_{L0} = 11.9$ . Left side = temperature in  $K$ , right side = axial velocity in  $\text{m/s}$ .

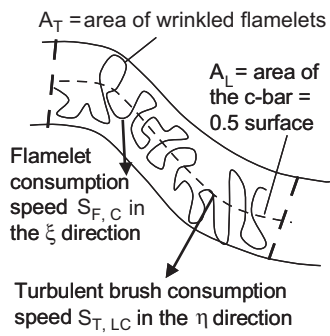


Fig. 2. Schematic of the wrinkled area ( $A_T$ ) and the area of the  $\bar{c} = 0.5$  contour ( $A_L$ ). Also labeled are the flamelet consumption speed ( $S_{F,C}$ ) and the turbulent brush local consumption speed ( $S_{T,LC}$ ).

no evidence to date that verifies that such conditions can be generated. Relatively flat turbulent flames can be created, but only by employing the diverging flow fields that are

found in counterflow [12], low-swirl [13], or diffuser type [14] burners. It has been speculated that the flame brush eventually will reach an equilibrium state and will no longer become thicker after a certain time (in the spherical case) or after a certain distance (in the Bunsen case). There is no evidence that such an equilibrium state has ever been achieved, and if it could be achieved it would not be representative of real engines. Instead it appears that the best strategy is to accept that real flames undergo “geometry-dependent” wrinkling and there is a need to develop numerical simulations that can handle each geometry separately. Cheng and Shepherd [13] have suggested the following names for the categories of premixed turbulent flames:

- (i) envelope flames: axisymmetric or 2-D Bunsen burners [15];
- (ii) oblique flames: V-flames [16];

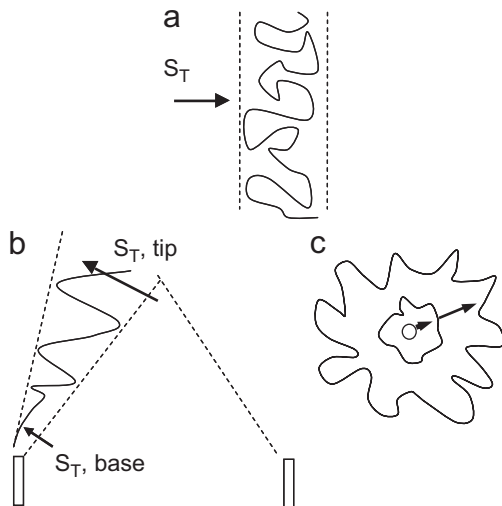


Fig. 3. Schematic of (a) a hypothetical “geometry-independent” wrinkled flamelet structure and (b, c) realistic “geometry-dependent” wrinkled structures that cause the burning velocity  $S_T$  to depend on the distance ( $x$ ) for the Bunsen geometry and the time ( $t$ ) for the spherical case.

- (iii) flat flames: low-swirl, counterflow, or diffusion burners [12–14];
- (iv) spherical flames: fan-stirred chambers [17].

It is recommended that a database of values of  $S_T$ ,  $I_0$ ,  $\Sigma$  and  $\delta_T$  be recorded for each category using measurements and DNS. Formulas for burning velocity such as Eq. (6) should be modified to include the parameters that are specific to that particular category. Only flames within a particular category should be compared, since the wrinkling processes associated with each category can be inherently different.

Since experiments indicate that flamelet wrinkling is “geometry-dependent”, it follows that models must be able to simulate wrinkling with realistic differential equations and not rely on empirical correlations. Table 1 lists some commonly used models and simulations. The flamelet-structure approach is defined to be the use of differential equations to obtain the flame surface density. Differential equations account for the fact that the wrinkling process has a “memory” of wrinkling that occurred at upstream locations. The flamelet-structure approach includes two Reynolds-averaged Navier Stokes (RANS) models. The coherent flamelet model (CFM) of Veynante et al. [18], Meneveau and Poinsot [19] and others [20–29] solves the flame surface density balance equation. The other RANS approach is that of Peters [30,31] who solves the  $G$ -equation. Also listed in Table 1 is LES; LES submodels that are based on the flame surface density equation were developed by Hawkes and Cant [32], Weller et al. [33] and Charlotte et al. [34]. An LES submodel that is based on the  $G$ -equation was developed by Pitsch [4,35]. DNS is another way to simulate the flame structure; DNS of an entire burner has been described by Bell et al. [1,2] and Sankaran et al. [3]. The ability of these simulations to provide

Table 1  
Models of premixed turbulent combustion

- |  |
|--|
| A. Models with no differential equation for $\Sigma$                   |
| 1. BML model with algebraic relation for $\Sigma$ [7]                  |
| 2. Stochastic particle/Monte Carlo concept [36]                        |
| 3. Fractal model of Lindstedt–Vaos [39]                                |
| 4. Zimont correlation model [37,38]                                    |
| B. Flamelet structure approach—differential equations predict $\Sigma$ |
| 1. Flame surface density balance (CFM/RANS or LES) [18,32]             |
| 2. $G$ -Equation models (RANS or LES) [4,30]                           |
| 3. Direct numerical simulation [1–3]                                   |

accurate predictions of the turbulent burning velocity is discussed in Section 4.

An advantage of flamelet-structure approach is that it provides predicted profiles of  $\Sigma$  and brush thickness that can be directly compared to experimental measurements. Comparing quantities such as  $\Sigma$  and  $\delta_T$  is a more sensitive test of a model than simply comparing mean temperature or velocity profiles. It is recommended that the following requirement be applied to the next generation of numerical models: the model cannot be considered to be realistic unless it can predict  $S_T$  as well as the measured structure, such as profiles of  $\Sigma$  and  $\delta_T$ .

The first four models listed in Table 1 that are classified as models that do not use differential equations to predict the spatial variations of the flamelet surface density. Bray et al. [7] assumed that the mean reaction rate is proportional to  $\Sigma$ . In some of their analysis they assumed that an algebraic relation is sufficient to relate  $\Sigma$  to the local turbulence properties. One version of their algebraic relation is

$$\Sigma = \ell^{-1} \frac{u'}{S_{L0}} \bar{c}(1 - \bar{c}) C_L. \quad (7)$$

Eq. (7) is based on the assumption that  $\Sigma$  depends only on the local integral scale  $\ell$  and local velocity fluctuations  $u'$ ; there is no memory of the wrinkling that occurred elsewhere. Wu and Bray [12] later replaced Eq. (7) with a differential equation for  $\Sigma$ . Another approach is one that employs stochastic particles [36]. Each stochastic particle is a “well-stirred reactor” that has a certain chemical residence time. The residence time is predicted by an equation for the mixing frequency that is based on some speculative ideas rather than the conservation equations of physics. The hope is that the time-averaged properties of these hypothetical stochastic particles in some way represent the true time-averaged properties of the actual fluid elements, even though the particles themselves do not obey the conservation laws. No attempt is made to incorporate the physics of the wrinkled flame surface or the stretching that is caused by vortices. The submodel developed by Zimont is included in the commercial design code FLUENT and is described in Refs. [37] and [38]. It is

based on the following empirical correlation:

$$\frac{S_T}{S_{L0}} = 1 + A \left( \frac{u'}{S_{L0}} \right)^{1/2} \left( \frac{u' \ell}{v} \right)^{1/4}. \quad (8)$$

While Eq. (8) is based on empirical correlations, it has been explained by some theoretical concepts [38].

The Lindstedt–Vaos model [39] is based on a different set of assumptions: the flamelets are assumed to be fractal and to have fractal dimension of  $\frac{7}{3}$ , the inner cutoff scale equals the Kolmogorov scale and the outer scale is the integral scale. It employs an algebraic equation for  $\Sigma$  that is similar to Eq. (7) except that fractal cutoff scales appear. Both the Zimont and Lindstedt–Vaos models are described in a review paper by Lipatnikov and Chomiak [37]. Since the first four models in Table 1 do not use differential equations to compute  $\Sigma$  they will not be discussed in this review.

Fig. 4 illustrates one of the motivations for developing a better model of premixed turbulent combustion. It shows a “lifted edge-flame” that is downstream of fuel jet that has been injected into a cross-flow of air. Initially the fuel and air streams are non-premixed. However, a stratified premixed fuel–air mixture is formed within the liftoff region between the fuel injector and the flame base. The “lifted-edge flame” in Fig. 4 is commonly found in new engines, including lean premixed prevaporized (LPP) gas turbine combustors [40], afterburners, scramjets, and direct-injection internal combustion engines. In real devices premixed combustion is important in certain regions, such as the liftoff region. Even if the fuel and air are injected in separate streams there may be significant premixing prior to combustion. To model the complex premixed and partially combustion shown in Fig. 4 a robust model is required. A promising approach is to determine the amount of surface area of the reaction layers (using the G-equation or the CFM), and then superimpose on the layers a model for fully premixed or partially premixed conditions. Such an approach allows some of the reaction surface to be fully premixed while other regions are partially premixed. It is not sufficient to assume that

simple formulas for burning velocity measured in Bunsen burners apply to complex geometries.

The purpose of this review paper is to summarize our current understanding of the structure of premixed turbulent combustion and show how this structure is related to the turbulent burning velocity. Section 2 is a review of recent images of flamelets that describe their shapes and thicknesses. Laser diagnostics provide images of the reaction layers associated with CH, CO/OH, HCO, CH<sub>2</sub>O, and heat release rate as well as the preheat zones. Section 3 reviews the current database of properties such as surface density, while Section 4 deals with the question: how well can we predict the turbulent burning velocity? Some research issues are discussed in Section 5.

Since this paper is limited to issues related to flamelet structure, the review purposely omits many measurements and modeling results that do not provide information about flame surface density or the wrinkling process. The only models considered are flamelet-structure models which can predict the flame surface density using differential equations. The reader is referred to several review papers that summarize other aspects of premixed turbulent combustion. Lipatnikov and Chomiak [37] review measured and computed turbulent burning velocities and brush thicknesses. The same authors also review molecular transport effects [41]. Bradley [42] and Abdel-Gayed et al. [43] have attempted to correlate measured values of burning velocity, while Gülder et al. [44] assess the idea of correlating burning velocities using the fractal dimension and fractal length scales. Hydrodynamic instabilities are reviewed by Kadokawa and Hasegawa [45]. A wide range of modeling approaches are reviewed by Peters [9], Veynante and Vervisch [46], Pitsch [47], Poinsot et al. [48], Poinsot and Veynante [10], Law and Sung [49] and Williams [50].

### 1.1. General concepts: flamelet wrinkling by flame–vortex interactions

Fig. 5 is a list of the important processes that occur in premixed turbulent combustion. The basic “building block” is the flame–vortex interaction. This fact was recognized by Damköhler [6] who modeled the flame surface area as a set of cones, each of which is created by the passage of an eddy, as is shown at the bottom of Fig. 5. At the bottom of the vortex the incident velocity is a minimum, so the flame propagates farther upstream. The flame–vortex interaction controls the stretch rate and the eddy residence time during which the stretch rate is applied. There are two paths in Fig. 5: the path on the right indicates that the average strength of the reaction layer is controlled by the thermodiffusive process that causes the local consumption speed to be larger or smaller than the unstretched speed  $S_{L0}$ . The theory of flame stretch helps to explain this thermodiffusive process. The path on the left side of Fig. 5 represents the wrinkling process. Each eddy stretches the surface area  $A$  at a stretch rate  $K$  that is defined to be  $(1/A)dA/dt$ . Consider the hypothetical case

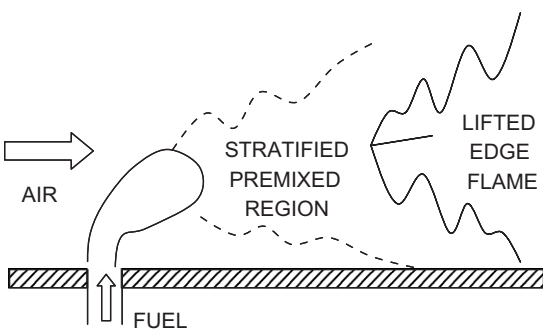


Fig. 4. Illustration of how premixed turbulent combustion plays a major role in lifted flames that have initially non-premixed fuel and air streams. Premixing in the lifted region occurs in new gas turbines, scramjets and direct-injection internal combustion engines.

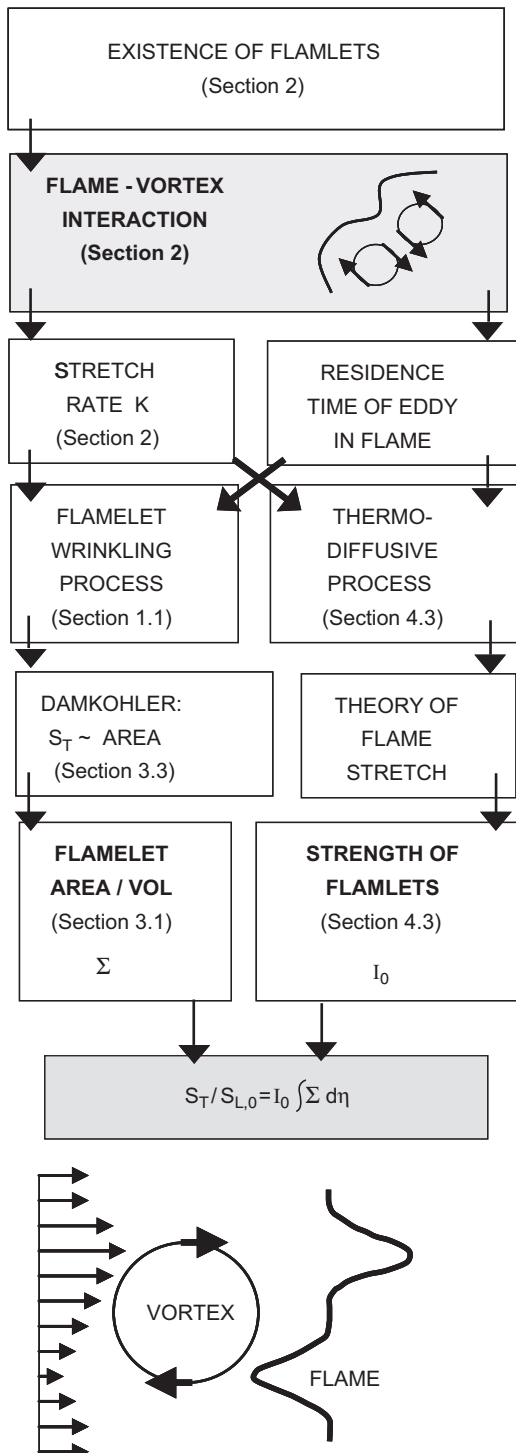


Fig. 5. Basic physics of premixed turbulent combustion. Also shown is a schematic of Damköhler's concept of a flame–vortex interaction, from Lewis and von Elbe [6], p. 415.

for which  $K$  is constant in time; integration of the definition of  $K$  yields

$$A_2/A_1 = \exp(Kt_{\text{res}}). \quad (9)$$

Thus, the area after the flame–vortex interaction  $A_2$  depends on two quantities: the stretch rate  $K$  and the

residence time  $t_{\text{res}}$  of the interaction. The residence time associated with large vortices is likely to be large, suggesting that large eddies should be more effective in increasing flame area than small eddies.

The flame surface density balance [19] represents one way to model the physical process listed in Fig. 5:

$$\frac{\partial \Sigma}{\partial t} + \tilde{U} \frac{\partial \Sigma}{\partial x} + \tilde{V} \frac{\partial \Sigma}{\partial y} = v_T \frac{\partial^2 \Sigma}{\partial y^2} + \bar{K} \Sigma - \bar{M} - \bar{Q}. \quad (10)$$

The convection terms in Eq. (10) simulate the way that a flame can be wrinkled at one location and this wrinkledness can be convected downstream. The diffusion term simulates the observed spreading of a flame brush due to turbulent diffusion. The source of flame area is the term containing the mean stretch rate  $\bar{K}$ , where  $K$  is defined by Poinsot et al. [48,51] and Law and Sung [49] to be

$$K = -\mathbf{n} \cdot (\mathbf{n} \cdot \nabla) \mathbf{V} + \nabla \cdot \mathbf{V} + S_L/R_c, \quad (11)$$

$R_c$  is the radius of curvature of the interface. The quantity  $\bar{Q}$  in Eq. (10) is the mean quenching rate and the mean merging rate  $\bar{M}$  has been modeled by Duclos et al. [24] as

$$\bar{M} = \frac{\beta_0(S_L + C\sqrt{k})}{(\bar{Y}_F/\bar{Y}_{F0})[1 - (\bar{Y}_F/\bar{Y}_{F0})]} \Sigma^2, \quad (12)$$

$\bar{Y}_F$  is the mean fuel mass fraction which has the value of  $\bar{Y}_{F0}$  upstream of the brush. Duclos set  $\beta_0$  equal to 1.0 and  $C$  equal to 0.5;  $k$  is the turbulent kinetic energy. The merging rate term was assumed to be proportional to  $\Sigma^2$  by drawing an analogy with the rate of collisions that occurs between molecules in a gas; if the number of flamelet segments is doubled, the number of collisions between them should be four times larger.

The time-averaged stretch rate  $\bar{K}$  was determined by Meneveau and Poinsot [19] to be

$$\bar{K} = (u'/\ell)\Gamma_K, \quad (13)$$

$\Gamma_K$  is the stretch efficiency function. Ref. [19] explains how this quantity was computed using DNS. Solutions first were obtained for the case of a single toroidal vortex that interacts with a laminar flat flame. A range of vortex diameters and rotational velocities were considered. It was assumed that real turbulence can be represented by an ensemble of toroidal vortices. The number of vortices in each size range was selected so that the power spectrum of the resulting vorticity field was similar to that of isotropic turbulence. The computations predicted how the stretch rate varies with time during each flame–vortex interaction. An assumption was made to relate the residence time of each flame–vortex interaction to the vortex size. The mean stretch rate exerted by the entire ensemble of vortices was determined by averaging the stretch rate for each interaction over the range of residence times and vortex sizes. Ref. [19] contains plots of the computed values of stretch efficiency  $\Gamma_K$ ; a reasonable fit to the results is Eq. (14) for a realistic range of integral scales between 10 and 100 times

the laminar flame thickness:

$$\Gamma_K = C_1 \left( \frac{\ell}{\delta_{L0}} \right). \quad (14)$$

Over the range of interest  $\Gamma_K$  is found to be nearly proportional to the integral scale and is nearly independent of the turbulent velocity fluctuation level  $u'$ . Thus larger eddies are more efficient at stretching the flame surface than smaller eddies. Some improvements were added by Charlette et al. [34] to develop an LES subgrid model based on the stretch efficiency function. Their relation for  $\Gamma_K$  does not differ significantly from Eq. (14);  $\Gamma_K$  is nearly independent of  $u'$  and is approximately proportional to the integral scale. Meneveau and Poinsot's results are a good example of how DNS can be applied to simple problems (such as a single flame–vortex interaction) in order to develop useful submodels.

One realistic aspect of the flame surface density balance (Eq. (10)) is that it provides a simulation of a geometry-dependent wrinkling process that retains a “memory” of the wrinkling that occurred at upstream locations. For example, it predicts that  $\partial\Sigma/\partial x$  will be positive or negative depending on how much new surface area is created by the stretch rate source term and how much of that new surface area diffuses away from the center of the brush as the brush becomes broader. At each location  $\Sigma$  depends on the values of  $\Sigma$  at upstream locations.

## 1.2. Turbulent burning velocities—definitions

At this point it is useful to review three common definitions of the turbulent burning velocity  $S_T$ . There is no single definition of the turbulent burning velocity that has emerged from past research. To some researchers  $S_T$  is an indicator of the mass per second of reactants consumed, so they define  $S_T$  to be a consumption speed. To others  $S_T$  indicates how rapidly the leading edge of the brush will traverse a certain distance, so they define it to be a displacement speed:

$$S_{T,GC} = \text{Global consumption speed} = \frac{\dot{m}_R}{\rho_R A_{\bar{c}=0.5}}, \quad (15)$$

$$S_{T,LC} = \text{Local consumption speed} = S_{L0} I_0 \int_{-\infty}^{\infty} \Sigma d\eta, \quad (16)$$

$$S_{T,LD} = \text{Local displacement speed} = (\mathbf{V}_{FLAME} - \mathbf{V}_{GAS})_{LE} \cdot \mathbf{n}_{LE}. \quad (17)$$

Before discussing these definitions, it is noted that there is no logical reason why there should be only one “superior” definition of the turbulent burning velocity. It can be argued that each of these three definitions is a valid way to compare an experiment to a simulation that has an identical geometry. It should be realized that for any specific flame the magnitudes of the three quantities  $S_{T,GC}$ ,  $S_{T,LC}$  and  $S_{T,LD}$  are not equal, as was demonstrated by

Shepherd and Cheng [13] and Lawn and Schefer [14]. When comparisons are made, values of consumption speeds for example, should only be compared to other values of consumption speeds and should not be compared to displacement speeds. Each of the speeds above is defined precisely and there is no ambiguity. Exactly the same algorithm can be used to determine consumption speed, for example, from experimental and from DNS results. A first requirement that should be imposed on any model is that it should predict a turbulent burning velocity that is realistic, just as it is important for any model of a non-premixed jet flame to be able to predict a jet flame length that is realistic. Problems have arisen in the past because values of these three burning velocities were measured by different researchers and it was incorrectly assumed that the three quantities should be equal, which resulted in graphs that contain a large amount of scatter.

Eq. (15) defines the global consumption speed ( $S_{T,GC}$ ) that is typically measured in Bunsen geometries. It is proportional to the total mass flow rate of reactants  $\dot{m}_R$  which is the measured total mass flow rate provided to the Bunsen burner. To use this definition it is necessary that all of the reactants pass through the flame brush. Bunsen flames meet this requirement, but reactants often flow around the edges of counterflow and V-flames, so  $\dot{m}_R$  is not known. For this reason  $S_{T,GC}$  is not usually reported for counterflow or V-flames.  $A_{\bar{c}=0.5}$  is defined as the area of the  $\bar{c} = 0.5$  contour of the Bunsen flame. To better understand Eq. (15), consider a hypothetical flat turbulent flame that has contours of  $\bar{c}$  that are flat planes. In the time  $\Delta t$  the entire brush moves forward a distance  $S_{T,GC} \Delta t$ . The volume of reactants that was traversed by the wave is  $S_{T,GC} \Delta t A_{\bar{c}=0.5}$ . The mass of reactants in this volume is  $\rho_R S_{T,GC} \Delta t A_{\bar{c}=0.5}$ . Dividing this number by  $\Delta t$  yields the mass per second of reactants traversed by the wave, which then is set equal to the mass per second of reactants exiting the burner ( $\dot{m}_R$ ), which leads to Eq. (15). Eq. (15) is not ambiguous;  $S_{T,GC}$  can be determined accurately from experimental or DNS results in exactly the same way. It can be argued that because the area  $A_{\bar{c}=0.5}$  is chosen, the choice of using the  $\bar{c} = 0.5$  contour (rather than the  $\bar{c} = 0.4$  contour) is somewhat of an arbitrary decision. This decision is similar to the decision to define the width of a jet flow to be the radius where the mean velocity, normalized by the centerline velocity, is 0.5. The definition of jet width is precise, unambiguous, but it involves the arbitrary decision to use a value of 0.5.

The local consumption speed  $S_{T,LC}$  is defined by Eq. (16). Profiles of surface density ( $\Sigma$ ) must be measured using laser-imaging diagnostics. Section 3 discusses recent measurements of surface density and the resulting local consumption speeds. The third type of turbulent burning velocity is the local displacement speed ( $S_{T,LD}$ ); it is defined by Eq. (17). It usually is measured in counterflow, low-swirl, spherical and V-flames.  $\mathbf{V}_{FLAME}$  is the velocity of the flame in the laboratory coordinate system; it normally is zero because counterflow and V-flames are stationary in

the lab coordinates.  $\mathbf{V}_{\text{GAS}}$  is the velocity in the lab frame of the gas into which the wave is propagating. The velocities and the normal  $\mathbf{n}$  are defined to be the values that occur at the leading edge of the brush. For counterflow or low-swirl burners, the reactants initially are decelerating and heat release causes the fluid elements to accelerate after they cross the leading edge of the brush. Therefore, the leading edge is defined to be the location where the profile of the mean velocity displays a minimum value. The definition of  $S_{T,\text{LD}}$  is precise, unambiguous, and is consistent with the way that the laminar burning velocity has been defined in a counterflow burner. The decision to evaluate the right side of Eq. (17) at the leading edge is an arbitrary choice but it presents no problem as long as it is realized that  $S_{T,\text{LD}}$ ,  $S_{T,\text{LC}}$  and  $S_{T,\text{GC}}$  should not have equal magnitudes. If it is desired to determine the time that it takes the leading edge of a flame brush to traverse an engine cylinder, then the displacement speed should be chosen. If it is desired to know the mass per second of reactants consumed, the consumption speed should be chosen.

Shepherd and Cheng [13] and Lawn and Schefer [14] have compared the displacement and consumption speeds of flat flames that were stabilized in a low-swirl burner and a diffuser burner, respectively. In both studies the displacement speed is consistently 2–3 times the local consumption speed. It is unfortunate that researchers have not agreed to use the same definition of the leading edge of the brush when they evaluate Eq. (17). Lawn and Schefer define the leading edge to be the  $\bar{c} = 0.02$  contour. Despite the fact that the leading edge is defined in Ref. [13] to be located at a different value of  $\bar{c}$  than in Ref. [14], the conclusion is still valid that displacement speeds are 2–3 times the consumption speeds. One reason for the difference in speeds is that flow divergence causes the areas of the leading edge and trailing edge of the flame brush to differ. Consider a flat turbulent flame that is in a flow that has diverging streamlines, such as those in a counterflow or low-swirl burner. The mean isotherms are horizontal planes. The mass per second of reactants that cross the leading edge of the brush is equal to the left side of

$$\rho_R S_{T,\text{LD}} A_{\text{LE}} = \rho_R \tilde{S}_{F,C} A_T. \quad (18)$$

The right side is derived by assuming that the region between the diverging streamlines contains wrinkled flamelets which have a total surface area of  $A_T$ . Their average consumption speed is  $\tilde{S}_{F,C}$  which was defined by Eq. (3) to be equal to  $I_0 S_{L0}$ . The gas density just ahead of each flamelet is  $\rho_R$ . Recall that Eq. (4) indicates that the wrinkled area  $A_T$  is the area of the unwrinkled flame (which would lie along the  $\bar{c} = 0.5$  contour) multiplied by the integral of  $\Sigma$  across the brush, so Eq. (18) becomes

$$\rho_R S_{T,\text{DL}} A_{\text{LE}} = \rho_R I_0 S_{L0} \int_{-\infty}^{\infty} \Sigma d\eta A_{\bar{c}=0.5}. \quad (19)$$

The ratio of the displacement speed to the consumption speed is determined from Eqs. (19) and (16) to be

$$\frac{S_{T,\text{LD}}}{S_{T,\text{LC}}} = \frac{A_{\bar{c}=0.5}}{A_{\text{LE}}}. \quad (20)$$

It can be concluded that one reason why displacement and consumption speeds differ is that the areas used in the two definitions differ. Displacement speed is based on the properties at the leading edge, while consumption speed is not. If the streamlines are diverging, as they are in Shepherd and Cheng's experiment, the displacement speed will exceed the consumption speed. The effects of streamline divergence have been analyzed by Poinsot et al. [51] for laminar flames which also display differences between consumption and displacement speeds. Lawn and Schefer [14] argue that streamline divergence is not the only cause for the differences in their speeds, since they make efforts to minimize their streamline divergence and they still see a difference. In addition to the above definitions of turbulent burning velocity, Ghenai et al. [52] suggest that the burning rate integral is important. It is proportional to the mass flux of reactants crossing a control volume that encloses a segment of the brush. They measure the flux of reactants across each surface and use diagnostics to determine the correlation term  $\overline{\rho' u'}$ . It is not yet possible to compare values of the burning rate integral to other results because of the limited amount of data.

## 2. Images of thin flamelets

In this section we address the question: what evidence do we have that flamelets exist? New laser diagnostics now make it possible to observe flamelet structure within fully turbulent premixed combustion. Therefore twenty papers [53–72] have been identified that report images of the primary reaction zones or the preheat zones. The only images that are considered are those that were obtained with an acceptable spatial resolution of less than 250  $\mu\text{m}$ , and which use reliable markers of the temperature field (such as Rayleigh scattering) or the primary reaction zone (such as CH or  $\text{CH}_2\text{O}$  PLIF). Papers that are not considered are those that image the post-flame gases (using OH PLIF, for example). In every one of the twenty papers it is found that the reaction zones and preheat zones are thin layers, having thicknesses between 0.5 and 4 times the unstretched laminar flame thickness.

Peters [8,9] defines a laminar flamelet to be a layer that contains a preheat and reaction zone, has gradients in the normal direction that are significantly larger than gradients in the tangential direction, and has a molecular diffusivity that is much larger than the turbulent diffusivity within the layer. Peters also defines another regime which occurs when the preheat zone is broadened but there is no broadening of the reaction zone. In this regime small eddies fit in the preheat zone but do not fit into the reaction zone. This regime has been called the regime of the “broadened preheat zone/thin reaction zone”, or “thick layers” [9].

Unfortunately there has been no experimental verification that eddies are the cause of any broadening of the preheat zone. To verify that turbulence is the cause of broadening, images of vortices that are smaller than the layer thickness would have to be obtained. Measurements that simply show that the layer is thicker than the unstretched thickness are not conclusive evidence that turbulence is the cause of the broadening. A laminar flamelet may be 3–4 times thicker than an unstrained laminar flame not because of turbulence but because of the strain rate that is applied. It also can appear to be thicker because of the orientation of the layer with respect to a laser light sheet, the spatial resolution of the measurement, or because several layers have merged together to give the appearance of a thick reaction zone.

Section 5 contains a review of some of the very few papers that provide experimental evidence that distributed combustion can exist. In these cases the deviations from flamelet behavior is due to the rapid heating of reactants caused by rapid-compression devices such as HCCI engines and shock tubes. In these cases it is the rapid compression (and not the large turbulence level) that raises the temperature of the reactants above the ignition temperature and thus is the cause of the distributed reactions.

Figs. 6–9 illustrate some examples of preheat layers and reaction layers that were imaged in Bunsen, counterflow and low swirl burners. In Fig. 6 the preheat layers recorded by Buschmann et al. [61] are shown, along with images obtained in the Bunsen burner of Chen and Bilger [66] and the low-swirl burner of Shepherd et al. [57]. Rayleigh

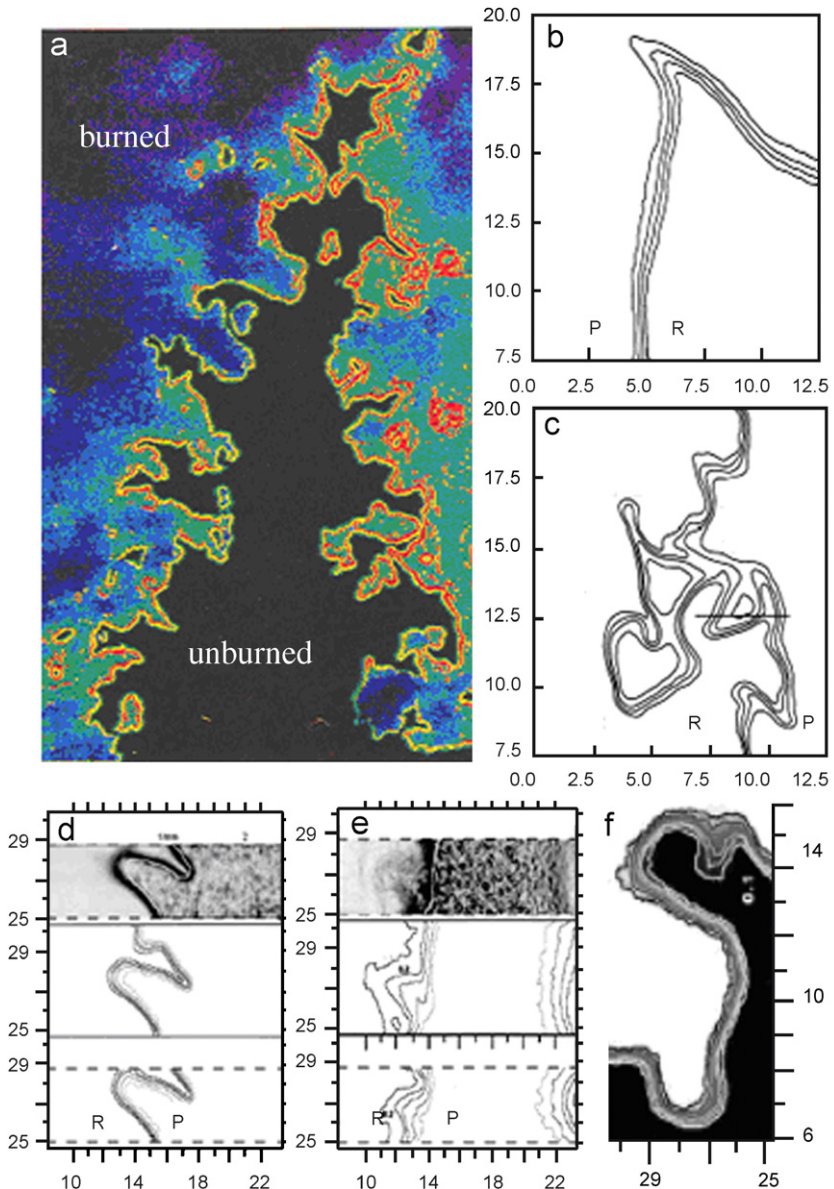


Fig. 6. Structure of preheat zones of flamelets in turbulent flames: (a) Buschmann et al. [61] Bunsen flame; (b, c) low-swirl flat flame of Shepherd et al. [57], (d) Bunsen flame of Chen and Bilger [66], propane-air, for moderate turbulence and (e) intense turbulence; (f) hydrogen-air Bunsen flame of Chen and Bilger [67]. Dimensions in mm.

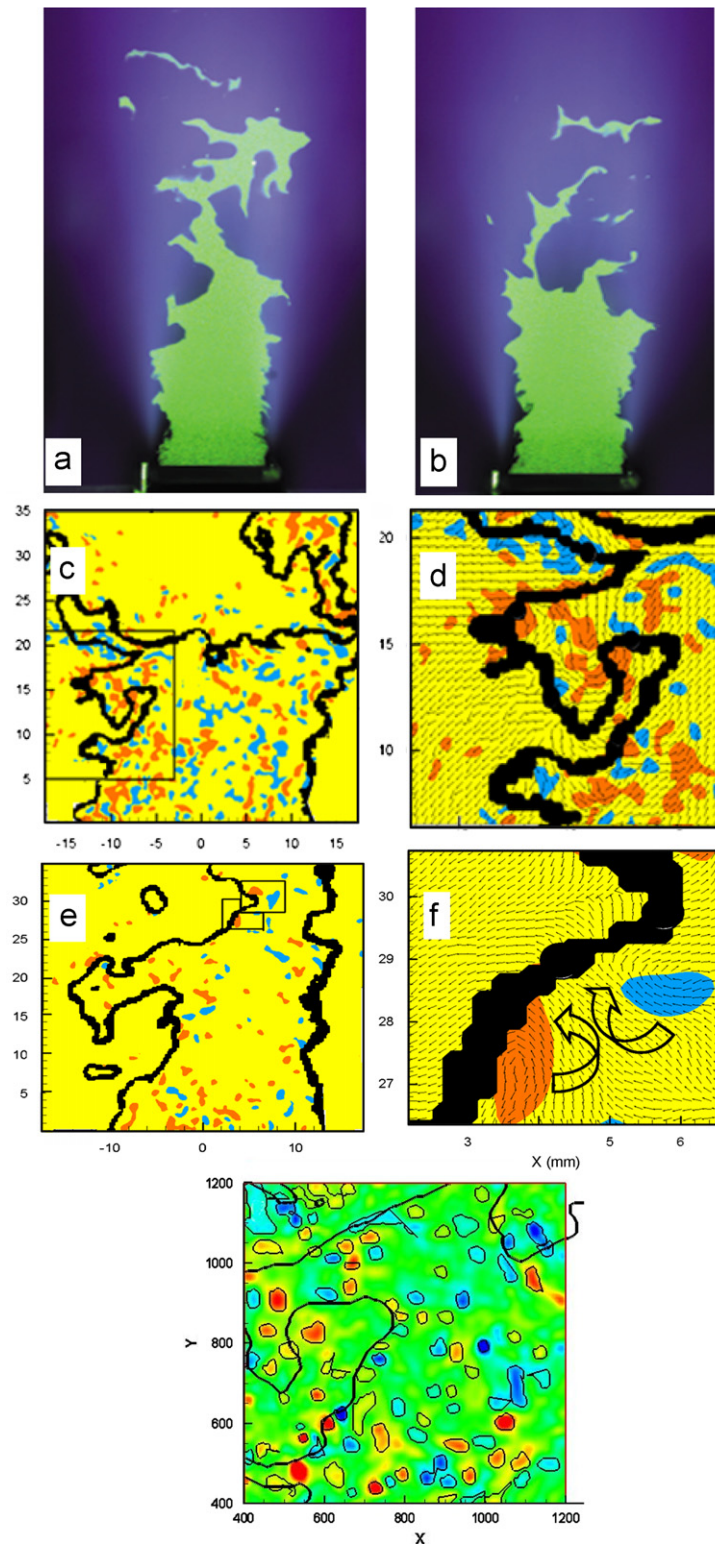


Fig. 7. (a–f) Structure of CH reaction layers (black layers) and turbulent eddies within the turbulent Bunsen flames of Filatyev et al. [53]. Stoichiometric methane-air;  $U = 8 \text{ m/s}$ ,  $u'/S_{L0} = 4.47$ ; (a, b) Mie scattering from oil drops, field of view =  $60 \text{ mm} \times 100 \text{ mm}$ , (c) simultaneous CH PLIF and PIV; red and blue regions have vorticity magnitude exceeding  $2000 \text{ s}^{-1}$ ; (d) a magnified image of the boxed region in (c); (f) magnified view of counter-rotating eddies in boxed region of (e); and (g) magnified view of turbulent eddies interacting with reaction layer (solid line) in the turbulent slot Bunsen flame of Filatyev et al. [53]. Flame shown in Fig. 8c was analyzed by Steinberg et al. [73] to achieve improved vorticity resolution. Blue regions of vorticity have clockwise rotation and red regions have counterclockwise rotation. Field of view is  $4.5 \text{ mm} \times 4.5 \text{ mm}$ .

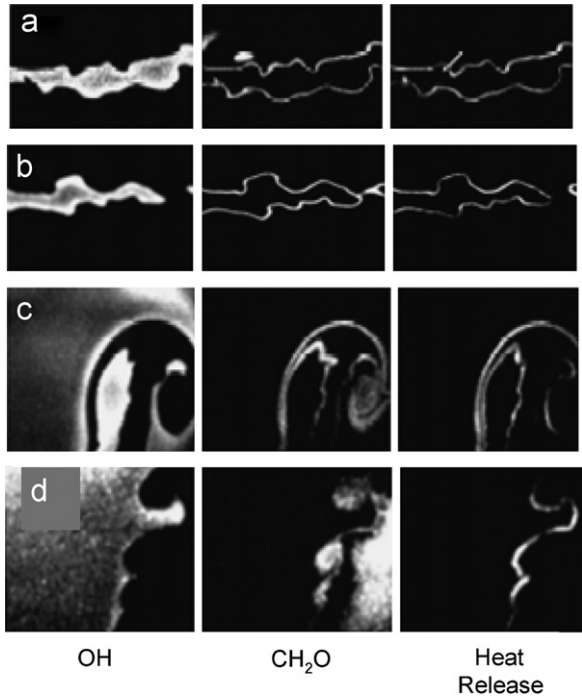


Fig. 8. Structure of the heat release layers of flamelets in the turbulent flames of Ayoola et al. [55]: (a) premixed turbulent counterflow flame, field of view = 25 mm × 16 mm; (b) premixed turbulent counterflow twin-flame; (c) premixed acoustically forced turbulent bluff-body flame; and (d) premixed turbulent bluff-body flame, unforced.

scattering was used to record the instantaneous temperature contours. The preheat zone thickness ( $\delta_{\text{PRE}}$ ) is defined as  $(T_{\text{P}} - T_{\text{R}})/(\partial T/\partial \xi)_{\text{max}}$ ;  $\xi$  is the direction normal to the layer. Fig. 7 shows the reaction layers of Filat'yev et al. [53] that were imaged in a Bunsen burner using CH planar laser induced fluorescence (PLIF) and simultaneous particle image velocimetry (PIV). The reaction zone that is identified by the thick black layer is the location where the CH signal exceeds a specified value (half of its maximum value). Fig. 7g is a magnified view of Fig. 7c; the individual eddies are observed using the improved vorticity field data analysis of Steinberg et al. [73]. Many vortices are identified which are about to cross the reaction layer. Heat release layers are seen in Fig. 8 that were imaged by Ayoola et al. [55] using  $\text{CH}_2\text{O}/\text{OH}$  PLIF methods. One of their laser sheets was tuned to provide formaldehyde ( $\text{CH}_2\text{O}$ ) fluorescence, while their other laser sheet was tuned to provide OH fluorescence. Their analysis demonstrates that the product of these two signals is proportional to the local volumetric heat release rate. For all cases in Fig. 8 the thickness of the heat release layer is less than 1 mm. Their cases correspond to turbulent counterflow twin flames and a premixed bluff body geometry.

Now that images of the reaction layers have become available, what is the structure of premixed turbulent combustion that is emerging from these observations? Fig. 9 is a schematic of the flamelets that are typically seen.

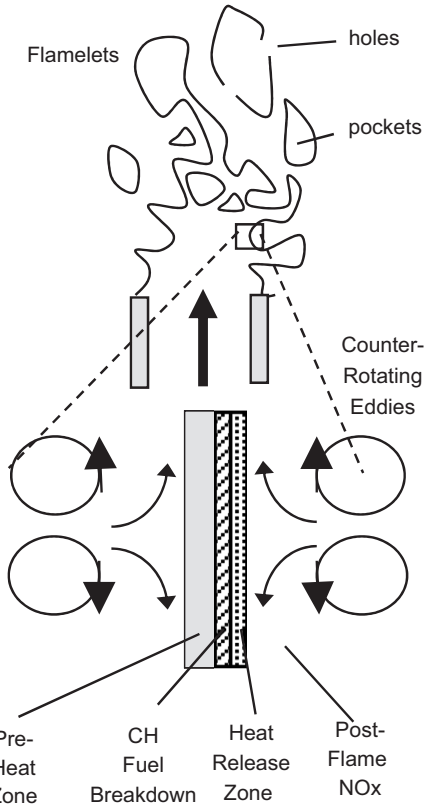


Fig. 9. Structure of turbulent premixed flames. Nearly continuous flamelets form borders around the main reactant flow, around pockets of reactants, and around pocket of products. Preheat and CH fuel breakdown reaction layer thicknesses are less than 1 mm. Post flame gases where thermal  $\text{NO}_x$  is formed are distributed  $\text{NO}_x$  reaction zones, but they are not part of the primary reaction zone.

One long and nearly continuous flamelet usually surrounds the main region of reactants. Others often surround pockets that are filled with reactants or products. If the pocket contains reactants the surrounding flamelet burns in an inward direction; if the pocket contains products the flamelet burns outward. At some locations it is possible for a hole in the reaction layer to occur due to local extinction, but there are no holes seen in any of the images in Refs. [53–72]. Unlike non-premixed flames, premixed flames have hot product gases that remain close to the reactants and quickly reignite any quenched regions. It has been speculated that flamelets are short, disconnected and shredded layers, but shredded layers have never been observed for fully premixed conditions. In contrast, non-premixed and partially premixed flames can become shredded and contain many quenched regions in the reaction surface [74].

In any discussion of the structure of premixed turbulent combustion it is important to differentiate between the primary reaction zone and the post-flame gases. In the post-flame gases, two types of reactions often occur: those associated with OH recombination and with NO formation. These post-flame reactions always will be distributed in space, even if the flame is laminar. Some previous studies

have erroneously reported that the presence of broad OH concentrations within the post-flame gas is an indicator that the primary reactions are in the distributed combustion regime. The post-flame reactions involving water vapor and OH will continue to occur far downstream of the primary heat release reactions. In addition, large concentrations of OH do not necessarily indicate that the overall OH reaction rate is large. The overall OH reaction rate often is zero in the post-flame gases where the OH and water vapor are in equilibrium, yet the OH concentrations may be large. The reactions that create NO also can be distributed in space in the post-flame gases, whether the flame is laminar or turbulent. The diagnostics that have proven to be useful in determining whether layers are thin are those that quantify the temperature contours and the CH contours. It has been shown that the CH contours do indicate the boundaries of the primary heat release region, based on numerical simulations of laminar flames.

For comparison purposes, Figs. 10 and 11 are included to show that non-premixed flamelets can be shredded to form regions of partially premixed combustion. These are images of the thin CH layers within non-premixed flames that are subjected to very strong recirculation zones of Ratner et al. [74] and Rasmussen et al. [76]. The shredded flame seen in Fig. 10 has many segments; the end of each

segment is believed to be an edge-flame that consists of both premixed and non-premixed reaction layers. The shredding is due to the very large velocity fluctuations of 6 m/s and the long residence times associated with the low velocities in the recirculation zone. In Fig. 11 the CH layers in are shredded by a strong recirculation zone in a wall cavity that was driven by a supersonic air stream having a velocity of 590 m/s. It is noted that when strain rates are applied that cause the flamelets to extinguish, the CH layers are observed to remain thin; there is no evidence that the flamelets are broadened. Similar images of premixed flamelets subjected to large strain rates have not yet been reported.

## 2.1. Flamelets exist for Karlovitz numbers exceeding ten

A long-standing question has been—what is the boundary of the laminar flamelet regime? Some researchers have assumed that laminar flamelets no longer exist when the Karlovitz number (defined below) exceeds unity because the small eddies can fit inside the flamelet, increase the diffusivity, and form thick flames. However, this assumption is based on theoretical speculation alone. There is no experimental verification that eddies actually enter the flamelet and increase the diffusivity. In contrast, a different idea is that increasing the turbulence level favors the formation of even thinner highly strained reaction layers; thus the flamelets may “extinguish before they broaden”. To date there is no experimental evidence that premixed flames can be shredded into thin disconnected flamelets.

To better define the conditions of any experiment, it is suggested that the definition of Karlovitz number that was proposed by Peters [9] be adopted for consistency. This would avoid the ambiguities that now exist because different definitions of  $Ka$  are used. Peters defines  $Ka$  to be the ratio of the ratio of the flame time ( $\alpha/S_{L0}^2$ ) to the time associated with flame stretch rate. This latter time is the inverse of  $(1/A)(dA/dt)$ , which he argues is the ratio of  $u'$  and the Taylor scale. He shows that this time scale equals the Kolmogorov time ( $\eta_K/u_K$ ). The Kolmogorov length scale  $\eta_K$  equals  $\ell(u'\ell/\alpha)^{-3/4}$  and  $u_K$  is  $v/\eta_K$ . The thermal diffusivity  $\alpha$  is  $\alpha_0 [(T_P + T_R)/2]/300 \text{ K}]^{1.5}$ , where  $\alpha_0$  is the diffusivity of nitrogen at 300 K, which is  $0.15 \text{ cm}^2/\text{s}$ . It is suggested that the temperature used to compute the thermal diffusivity be the average temperature (i.e., the mean of  $T_R$  and  $T_P$ ). With these definitions the Karlovitz number is:

$$Ka = \left( \frac{u'}{S_{L0}} \right)^{3/2} \left( \frac{S_{L0}\ell}{\alpha_0} \right)^{-1/2} \left( \frac{(T_P + T_R)/2}{300K} \right)^{1/2}. \quad (21)$$

It can be shown that if  $Ka$  equals unity, the Kolmogorov scale ( $\eta_K$ ) equals the characteristic flame thickness ( $\alpha/S_{L0}$ ).

**Table 2** lists some measured values of the average preheat zone thicknesses ( $\delta_{\text{PRE}}$ ). The last two columns in **Table 2** indicate that the Karlovitz number can be large (10.9, 25.2, 43.5) yet the average preheat zone thickness is

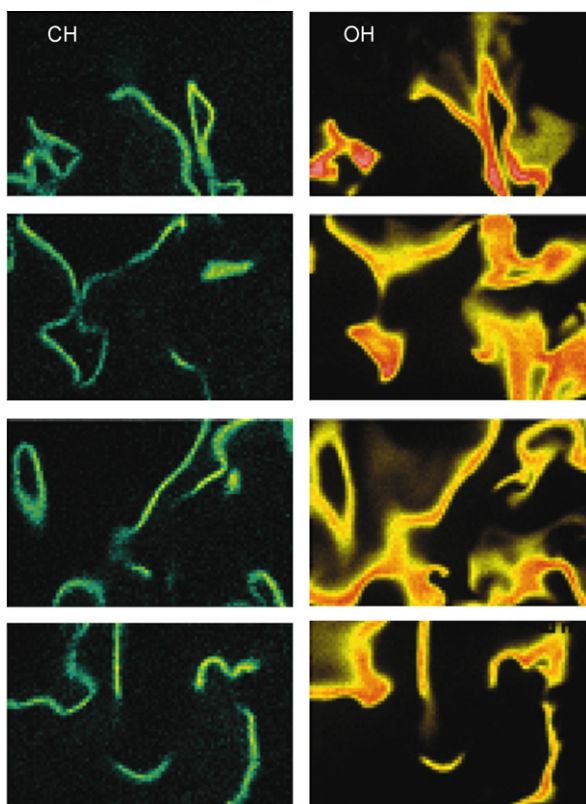


Fig. 10. Shredded flamelets observed in non-premixed combustion; partially premixed conditions occur in the regions where there is local extinction Ratner et al. [74]. CH layers appear on left, simultaneous OH PLIF signal is on right. Flamelets are seen to “extinguish before they broaden”.

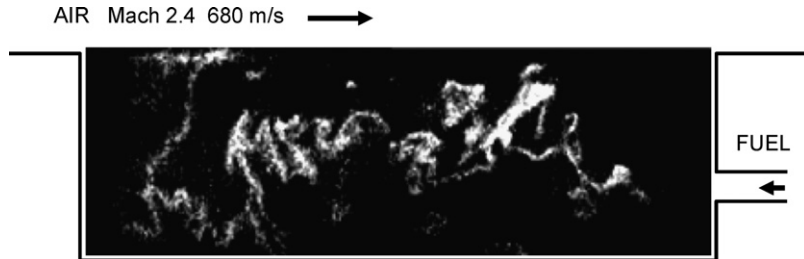


Fig. 11. Thin flamelets observed in non-premixed combustion even for highly turbulent conditions of Rasmussen et al. [76]. Supersonic velocity on top of cavity is at 590 m/s. CH PLIF images are shown.

Table 2

Thicknesses of preheat zones measured using Rayleigh scattering for various Karlovitz numbers defined by Eq. (21)

Authors reporting measured preheat zone thickness	Fuel	$\phi$	$u'$ (cm/s)	$S_{L0}$ (cm/s)	Integral scale (cm)	Karlovitz number (Eq. (21))	$\delta_{PRE}/\delta_{L0}$
Shepherd et al. [57]	Lean methane	0.7	374	20	1.50	10.9	0.9
Buschmann et al. [61]	Lean methane	0.6–0.8	220	8.5	1.76	25.2	1.0
Buschmann et al. [61]	Lean methane	0.6–0.8	13	27	0.73	0.1	0.4
Dinkelacker et al. [62]	Lean methane	0.5	900	39	1.00	13.1	0.5
Dinkelacker et al. [62]	Lean methane	0.5	370	11	1.00	43.5	0.8
Soika et al. [63]	Lean methane	0.50–0.8	36	18	0.60	0.6	0.9
Soika et al. [63]	Lean methane	0.5–0.8	26	26	0.60	0.2	0.7
Chen and Bilger [67]	Lean hydrogen	0.3–25	109	806	0.80	12.7	1.0
Chen and Bilger [66]	Lean methane	0.65–0.9	65	24	0.83	0.7	1.5
Mansour et al. [54]	Lean methane	1.0	845	40	0.48	16.4	2.5
Chen and Bilger [66]	Lean propane	0.7	110	20	0.90	2.2	3.0
O'Young, Bilger [70]	Lean propane	0.7	70	29	1.00	0.5	3.0

Note that thin flamelets can exist even for  $Ka > 10$ .

measured to be no larger than the laminar value. In some of these cases ( $u'/S_{L0}$ ) is 18.7, which is considered to be a very intense turbulence level, yet there is no broadening measured. Based on Table 2 the criterion that flamelets become thick when Karlovitz number exceeds unity does not appear to be realistic. The data suggest that it is necessary to have eddies that are much larger and stronger than those at the Kolmogorov scale to cause deviations from flamelet structure. Recall that eddies at the Kolmogorov scale are so weak that they typically are destroyed by weak viscous forces during one eddy turnover time. In contrast, heat release imposes a strong disturbance—the gas expansion superimposes an additional velocity of typically 200 cm/s to the product gases, which is much larger than the Komogorov eddy rotational velocity. The data in Table 2 indicate that new criteria are needed to identify deviations from flamelet behavior.

Rayleigh scattering diagnostics were used to measure the temperature contours in the studies listed in Table 2. The researchers who report no broadening of preheat zones due to turbulence include Buschmann et al. [61], Dinkelacker et al. [62], Soika et al. [63,64] Shepherd et al. [57] and Chen and Bilger for their hydrogen cases [67]. Chen and Bilger [66] and Mansour et al. [54] state that their preheat zones were “lamella-like” at low turbulence levels and no thicker

than the unstretched laminar flame thickness  $\delta_{L0}$ . Dinkelacker et al. [62] measured preheat zone thicknesses that were between 0.5 and 1.0 times  $\delta_{L0}$  for all six cases that they considered.

In contrast to these findings, Mansour et al. [54], Chen et al. [71], O'Young and Bilger [70] and Chen and Bilger [66] reported that for several of their cases their time-averaged preheat zone thicknesses were two to four times larger than the unstretched laminar value. If the theoretical speculations are correct, then the thickened layers of Refs. [54,66] should correspond to large values of Karlovitz number while the thin flamelets should correspond to smaller values of  $Ka$ ; unfortunately this is not the case. Table 2 shows that for a large value of  $Ka$  of 43.5 there is no thickening seen by Dinkelacker et al. [62] yet for a smaller value of  $Ka$  equal to 2.2 there is substantial thickening measured by Chen and Bilger [66].

There are several possible explanations for the fact that the normalized preheat zone thickness ( $\delta_{PRE}/\delta_{L0}$  in Table 2) is less than one in many studies, yet it exceeds one in a few other studies. Dinkelacker [65] concludes that variations in  $(\delta_{PRE}/\delta_{L0})$  are consistent with a strain rate argument. He notes that the thickest preheat zones were recorded when lean propane was used [66,70] while no thickening occurred for the lean methane cases in Refs.

[57,61–63]. It can be assumed that the net strain rate is positive because the total area of the layers is increased by the turbulence. It is known that if a positive strain rate is imposed on a lean propane–air laminar flame the strain will make the flamelet thicker, whereas a positively strained lean methane–air laminar flame becomes thinner. This strain rate explanation may explain why thickening occurs in Refs. [66,70] but does not occur in the other studies. Another possible explanation is associated with layer merging. When many cusps appear there will be layers that merge together within the cusps. The layer thickness in this merged region will be measured to be larger than its real value, and this causes the mean thickness to be erroneously large. Measured values of layer thickness always will be somewhat larger than the real thickness due to the orientation angle between the flamelet and the laser sheet. In addition, measured values can be erroneously large due to the limited spatial resolution associated with the laser sheet thickness.

Another argument that has been offered is that it appears that eddies do not enter the preheat zone because the turbulence intensity ( $u'/S_{L0}$ ) was systematically increased by a factor of five in the studies of Shepherd and Cheng [13] and Filatyev et al. [53], but there was no measurable increase in the thickness of the preheat layers or the CH layers, respectively. If eddies enter the preheat zones and cause the turbulent diffusion to dominate over molecular diffusion it would be expected that increasing the turbulence intensity would increase both the turbulent diffusivity and the layer thickness. Based on this argument, the authors of Refs. [13,53] believe that the layers they observed are laminar flamelets. However, such arguments are not conclusive since no images were presented which identified small scale eddies. What can be concluded is that the studies to date have demonstrated that flamelets are typically no thicker than laminar unstretched flames in most cases, but in some experiments the preheat zone is 2–4 times that of an unstretched flame. The reasons for the broadening observed in some cases is still not clear. Possible broadening by turbulent eddies cannot be ruled out, but the broadening instead could be due to the effects of strain rate or due to laser sheet-layer misalignment. To understand the role of small eddies, images with improved spatial resolution are needed.

In two DNS studies the flamelet thickness has been computed for relatively large Karlovitz numbers and only a small amount of broadening occurs. Sankaran et al. [3] simulated a Bunsen burner for a very high intensity ( $u'/S_{L0}$ ) of 10, a Karlovitz number based on Eq. (21) of 5.2, and a 3-D grid resolution of 20 μm. The mean thickness of their reaction layer was not increased by the turbulence but the mean thickness of the preheat zone was about 20% larger than the laminar unstretched value. They do not state if this 20% thickening is due to eddies that may enter the preheat zone or is due to stretch effects. It also may be due to distortions of the flame shape when cusps and pockets are created. The fact that they found their preheat zone to

increase by only 20% indicates that their flame is still in the flamelet regime even though their Karlovitz number is large (5.2). Sankaran et al. also demonstrated that the profiles of reactedness across each layer are remarkably similar to that of a laminar counterflow flame. This work supports Damkohler's hypothesis; even for very large turbulence intensities ( $u'/S_L = 10$ ) Sankaran et al. find that the turbulence increases the layer surface area but does not significantly alter the internal structure of the layers by more than 20%. Tanahashi et al. [75] used DNS to simulate a flame wrinkled by decaying isotropic turbulence in a box. Their 3-D code had a 20 μm grid resolution and included complex chemistry. They concluded that their computed reaction layers remain thin and sheet-like, even when the turbulence intensity is large ( $u'/S_L = 3.4$ ) and the integral scale was less than the laminar flame thickness. Their maximum heat release rate was much as 30% larger than the laminar case, but they do not find that this is due to eddies inside the flame; instead they find that it is associated with thermodiffusive effects in the regions of negative curvature.

## 2.2. Images of flame–eddy interactions in turbulent flames

Some recent work has demonstrated that it is possible to use laser diagnostics to image the flame–eddy interactions that occur within fully turbulent premixed flames. Fig. 7 shows some of the images of vortices obtained by Filatyev et al. [53] in a turbulent Bunsen flame for relatively large turbulence intensity ( $u'/S_{L0}$ ) of 4.47. The wrinkled reaction layer (black) is identified with CH PLIF diagnostics while the eddies are regions where the magnitude of the vorticity was measured with PIV to exceed 2000 s<sup>-1</sup>. Fig. 7f is a magnified view of two counter-rotating eddies that are near the CH layer. Note that these velocity vectors are similar to those in a counterflow burner, and the vectors also are similar to those measured in the flame–vortex experiment of Mueller et al. [77]. Fig. 7g is a magnified view of Fig. 7c; additional eddies are identified by the improved vorticity resolution algorithm of Ref. [73].

Fig. 12 is a set of frames from a high-speed cinema-PIV movie of flame–eddy interactions that were obtained by Steinberg et al. [73] in a fully turbulent Bunsen flame. The time-history information is important because single images (such as Fig. 7) only show that an eddy might be near a wrinkle in a flamelet but it does not indicate if the eddy actually created the wrinkle or if the wrinkle was created at an earlier time. In Fig. 12 the vorticity field contours are plotted at time intervals of 1.5 ms. The premixed slot Bunsen burner of Ref. [53] was used and fully turbulent conditions were selected so that  $u'/S_{L0} = 2.9$  and the reactants were methane and air. Two high-repetition rate Nd:YAG lasers were pulsed at 1.3 kHz and images were recorded every 0.75 ms with two high-speed, high-resolution Phantom V9.0 digital cameras. The flame boundary, which is the solid black line in Fig. 12, is the

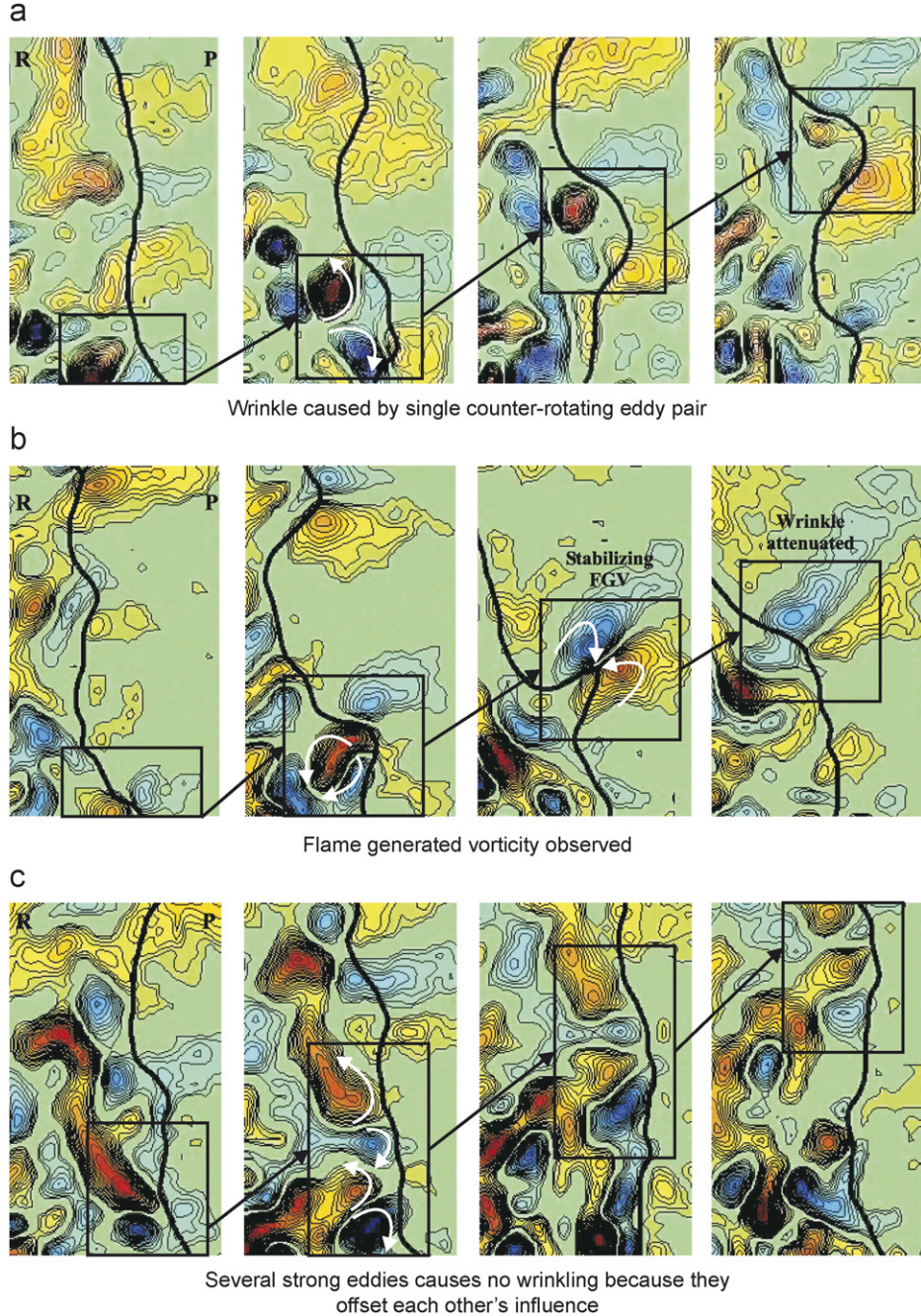


Fig. 12. Time-history of eddy–flame interactions measured by Steinberg et al. [73] using cinema–stereo PIV in a fully turbulent slot Bunsen flame. Time between images = 1.5 m. Flow is upward; reactants are on the left. Flame is the solid line.  $u'/S_{L0} = 2.9$ , methane–air. Red is positive (counter clockwise) vorticity ( $1600 \text{ s}^{-1}$ ); blue is negative vorticity ( $-1600 \text{ s}^{-1}$ ).

contour of the maximum gradient in the PIV particle density.

The top sequence of four images in Fig. 12(a) illustrate the classical wrinkling process that was predicted by Shchelkin and Damköhler [6]. A single eddy passes over the interface and the resulting wrinkle is approximately the same size as the eddy. In the middle images, a wrinkle is formed but strong flame-generated vorticity (FGV) in the products gases is observed. The blue and red vortex pair to

the right of the wrinkle is the FGV that is generated as the gas expands and accelerates across the curved interface. This FGV vortex pair in the products superimposes velocity vectors that are directed toward the top of the wrinkle and this velocity is observed to cause a rapid attenuation of the wrinkle. Thus, FGV is a stabilizing factor that tends to decrease the amplitude of the wrinkles in this case. In the bottom sequence (Fig. 12c) several strong eddies exists but they do not wrinkle the interface.

Table 3

Mean stretch rate ( $\bar{K}$ ) and the stretch efficiency function  $\Gamma_K$  measured in the turbulent Bunsen flame of Filatyev et al. [53]

Case	Height $x$ (mm)	$u'/S_{L0}$	Integral scale $\ell$ (mm)	Mean stretch rate ( $s^{-1}$ )	Stretch efficiency function $\Gamma_K$
3b	21	0.69	5.2	79	1.57
3b	56	0.69	5.2	86	1.71
3c	13	2.14	3.1	184	0.70
3c	31	2.14	3.1	174	0.66
8b	26	1.88	12.8	223	4.00
8b	61	1.88	12.8	248	4.44
8b	96	1.88	12.8	229	4.10
8c	26	4.47	8.7	389	1.99
8c	61	4.47	8.7	232	1.19

This is because the eddies are so close to each other that they counteract each other. This indicates that small eddies having large magnitudes of vorticity may be less effective than a single large eddy that has small peak vorticity but has a large circulation. Circulation is defined to be the product of the average vorticity and the area of the eddy. Large eddies can play an important role because of their large circulation and their large residence time, even though the magnitude of their peak vorticity may not be as large as that of a small eddy.

The local stretch rate is another important quantity to measure because it is a source term in the flame surface density balance (Eq. (10)) that is employed by a number of models. Filatyev et al. [53] reported measurements of mean stretch rates obtained in a Bunsen slot burner. The various terms in the definition of stretch rate (Eq. (11)) were evaluated using simultaneous CH PLIF/PIV diagnostics. The normal to each CH reaction layer was identified and PIV recorded the velocity vectors in the normal and tangential directions. All measurements were made in one plane—the plane of the laser sheet. There are three components to the stretch rate; only the two in-plane components were determined. Nearly diffusional neutral reactants were selected so that  $S_L$  was nearly equal to  $S_{L0}$ . Table 3 lists the measured mean stretch rates which varied from 79 to 389  $s^{-1}$ . For all cases the mean stretch rate was positive, as expected. The instantaneous stretch rates oscillated between +2500 and  $-1000 s^{-1}$ . Law and Sung [49] have shown that a stretch rate of 1800  $s^{-1}$  is required to extinguish a corresponding steady counterflow flame, but no local extinction occurred in the turbulent flames of Ref. [53]. Extinction requires that a sufficiently large stretch rate be imposed for a sufficiently long residence time. The eddies passed through the turbulent Bunsen flame with large convection velocities of 3–12 m/s, so the residence time is believed to have been insufficient to cause extinction. Previously Donbar et al. [79] imaged a non-premixed flame and also reported no extinction, even where the strain rates were measured to be very large. They concluded that eddies did not have sufficient residence time to complete the local extinction process.

### 3. Flamelet structure ( $\Sigma, \delta_T$ )

#### 3.1. Surface density ( $\Sigma$ )—measurements and DNS computations

In this section we compare the structure of flames that have different geometries. There have been a number of studies that provide direct measurements of the flame surface density  $\Sigma$ . For the case of Bunsen flames, surface density was reported by Deschamps et al. [80], Lee et al. [81] and Chen and Bilger [66–68]. In addition, measurements of  $\Sigma$  appearing in Bell et al. [1] were performed by Filatyev et al. [53]. For V-flames  $\Sigma$  was measured by Shepherd [82] and by Veynante et al. [25,83]. Flat flames were considered by Shepherd and Cheng [13], Shepherd et al. [57] and Lawn and Schefer [14] who used low-swirl and diffuser type burners, respectively. Renou et al. [84] studied a freely propagating flame, while a cruciform burner was employed by Shy et al. [85]. For partially premixed conditions the surface density was determined in Refs. [74] and [86]. Computations of  $\Sigma$  using DNS were performed by Bell et al. [1] for a Bunsen geometry, by Domingo et al. [87] for a V-flame, and by Boger et al. [88] and Chakraborty and Cant [89] for decaying turbulence within a box. RANS and other models also have provided predictions of  $\Sigma$  [18,23,26,28,32,90–92]; for these cases several modeling constants were required.

In order to make meaningful comparisons it is useful to define the quantity  $\Sigma_{\max}$ , which is the surface density at the center of the brush where  $\bar{c}$  is 0.5. Lawn and Schefer [14] point out that nearly all studies have found that  $\Sigma$  varies across the flame brush in approximately the following manner:

$$\Sigma = 4\Sigma_{\max}\bar{c}(1 - \bar{c}). \quad (22)$$

Fig. 13 shows that Eq. (22) provides a reasonable fit to the data of Refs. [66] and [81]. It is useful to define the flame brush thickness  $\delta_T$  using the following relation [13]:

$$\bar{c} = \left[ 1 + \exp\left( \frac{-4(\eta - \eta_m)}{\delta_T} \right) \right]^{-1}. \quad (23)$$

The coordinate  $\eta$  is normal to the brush and  $\eta_m$  is the value of  $\eta$  where  $\bar{c}$  equals 0.5. The mean reactedness  $\bar{c}$  is measured using Rayleigh scattering or oil drop imaging methods. If Eqs. (22) and (23) are inserted into Eq. (1), it follows that

$$\frac{S_{T,LC}}{S_{L0}} = I_0 \int_{-\infty}^{\infty} \Sigma d\eta = I_0 \Sigma_{max} \delta_T. \quad (24)$$

It is noted that one can better understand the physical significance of  $\Sigma_{max}$  by combining Eqs. (2) and (24) to yield

$$\Sigma_{max} = \frac{1}{\delta_T} \frac{A_T}{A_L}. \quad (25)$$

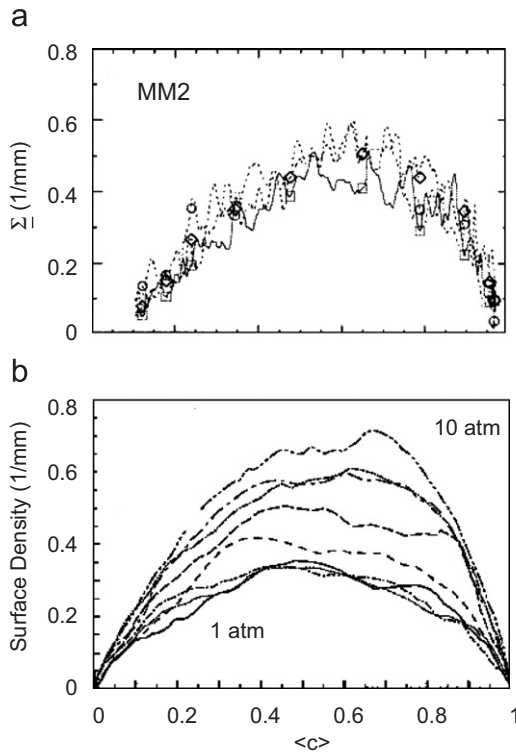


Fig. 13. Flame surface density measured in Bunsen flames of (a) Chen and Bilger [66] and (b) Lee et al. [81] plotted against mean reactedness.

For example, if the brush thickness is 6.0 mm and the ratio  $A_T/A_L$  is 2.4, then Eq. (25) indicates that  $\Sigma_{max}$  is  $0.40 \text{ mm}^{-1}$ , which is in the range of values displayed in Fig. 13. Surface density is defined to be

$$\Sigma = \lim_{\Delta x \rightarrow 0} \frac{\bar{A}_f}{\Delta x^3}, \quad (26)$$

$\bar{A}_f$  is the time-averaged surface area of flamelets within an cubic interrogation box of size  $\Delta x$ . In experimental studies, information is available only in the plane of a laser sheet so the following 2-D approximation usually is made. The right side of Eq. (26) is approximated to be the average perimeter within an interrogation box of area  $\Delta x^2$  divided by the area  $\Delta x^2$ . The accuracy of this 2-D approximation was evaluated by Bell et al. [1]. Using their 3-D DNS results for a Bunsen flame, they first computed  $\Sigma$  using Eq. (26) and defined this value to be their 3-D result. Then they identified one plane and computed  $\Sigma$  again after making the 2-D approximation. Their conclusion is that the value of  $\Sigma$  determined with the 2-D approximation should be multiplied by 1.35 to yield the correct 3-D value.

It is now possible to compare some profiles of  $\Sigma$  that have been measured for different geometries. Table 4 lists typical values that were measured in Bunsen, V-flame and flat flame burners. It is seen that  $\Sigma_{max}$  varies from 0.12 to  $0.60 \text{ mm}^{-1}$  and brush thickness is in the range from 6 to 35 mm. The last column in Table 4 is the estimated normalized value of the local consumption speed ( $S_{T,LC}$ ) that was obtained from Eq. (24); it varies from 1.3 to 7.8. It is noted that the largest normalized consumption speeds are in the range of 5.0–6.0 for atmospheric pressures; an even larger value of 7.8 was achieved at 10 atm.

Fig. 14 indicates that the profiles of  $\Sigma$  are tall and narrow at upstream locations in the V-flame of Veynante et al. [25]. The profiles become shorter and wider at downstream locations because the brush thickness increases due to turbulent diffusion. A similar trend is observed in Fig. 15d–f, which shows measured profiles of  $\Sigma$  that were reported in Ref. [1]. The curves display two sharp peaks at the upstream locations (the thin solid line) which corre-

Table 4

Flame surface density at the center of the brush ( $\Sigma_{max}$ ), brush thickness, and local consumption speeds for several experiments

Ref.	Geometry	$\Sigma_{max}$ ( $\text{mm}^{-1}$ )	Brush thickness $\delta_T$ (mm)	$S_{T,LC}/S_{L0}^*$
Deschamps et al. [80]	Bunsen	0.30	20.0	6.0
Lee et al. [81]	Bunsen	0.60	13.0	7.8
Chen and Bilger [66]	Bunsen	0.50	6.0	3.0
Bell et al. [1]	Bunsen	0.18	14.0	2.5
Shepherd [82]	V-flame	0.17	10.3	1.8
Veynante et al. [25]	V-flame	0.40	5.0	2.0
Shepherd and Cheng [13]	Low-swirl	0.20	30.0	6.0
Shepherd et al. [57]	Low-swirl	0.20	24.0	4.8
Lawn and Schefer [14]	Diffuser	0.12	35.0	4.2
Renou et al. [84]	Unconfined	0.45	6.0	2.7
Shy et al. [85]	Cruciform	0.14	9.0	1.3

\*Estimated to be the product  $(\Sigma_{max})(\delta_T)(I_0)$ .

spond to the two flame brushes that are stabilized on the right and left sides of the 2-D slot Bunsen burner. Farther downstream the two peaks merge into one thick profile (the thick solid line). As the turbulence intensity  $u'/S_{L0}$  is increased, Figs. 16 and 17 indicate that both  $\Sigma_{\max}$  and  $\delta_T$  increase and this causes their product to increase as well. Increasing the gas pressure was found to cause an increase in the values of  $\Sigma_{\max}$  that were measured in the Bunsen burner of Lee et al. [80]. This finding is explained by their

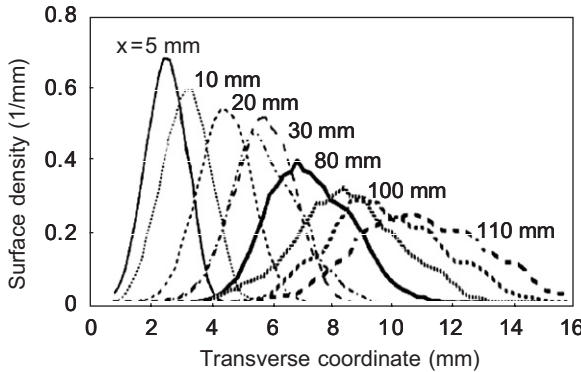


Fig. 14. Surface density measured in the V-flame of Veynante et al. [25] at different downstream locations ( $x$ ).

images which show that the flame surface has many more fine-grained wrinkles at 10 atm than at 1 atm. Elevated pressure reduces the laminar flame thickness and the theory of hydrodynamic instability [45] predicts that the cell sizes of wrinkles should decrease as the laminar flame thickness decreases.

For the case of flat flames, Figs. 18 and 19 show the results of Shepherd and Cheng [13] and Lawn and Schefer

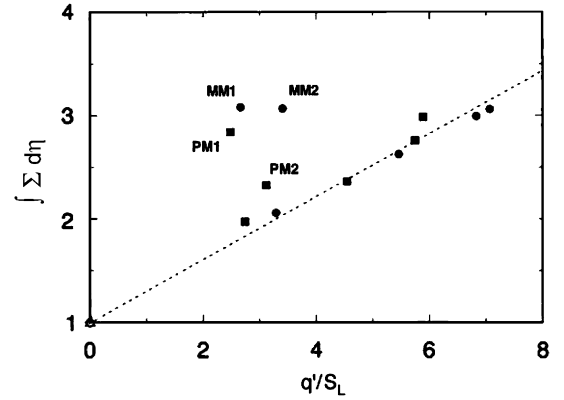


Fig. 16. Values of the measured surface density that was integrated across the brush of the Bunsen flame of Chen and Bilger [66].

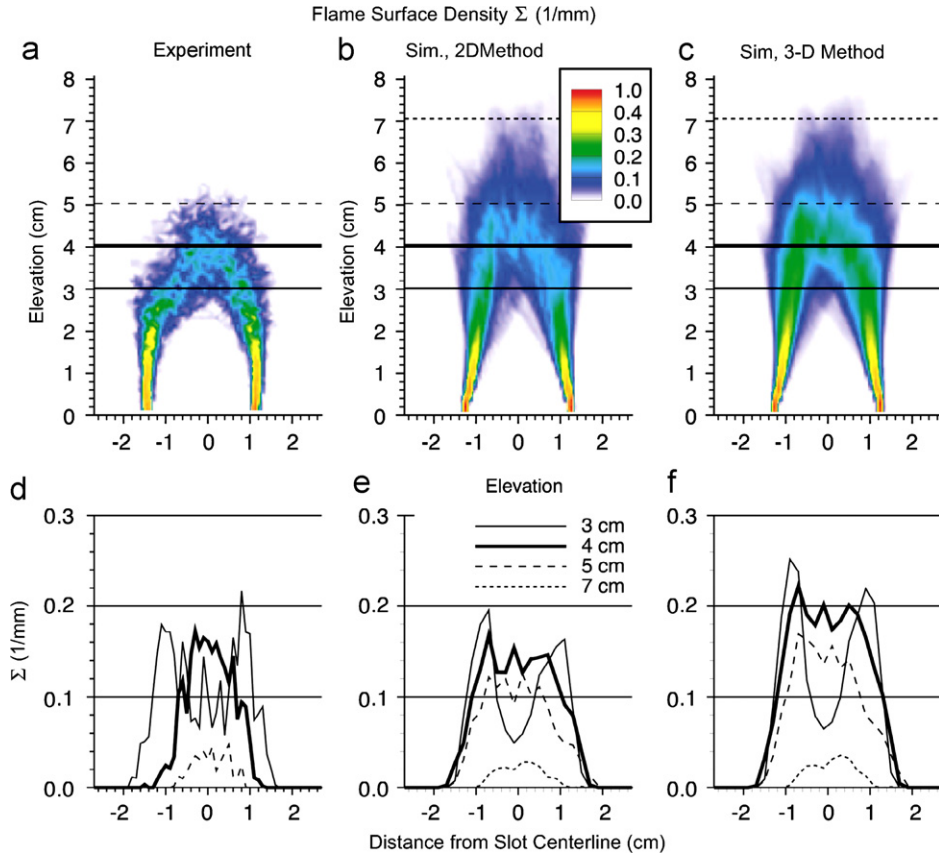


Fig. 15. Flame surface density  $\Sigma$  reported in Bell et al. [1] for the Bunsen slot burner geometry of Filatyev et al. [53]: (a, d) measured values of  $\Sigma$  based on values recorded in one plane; (b, e) DNS computations of  $\Sigma$  using only results tabulated for one plane of the 3-D data; and (c, f) DNS computations of  $\Sigma$  using the full 3-D results.

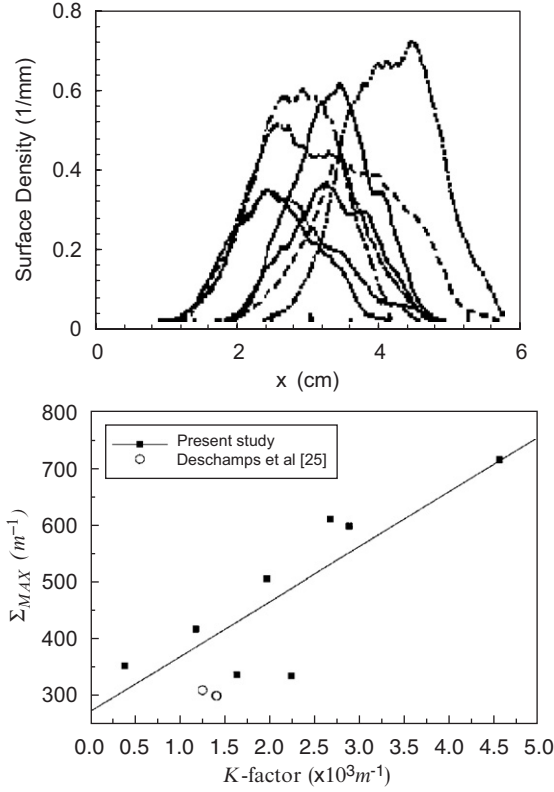


Fig. 17. Flame surface density measured in Bunsen flame of Lee et al. [81]. The  $K$ -factor is defined to be  $(u'/S_{L0})\ell^{-1}$   $[5.4 + 2.3(u'/S_{L0})]/[1 + 2.3(u'/S_{L0})]$ .

[14]. Since their brushes are relatively flat, the profiles of  $\Sigma$  remain nearly constant along the brush, unlike Bunsen or V-flames. As the turbulence level is increased, Fig. 18 indicates that the consumption speed measured by Cheng and Shepherd increases linearly even for large values of  $u'/S_{L0}$  up to 11. However, Lawn and Schefer's data in Fig. 19b displays a different trend. Their consumption speed increases with increasing turbulence level for  $u'/S_{L0}$  up to 3 and then it sharply decreases as the turbulence level is increased. Their values of  $\Sigma_{\max}$  display the same trend and their brush thickness remains nearly constant. This trend suggests that the degree of wrinkling of their flamelets eventually is limited by some mechanism, which could be the merging or extinction process, or it could be some geometric limitation. One question is whether or not the flat turbulent flames on low-swirl and diffusion burners have geometry-independent properties and their consumption speeds depend only on  $(u'/S_{L0})$  and  $(\ell/\delta_{L0})$ . If flat flames are geometry-independent, the slopes of the two curves shown in Figs. 18b and 19b should be the same since the values of  $(\ell/\delta_{L0})$  for the two experiments are similar. To compare the slopes, it is noted that Fig. 11 of Ref. [14] indicates that their brush thickness was approximately 4.2 times the integral scale. It follows that  $\Sigma_{\max} \delta_T$  is approximately 4.2 times the value plotted in Fig. 19b. Therefore the slope of the curve in Fig. 19b (for  $u'/S_{L0}$  less than 3) is about 2.5 times larger than the slope of the lower

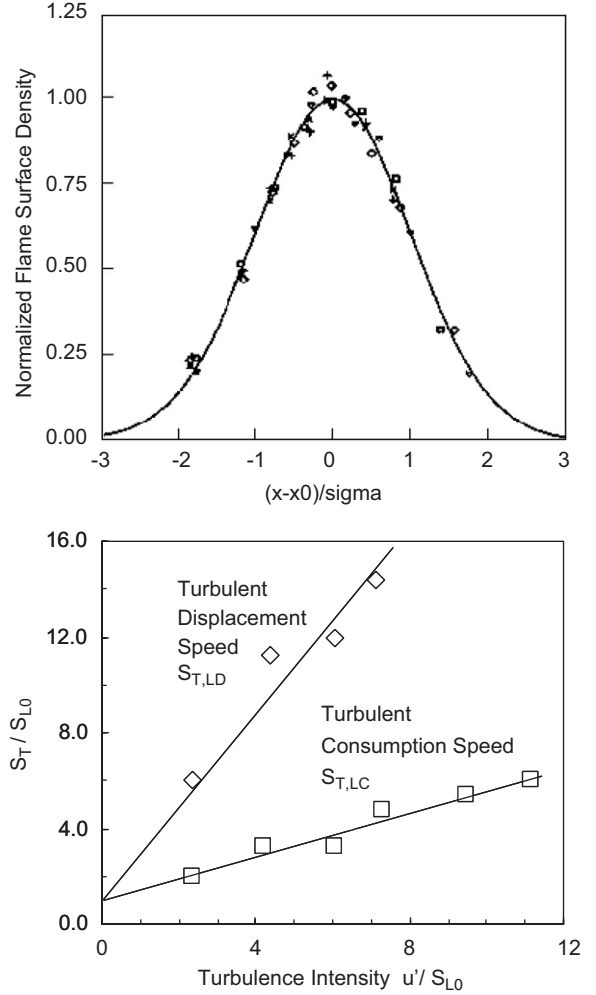


Fig. 18. Measured flame surface densities and consumptions speeds of Shepherd and Cheng [13] in their low-swirl flat flame designated SWF26;  $\Sigma_{\max}$  is approximately  $0.22 \text{ mm}^{-1}$  and sigma is  $20 \text{ mm}$ . Consumption speed is determined by integrating  $\Sigma$  across the brush.

curve in Fig. 18b. It can be concluded that even though flat turbulent flames are achieved in Refs. [13] and [14], the consumption speeds of the two flames are not the same for the same values of  $(u'/S_{L0})$  and  $(\ell/\delta_{L0})$ . Even though the mean isolines are flat, the streamlines diverge and there is a strong adverse pressure gradient which may differ in the two experiments. There also may be some geometrical factors that affect the freedom of the reaction layers to oscillate in space which limits the brush thickness or the degree of wrinkling. Flat turbulent flames provide much useful information but the evidence indicates that no premixed turbulent flame is truly geometry-independent. To realistically simulate an experiment, the specific boundary conditions of that experiment should be included.

DNS computations of some profiles of surface density appear in Figs. 15 and 20. Bell et al. [1] simulated the Bunsen experiment of Filatyev et al. [53]; their computation was 3-D, highly resolved, and included complex

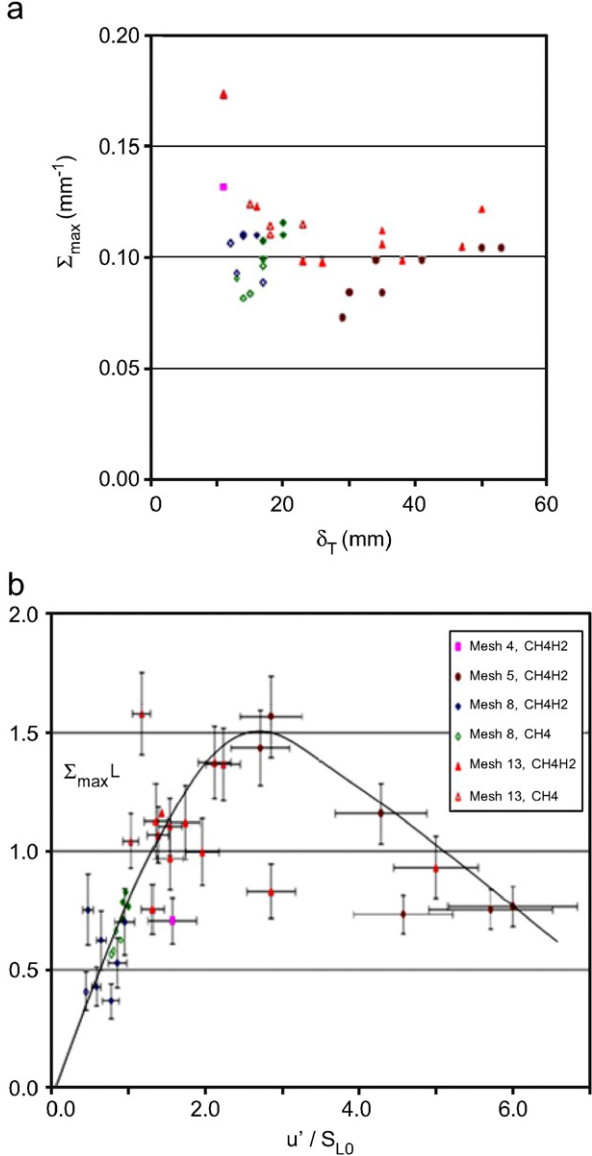


Fig. 19. Measured values of  $\Sigma_{\max}$  and  $(\Sigma_{\max} \ell)$ , where  $\ell$  is the integral scale, in a flat flame that was stabilized in the diffuser burner of Lawn and Schefer [14]. Measured brush thicknesses were correlated by the relation:  $\delta_T = 4.2 \ell$ . Solid curve in lower figure was added for clarity.

chemistry. The profiles of Bell et al. in Fig. 15e can be compared directly to the measurements that appear in Fig. 15d. In both cases the thin solid line has two distinct sharp peaks that reach a value of  $0.2 \text{ mm}^{-1}$ . This thin line corresponds to values of  $\Sigma$  determined at an axial location of 3 mm. The thick solid line represents values at an axial location of 4 cm. The peak values of this curve are about  $0.15 \text{ mm}^{-1}$  for both the computations and experiment. Farther downstream at 7 cm, the lowest curves have a peak value of only about  $0.05 \text{ mm}^{-1}$ . Because the inlet boundary conditions in the experiment are not perfectly symmetric, the properties of the brush on the right differ somewhat from the brush on the left. The experimental profile at  $x = 4 \text{ cm}$  (the thick line) is considerably narrower than that of the DNS. Better agreement would be expected if the

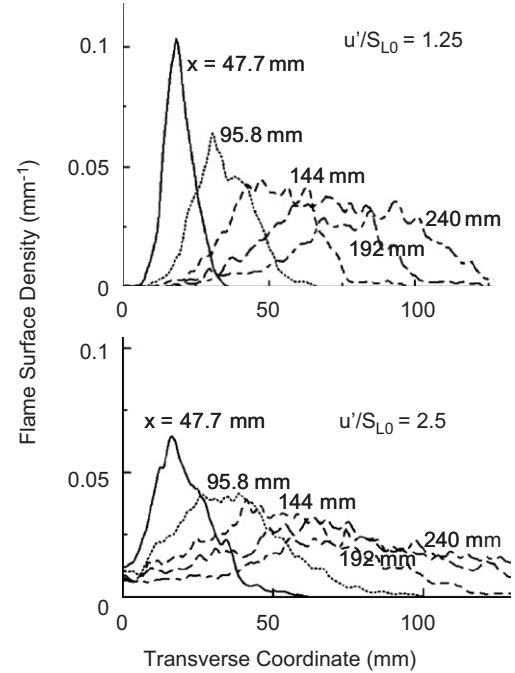


Fig. 20. Surface density computed using DNS for a V-flame geometry by Domingo et al. [87].

boundary conditions of the experiment and the DNS are more carefully matched. In Ref. [1] the only the spatially averaged values of  $U$ ,  $u'$  and the streamwise integral scale at the inlet boundary were matched. No attempt was made to match the exact inlet profiles of  $U$ ,  $u'$ ,  $v'$ ,  $\ell_x$ ,  $\ell_y$ ,  $\ell_z$  and the power spectrum of the turbulence. Fig. 20 is a plot of DNS results of Domingo et al. [87] for a V-flame. Their DNS included complex chemistry but was limited to a 2-D grid, whereas their LES was a fully 3-D computation. The profiles in Fig. 20 display trends that are similar to the V-flame measurements in Fig. 14. However, the operating conditions were not matched so the experiment has a much narrower brush and a much larger value of  $\Sigma_{\max}$  than the computation.

In Fig. 21 surface density values are plotted which were computed using the discrete-vortex model of Lam et al. [92]. The case that is labeled  $M$  corresponds to a moderate level of velocity fluctuations ( $u'/U = 7\%$ ) and is selected to simulate the V-flame experiment of Shepherd [82]. The authors find that their results are in reasonably good agreement with the experiment; they report that the integral of  $\Sigma$  across the brush yields a normalized consumption speed of 1.38. Fig. 21 shows that as the turbulence level is doubled their computed value of  $\Sigma_{\max}$  actually decreases slightly, but the brush becomes much thicker. One can find many computations of surface density that have been obtained using the CFM. For example, results reported by Prasad and Gore [26] appear in Fig. 22. The three curves shown correspond to different models for the source term in the equation for surface

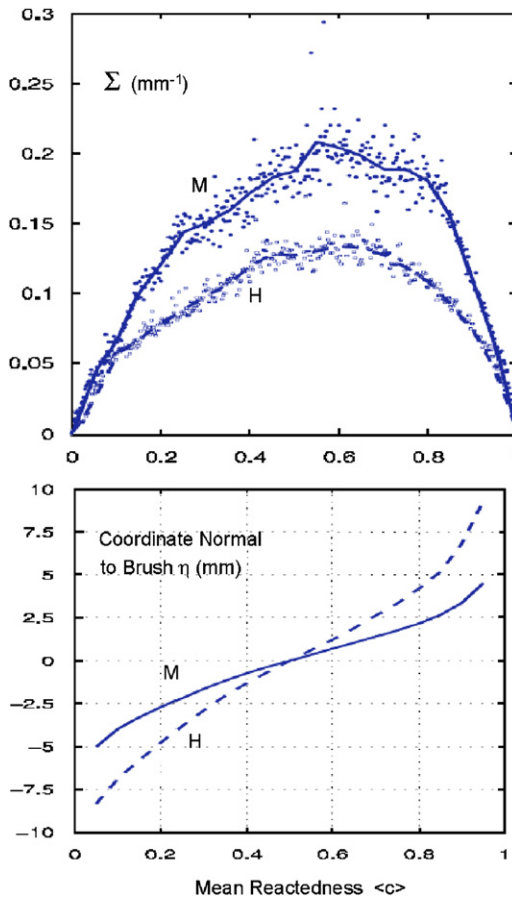


Fig. 21. Surface density computed in the V-flame of Lam et al. [92] using a discrete vortex method. Curves  $M$  = moderate turbulence level ( $u'/U = 7\%$ ); corresponds to experiment of Shepherd [82]. Curves  $H$  = high turbulence level ( $u'/U = 14\%$ ). For case  $M$  the authors report that the integral of  $\Sigma$  across the brush yields  $S_{T,LC}/S_{L0} = 1.38$ .

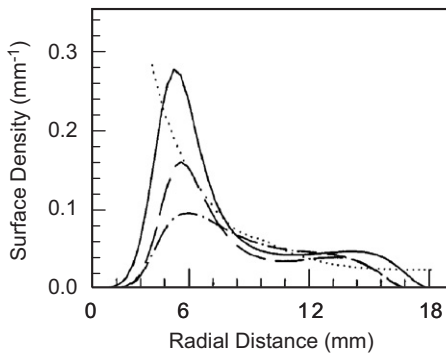


Fig. 22. Computed profiles of surface density for a Bunsen flame; the coherent flamelet model was used by Prasad and Gore [26]. The three curves correspond to different models used to determine the source term in the equation for flame surface density.

density. It was concluded that one of the three models is superior because it resulted in a global consumption speed that resulted in good agreement between the computed and measured height of the Bunsen cone.

### 3.2. Brush thickness ( $\delta_T$ )

The brush thickness  $\delta_T$  indicates the spatial region over which the reaction layers are located, so it is important that numerical simulations be assessed to insure that they predict realistic values of  $\delta_T$ . Fig. 23 is an example of data reviewed by Lipatnikov and Chomiak [37] that shows that the measured brush thickness in a Bunsen burner increases in a nonlinear manner with the downstream distance. Ref. [37] also reviews the results of Goix et al. [94] and Renou et al. [83] and concludes that Taylor's theory of turbulent diffusion [93] adequately explains the brush thickness measurements. It is often assumed that  $\delta_T^2$  is proportional to the product of the turbulent diffusivity ( $u'\ell$ ) and time, so that

$$\delta_T = A(u'\ell)^{1/2} t^{1/2}. \quad (27)$$

The time  $t$  in Eq. (27) is the convection time  $x/U$  for Bunsen and rod stabilized burners, and for spherical flames  $t$  is the time measured from the ignition event. Results in Ref. [37] agree with Eq. (27) if the time ( $t$ ) is larger than the large eddy turnover time ( $\ell/u'$ ). For times less than the large eddy turnover time, Taylor's theory predicts that  $\delta_T$  should be proportional to  $u't$  and the integral scale is no longer relevant. Both of these examples are limiting cases of the more general statement of Taylor's theory, which is [93]

$$\delta_T = (2u'\ell t)^{1/2} \left\{ 1 - \frac{\ell}{u't} \left( 1 - \exp\left(\frac{-tu'}{\ell}\right) \right) \right\}^{1/2}. \quad (28)$$

Some researchers have reported that their measured values of  $\delta_T$  scale as  $t^{1/2}$  while others find that  $\delta_T$  is proportional to time [37]; in both cases the measurements display reasonable agreement with Eq. (28) for simple geometries. For complex geometries Eq. (28) may not be adequate because Taylor's theory does not account for heat release and it assumes that the turbulence is homogeneous so  $u'$  and  $\ell$  do not vary in space or time.

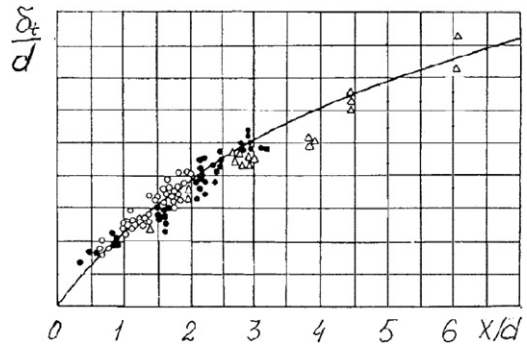


Fig. 23. Turbulent brush thickness, normalized by Bunsen burner diameter, measured by Prudinkov [95] as reported in Lipatnikov and Chomiak [38]. Benzene–air mixtures, mean velocities from 35 to 75 m/s, burner exit diameter  $d = 150$ –200 mm, equivalence ratios from 0.77 to 2.0.

### 3.3. Surface area of flamelets—proportional to turbulent burning velocity?

In this section some recent results are reviewed which provide evidence that Damköhler's concept is valid in the flamelet regime: turbulence increases the turbulent burning velocity primarily because it increases the reaction surface area. Validation of this idea has been provided by two recent DNS studies of a flat turbulent flame in a box by Bell et al. [95] and Hawkes and Chen [96]. They considered a flat turbulent flame that has 1-D mean properties and were able to compute the magnitude of both sides of the equation:

$$\frac{\dot{m}_R / (\rho_R A_{\bar{c}=0.5})}{S_{L0}} = I_0 \int_{-\infty}^{\infty} \Sigma d\eta. \quad (29)$$

Eq. (29) is a combination of Eqs. (15) and (16) and it is valid if the local and global consumption speeds are the same. The left side is the normalized global consumption speed; it contains the known mass per second per unit area of reactants flowing into the DNS computational domain. Bell et al. [95] used DNS results to compute the integral in Eq. (29) which is  $(A_T/A_L)$ . They selected a lean methane-air flame ( $\phi = 0.8$ ) which they believed should be diffusionally neutral. They found that at two different turbulence levels the left side of Eq. (29) was 1.35 and 1.85 and the integral had values of 1.23 and 1.64, respectively. The ratio of these numbers is  $I_0$  which was 1.09 and 1.12 for the two turbulence levels. Therefore their observed increase in the global consumption speed is almost entirely due to the increase in surface area. Hawkes and Chen [96] computed  $I_0$  in a different way; they used Eq. (3) and integrated the volumetric reaction rate across each layer for a lean methane-air flame. Their computed values of  $I_0$  for four different turbulence levels were 1.10, 0.95, 0.98 and 1.08. This implies that their flamelets are propagating at a velocity nearly equal to  $S_{L0}$ , on average, so that  $S_T/S_{L0}$  is nearly equal to  $A_T/A_L$  and their DNS conditions can be inferred to be in the flamelet regime. In contrast, Chen and Bilger [66] state that their Bunsen experiment was operated in both the flamelet and the non-flamelet regimes. While they do not compare  $S_T/S_{L0}$  to  $A_T/A_L$  directly, they analyze their measurements and conclude that  $S_T/S_{L0}$  is significantly greater than  $A_T/A_L$  in the non-flamelet regime. They suggest that the burning velocity along their

flame surface is larger than the unstretched value in this regime.

While DNS is capable of providing values of the stretch factor  $I_0$ , experimental determination of  $I_0$  has not yet been possible.  $I_0$  could be measured using Eq. (29); the left side could be evaluated for a Bunsen burner since the mass flow rate of the reactants is known. The integral in Eq. (29) could be evaluated by integrating measured values of  $\Sigma$  over the entire brush. Filatyev et al. [53] estimated the integral in Eq. (29) to be the quantity  $(P_T/P_L)^2$  where  $P_T$  is the perimeter of the wrinkled reaction layers that were imaged in a 2-D laser sheet. They found that increasing the turbulence level caused the global consumption speed (the left side of Eq. (29)) to increase by a factor of four, and there was approximately a corresponding fourfold increase in  $(P_T/P_L)^2$ . These findings also are indications that  $S_T/S_{L0}$  is approximately equal to  $A_T/A_L$ .

## 4. How well can we predict the turbulent burning velocity?

Many models in the past have failed to provide adequate predictions of turbulent burning velocity, but now some convincing simulations are being performed using DNS and LES. The advantage of DNS is that the three-dimensional geometry and boundary conditions of a specific experiment are simulated. In addition, DNS includes complex chemistry and differential diffusion and it employs no empirical constants.

### 4.1. Burning velocities predicted by DNS

**Table 5** lists some impressive new DNS efforts that include detailed chemistry and employ 3-D grids which resolve the Kolmogorov scale. Bell et al. simulated a Bunsen flame [1], a V-flame [2] and a flat flame [95] in a box. Sankaran et al. [3] simulated a preheated Bunsen flame and Tanahashi et al. [75] considered a flat flame in a box. The first two studies in **Table 5** are noteworthy because they simulate the geometry and boundary conditions of the experiments of Refs. [2] and [53]. **Fig. 1** showed some of the computed flamelet structure. In Figs. 24–26 DNS results of Bell et al. [1] are compared to the slot Bunsen experiment of Filatyev et al. [53]. In both studies the reactants were stoichiometric methane and air that issued from a 25 mm by 50 mm slot at a mean velocity of

Table 5

Recent DNS of premixed turbulent combustion that include complex chemistry and employ high-resolution 3-D grids

Authors	Flame type	Fuel	Grid (μm)	$u'/S_{L0}$	$Re_f = u' \ell / v$
Bell et al. [1]	Bunsen	Methane	79	0.80	104
Bell et al. [2]	V-flame	Methane	312	1.1	50
Bell et al. [95]	Flat	Methane	62	4.3	100
Sankaran et al. [3]	Bunsen	Methane	20	10	83
Tanahashi et al. [75]	Flat	Hydrogen	20	3.4	153

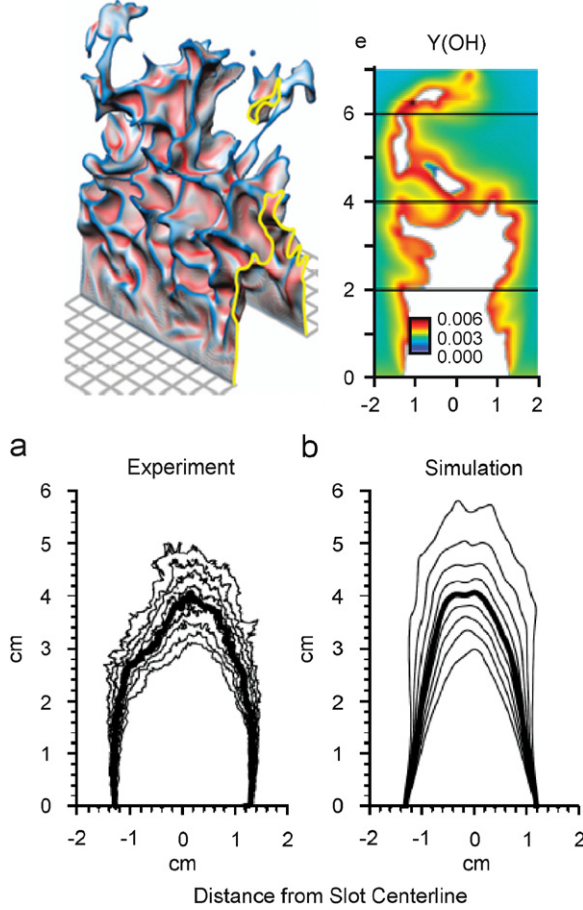


Fig. 24. Evidence that the DNS of Bell et al. [1] can correctly predict the turbulent burning velocity that was measured in the Bunsen flame of Ref. [53]. The height of the  $\bar{c} = 0.5$  contour (thick line) is 4 cm in both the DNS and the experiment, yielding  $S_{T,CG}/S_{L0}$  of 2.45 and 2.55 for the simulation and experiment, respectively. Top left: the computed 1684 K isotherm that occurs where the heat release is a maximum; top right: OH mass fraction.

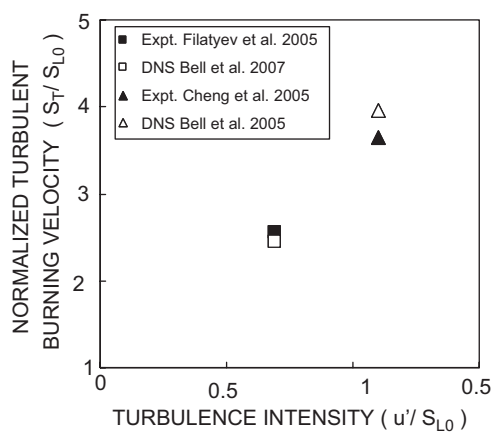


Fig. 25. Comparison of turbulent burning velocities predicted by DNS of Bell et al. [1,2] to measured values for Bunsen geometry of Filatyev et al. [53] and V-flame of Cheng [2]. The DNS matched the experimental geometry and boundary conditions and included complex methane chemistry.

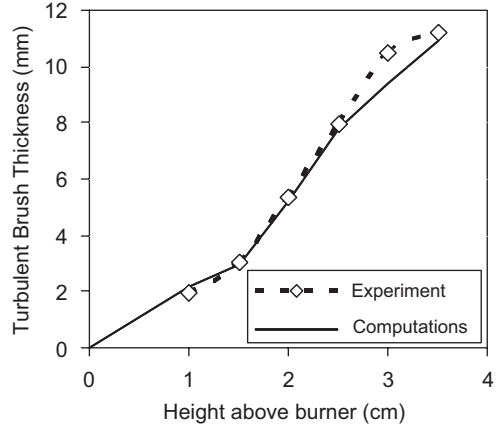


Fig. 26. Comparison of the brush thickness computed by DNS of Bell et al. [1] (solid line) compared to measurements in the Bunsen flame [53].

3 m/s;  $u'/S_{L0}$  was 0.69 and the integral scale was 5.2 mm. The DNS also simulated two side burners which provided a surrounding stream of hot products to eliminate unwanted shear layers in the experiment. The DNS employed adaptive mesh refinement to resolve the Kolmogorov scale and included a 20 species, 84 reaction chemistry mechanism derived from GRI-Mech 1.2. The thick lines in Fig. 24a and b are the measured and computed values of the  $\bar{c} = 0.5$  contour, respectively. This contour has a height of approximately 4 cm for both the DNS and the experiment. The values of normalized consumption speeds  $S_{T,CG}/S_{L0}$  that were determined using Eq. 15 were 2.45 and 2.55 for the DNS and the experiment, respectively. These two values of burning velocity are plotted in Fig. 25. The difference of 4% could be due to differences in boundary conditions or experimental uncertainties. Centerline values of  $u'$ ,  $U$  and the streamwise integral scale were matched, but several quantities were not matched, including the lateral velocity fluctuations  $v'$ , the lateral integral scale, and the power spectrum of the turbulence. In the previous section it was shown in Fig. 15 that the flame surface density profiles predicted by the DNS were in general agreement with the experiment. Fig. 26 indicates that the brush thickness of the Bunsen experiment and the DNS are in agreement.

For the case of a V-flame, DNS results reported by Bell et al. [2] were compared to the experiment of Cheng and Shepherd and some results are seen in Fig. 27. Methane-air reactants at  $\phi = 0.7$  exit a 5 cm circular nozzle with a mean velocity of 3 m/s;  $u'/S_{L0}$  was 1.1 and the integral scale was 3.5 mm. A 2 mm diameter rod stabilized the flame. The computed half-angle ( $\theta/2$ ) of the brush is compared to the experiment in Fig. 27b. An approximate value of the normalized displacement speed ( $S_{T,DL}/S_{L0}$ ) is  $(U/S_{L0}) \sin(\theta/2)$ , which is equal to 3.95 for the DNS and 3.62 cm/s for the experiment. The two values differ by 19%. These two values of burning velocity are plotted in Fig. 25. The computed brush thickness in Fig. 27c also agrees with measured values.

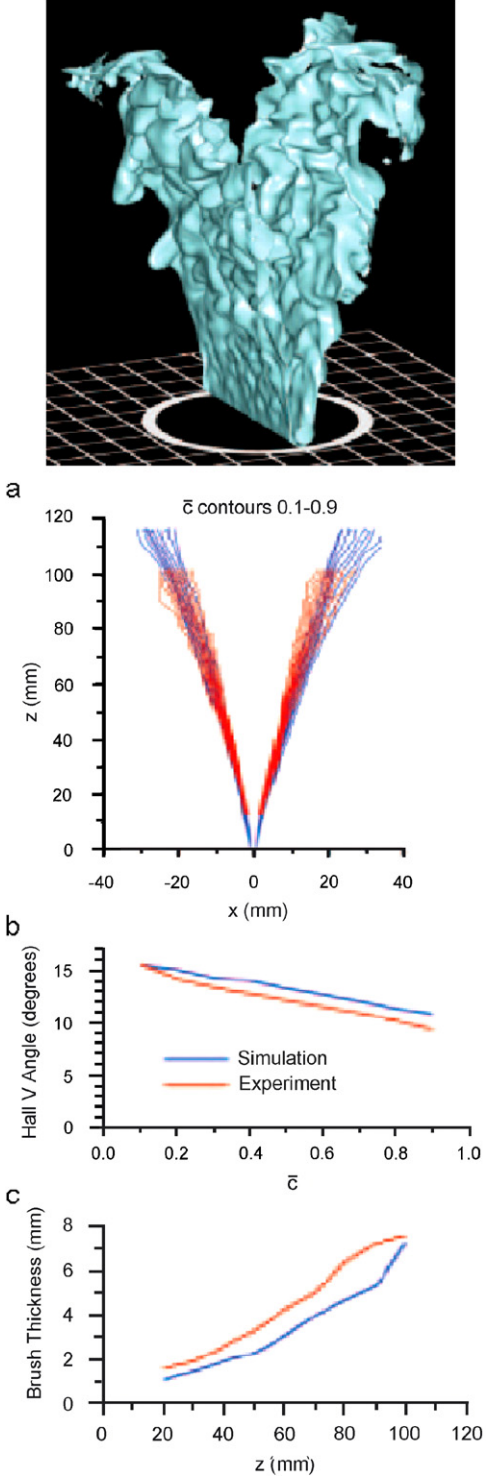


Fig. 27. Evidence provided in Bell et al. [2] that their DNS can predict a realistic turbulent burning velocity for a V-flame.  $S_T$  is proportional to the sine of the half-angle, and (b) verifies that the DNS half-angle agrees with experiment, as does the brush thickness (c).

It can be concluded that it is now possible to use DNS to predict turbulent burning velocities that differ by 4–19% from values measured in experiments that have simple geometries [1,2]. To achieve this level of accuracy,

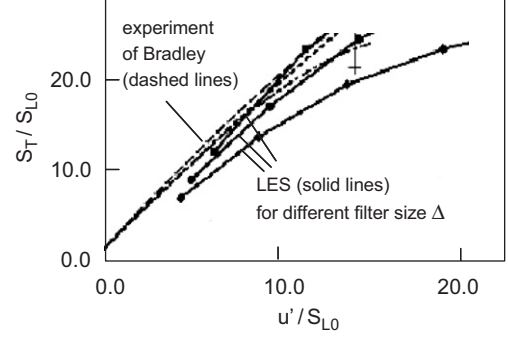


Fig. 28. Comparison of turbulent burning velocity predicted by the LES of Charlette et al. [34] to experimental data of Bradley [42].

the simulations require measured values of the inlet boundary conditions, including inlet profiles of mean velocity, velocity fluctuations and the streamwise integral scale ( $\ell$ ). To improve this level of accuracy it may be necessary to specify inlet profiles of lateral integral scales and the power spectrum of the inlet velocity fluctuations.

#### 4.2. Burning velocities predicted by LES and the CFM

Three types of LES methods that provide values of the turbulent burning velocity were described by Charlette et al. [34], Hawkes and Cant [32] and Pitsch [4]. Fig. 28 indicates some values of  $S_T$  from Charlette et al. [34] for a flat flame in a box. These authors compare their finding to some of Bradley's correlations of experimental data [42] and agreement is observed. It is noted that their computed curves also display a “bending” that is seen in many experiments. To obtain these results Charlette et al. modeled their subgrid turbulent diffusion with a Smagorinsky relation, and their mean volumetric reaction rate  $\bar{\omega}$  was set equal to

$$\bar{\omega} = \rho_R S_{L0} I_{0,SG} \Sigma_{SG}. \quad (30)$$

After the subgrid flame surface density was modeled, Eq. (30) becomes

$$\bar{\omega} = \rho_R \bar{c} (1 - \bar{c}) \exp(E/RT)(A/F) \left( 1 + \frac{\Gamma_K u'_\Delta}{S_L} \right)^\beta. \quad (31)$$

Eq. (31) is based on an algebraic power law relation for  $\Sigma_{SG}$  which was derived by Charlette et al. by starting with the flame surface density balance equation and setting the production term equal to the destruction term. The quantity A is the Arrhenius pre-exponential constant, F is a thickening factor, and  $\Gamma_K$  is a modified version of the original the stretch efficiency function [19]. The subgrid turbulent velocity  $u'_\Delta$  was related to the resolved vorticity field using an equation that is proposed in Ref. [34], and the exponent  $\beta$  was set to 0.5 to achieve best agreement between computations and measurements. A different LES subgrid model was developed by Hawkes and Cant [32] who included Eq. (30) but did not use Eq. (31). They chose to solve a differential equation that is similar to Eq. (10) to

compute  $\Sigma_{SG}$  and their computed values of  $S_T/S_{L0}$  were as large as 2.6 for the case of a flat turbulent flame in a box.

A third type subgrid model is one that involves the  $G$ -equation and has been developed by Pitsch [4,35]. Fig. 1d showed the computed flame structure that was reported in Ref. [4] for a geometry that is identical to the Bunsen experiment of Chen et al. [7]. The computed mean temperature contours were found to agree with the measurements. It also can be inferred that the LES accurately predicts the turbulent burning velocity because the flame height computed in Ref. [4] differs by only 6% from the measured value, and flame height is directly proportional to burning velocity. The  $G$ -equation analysis previously was developed to simulate instabilities that create cusps in laminar flames by Kerstein et al. [97] and Sivashinsky [98]. Ashurst [99] and Peters [9,30,31] have done extensive work to apply the  $G$ -equation to turbulent flames. Some simple solutions to the  $G$ -equation are discussed in Ref. [9]. The  $G$ -equation LES approach treats the reactants as a non-reacting and constant density gas that has a turbulent velocity field  $\mathbf{v}(x,y,z,t)$  which is determined from the unsteady solution to the filtered Navier Stokes equations. Each point on the interface is convected by the resolved velocity field and each point propagates in the normal direction at a speed that must be specified by some assumed relation. The  $G$ -equation provides a method to track the wrinkled interface. It does not contribute any new physics and it is not a fundamental conservation equation. It does accurately represent the kinematics of the wrinkled interface if the formulas for the local propagation speed and gas expansion at the interface are realistic. For example, if an interface has a sinusoidal shape and each point propagates normal to the surface, Ref. [99] shows that the  $G$ -equation correctly predicts that cusps must form and the wrinkles are attenuated by the propagation of the surface; this is called kinematic restoration or Huygens's principle. The quantity  $G$  is a scalar which is defined near the interface only; away from the interface  $G$  is not defined uniquely so it has no physical significance. In this way  $G$  is different from the reactedness ( $c$ ) which is defined far from the interface and obeys fundamental conservation laws and boundary conditions. A general form of the  $G$ -equation is [35,100]

$$\frac{\partial G}{\partial t} + \mathbf{v} \cdot \nabla G = (S_L + S_{T,SG})|\nabla G| + \left(\frac{\rho_R}{\rho_P} - 1\right) \frac{S_{L0}}{2} I(G). \quad (32)$$

The unsteady resolved-scale velocity field is  $\mathbf{v}$  and the stretched laminar burning velocity  $S_L$  is determined from

$$S_L = S_{L0}(1 - \mathcal{L}\mathcal{K}), \quad (33a)$$

$$\mathcal{K} = -\nabla \cdot \left( \frac{\nabla G}{|\nabla G|} \right). \quad (33b)$$

The Markstein length ( $\mathcal{L}$ ) is proportional to the Markstein number ( $Ma_L$ ) and  $\mathcal{K}$  is the local curvature of the

interface. Eq. (32) is used to determine the wrinkled, unsteady resolved scale interface ( $G = G_0$ ), which propagates normal to itself at a speed ( $S_L + S_{T,SG}$ ) where  $S_{T,SG}$  is the subgrid contribution to the turbulent burning velocity. The idea is that this resolved-scale wrinkled interface is a “thick” and moderately wrinkled spatially filtered version of the true interface. The true interface is highly wrinkled but cannot be resolved by the grid. Pitsch [35] assumed that  $S_{T,SG}/S_{L0}$  is the ratio of the area of the true interface to the area of the resolved scale interface and he set this ratio equal to

$$S_{T,SG}/S_{L0} = A \frac{A \cdot S_L}{D} + \left( B \left( \frac{A \cdot S_L}{D} \right)^2 + C \left( \frac{D_T}{D} \right) \right)^{1/2}, \quad (34)$$

where  $A$ ,  $B$  and  $C$  are constants and  $D$  is diffusivity. Pitsch argues that this function behaves in the classical manner that was suggested by Damköhler. At the thin flamelet limit  $\delta_{L0}$  is much smaller than  $A$  and Eq. (34) predicts that  $S_T$  is proportional to  $(u'/S_{L0})$ . At the thick flamelet limit  $\delta_{L0}$  is larger than  $A$  and Eq. (34) indicates that  $S_T$  is proportional to  $(D_T/D)^{1/2}$ .

The last term in Eq. (32) accounts for the gas expansion at the interface. The velocity field  $\mathbf{v}(x,y,z,t)$  corresponds to that of non-reacting, constant density reactants upstream of the interface. If no model for gas expansion is included then unrealistic values of interface wrinkling would be predicted. Sivashinsky [98] and Ashurst [99] modeled gas expansion by distributing a series of volume sources along the interface that have sufficient strength to satisfy the jump condition ( $\rho_R U_{R,N} = \rho_P U_{P,N}$ , where  $N$  indicates the direction normal to the interface). The volume sources create an irrotational velocity field that is superimposed upon the original constant-density turbulence flow field.  $I(G)$  in Eq. (32) is the Sivashinsky integral [98]. The new velocity added by the gas expansion is the integral sum of the contributions from every volume source along the interface. The  $G$ -equation approach does attempt to account for complex chemistry and differential diffusion in a simple manner; these processes determine the value of Markstein number in Eq. (33).

Several advantages of the  $G$ -equation approach are discussed in Refs. [9] and [35]. The approach is a computationally efficient way to calculate the shape of a wrinkled unsteady surface. The computation effort is focused on resolving the interface structure while no computational effort needs to be expended to solve for chemical reaction source terms since  $S_L$  and  $S_T$  are modeled. The  $G$ -equation automatically insures that the wave propagates normal to itself. The  $G$ -equation has been demonstrated to accurately represent the kinematics of laminar flames (i.e., instabilities, wrinkling, cusp formation and merging). One disadvantage of the  $G$ -equation approach is that it is not known if the propagation speed of the spatially filtered interface can be realistically represented by general formulas such as Eqs. (33) and

(34). Eq. (33) has been verified in quasi-steady laminar experiments but not under highly unsteady conditions. The theory of flame stretch predicts that  $S_L$  will increase (if positive stretch is applied and Markstein number is negative) but this increase cannot continue indefinitely as the stretch rate is made arbitrarily large. Eventually  $S_L$  must decrease and extinction occurs, and this limit is not considered when Eq. (33) is used. Gas expansion also can be a problem. The Sivashinsky integral in Eq. (32) is based on the idea that the flame can be represented by volume sources on the interface which create an irrotational velocity field. This approach neglects any flame-generated vorticity. Local flame extinction could lead to other problems because the level set approximation is not valid unless the gas consists of only reactants and products. As with any LES, it is important that results be demonstrated to be independent of the selected filter size  $\Delta$ .

RANS models also have provided several predictions of turbulent burning velocity, some of which are shown in Figs. 29–34. Peters [30] included the time-averaged  $G$ -equation in his RANS model and Fig. 29 indicates the level of agreement between his predictions and some measured burning velocities. Fig. 30 shows that the integral scale ( $\ell$ ) plays an important role in his model.  $S_T$  is predicted to scale as  $\ell^n$  where  $n$  is between 0.3 and 0.5. This result is in general agreement with Bradley's correlation [42]. Another RANS approach is the CFM that has been described by Veynante et al. [18]. CFM evolved from concepts first developed by Bray et al. [7] and later work by Candel, Poinsot, Meneveau, Veynante, Baritaud and others [18–24,46,48]. It is an unsteady RANS model that is contained within the KIVA code that is often used to simulate internal combustion engines [21,22]. The conservation equations are time-averaged over time scales that

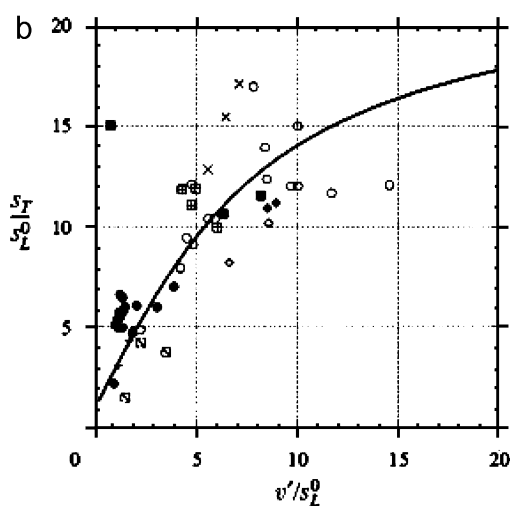


Fig. 29. Comparison of turbulent burning velocity predicted by the RANS-G-equation model of Peters [30] (solid line) to the measurements of Abdel-Gayed et al. [43]. The model simulates a planar turbulent flame having one-dimensional mean properties.

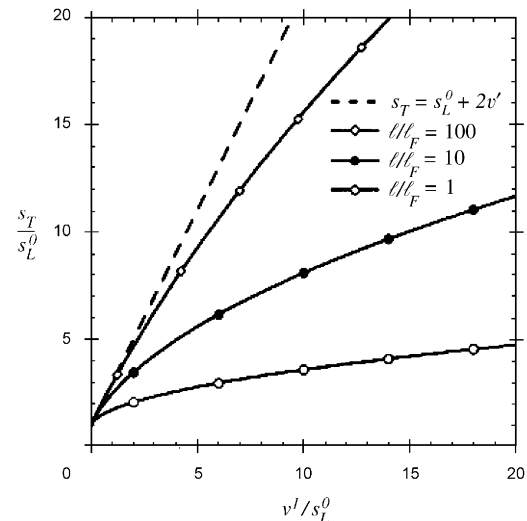


Fig. 30. Predictions of RANS-G-equation model of Peters [30] showing that turbulent burning velocity increases as the integral scale is increased. This trend is in agreement with the correlation of measured values reported by Bradley [42].

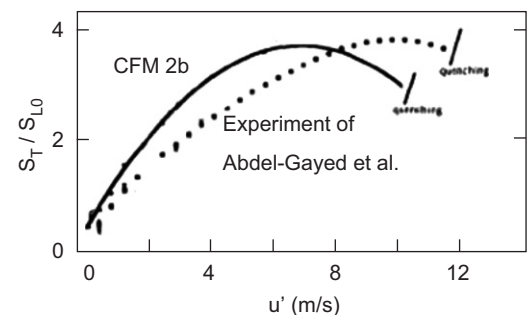


Fig. 31. Results of Duclos et al. [24] showing that the coherent flamelet model can predict the turbulent burning velocity data of Abdel-Gayed et al. [43]. Note that CFM predicts the correct “bending” of this curve that is caused by the loss of flame surface area due to flamelet merging and quenching at large turbulence intensities. The model simulates a planar turbulent flame having one-dimensional mean properties.

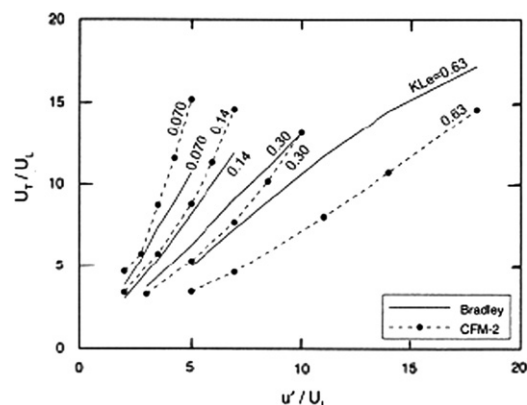


Fig. 32. Comparison of turbulent burning velocity predicted by the coherent flamelet model of Choi and Huh [28] to the measurements of Bradley [42]. The model considers a spherical expanding turbulent flame in a chamber.

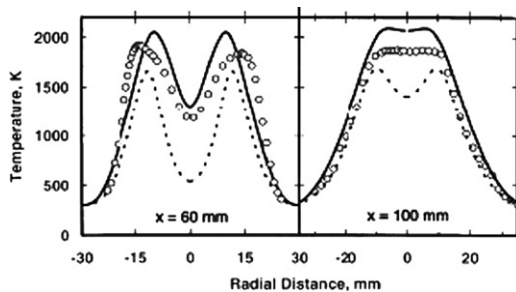


Fig. 33. (a) Comparison of temperature profiles predicted by the coherent flamelet model of Prasad and Gore [26] to thermocouple measurements made in an identical turbulent Bunsen flame. The agreement indicates that the model is predicting a realistic flame height (where the temperature profile is no longer bimodal) and a realistic turbulent burning velocity. (b) Flame surface density across the brush of the Bunsen flame computed by Prasad and Gore.

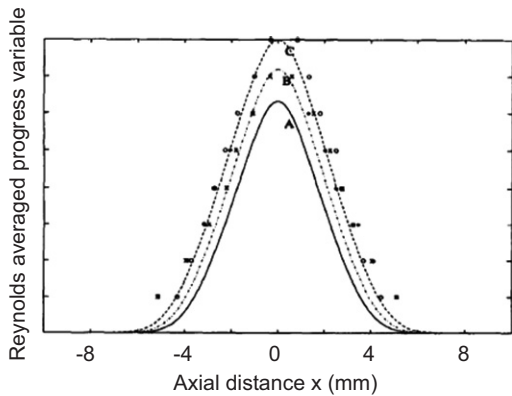


Fig. 34. Comparison of mean reactedness computed by the coherent flamelet model of Wu and Bray (solid and dashed lines) to the measured values of Kostiuk and Bray [12]. CFM predicts a realistic mean location of the flame within the counterflow velocity field, indicating that the predicted turbulent burning velocity is in agreement with the experiment.

are associated with the turbulence, so CFM cannot provide instantaneous images of the wrinkled flame surface, such as those predicted by LES. However, it does resolve the time scales associated with piston movement within an engine. Profiles of  $\Sigma$  are computed from the flame surface density equation (Eq. (10)) and its source terms (Eqs. (13) and (14)). These profiles are integrated across the brush using Eq. (16) to determine the turbulent burning velocity.

Fig. 31 indicates the results of Duclos et al. [24] for a turbulent flame in a box. A particular model of the source term in Eq. (10) was selected to create a model that he named CFM2b that gave best agreement with the measurements of Abdel-Gayed et al. [43]. The computed curve in Fig. 31 displays the nonlinear bending that was observed in the experiment. The bending predicted by the model results from the fact that the merging rate is assumed to be proportional to  $\Sigma^2$ , so for large turbulence intensities the rate of surface destruction due to merging is larger than the rate of creation due to stretch. For a

spherical flame Fig. 32 shows the results of the CFM of Choi and Huh [28]. Relatively good agreement with measurements [42] is achieved. For the case of a Bunsen flame, the CFM results in Fig. 33 were reported by Prasad and Gore [26]. Their predicted height of their Bunsen cone is approximately 100 mm since Fig. 33 shows that two peaks appear in the temperature profile at  $x = 60$  mm but they merge together at  $x = 100$  mm. They conclude that their predicted cone height agrees with the experiment. Since the Bunsen cone height is inversely proportional to  $S_T$ , Fig. 33 indicates that the predicted turbulent burning velocity is approximately in agreement with the experiment. A counterflow premixed twin-flame was modeled using CFM by Wu and Bray [12] and their results appear in Fig. 34. The mean reactedness reaches a maximum value near the stagnation point ( $x = 0$ ) as expected, and the predicted profile is seen to agree with the measurements. In a twin-flame burner the reactants flow toward each other and two flames surround the products which exist near the stagnation point. Since the model predicts that the twin flames are located at the same positions in the counterflow velocity field as in the experiment, this implies that the predicted turbulent burning velocity agrees with the experiment.

One fundamental advantage of the CFM approach is that it separates the effects of large-scale velocity gradients (which depend on the geometry of shear layers and recirculation zones) from small-scale effects that are modeled in a more universal manner. The model of Prasad and Gore [26] specifically includes large-scale and small-scale source terms to the flame surface density balance. Complex geometries can be simulated; for example, a diesel-engine geometry was considered by Musculus and Rutland [21]. Another advantage to the CFM approach is that the role of hydrodynamic instabilities can be included. Paul and Bray [101] modeled the additional wrinkling caused by hydrodynamic instabilities by adding an additional source term to the equation for the surface density (Eq. (10)). The CFM approach includes thermodiffusive effects and complex chemistry in the stretch factor  $I_0$  that appears in Eq. (1). One concern is that the source terms in Eq. (10) are modeled in a simple and universal manner and these source terms depend only on three parameters ( $\Sigma$ ,  $u'/S_{L,0}$  and  $\ell/\delta_L$ ). This simple approach may not be adequate to account for the complex phenomenon such as flame–flame and flame–wall interactions that occur in engines.

It is clear from the above examples that impressive progress has been made in recent efforts to predict turbulent burning velocities for a variety of burners and engines. While DNS has been successful for a few simple laboratory geometries, there still is a need to systematically vary the turbulence levels and integral scales and then collect a DNS database of burning velocities for a single geometry. Little research has been done to determine if the empirical constants employed in LES and RANS models are geometry-independent.

### 4.3. Thermodiffusive (Markstein number) effects and the stretch factor $I_0$

The previous section described comparisons between simulations and experiments; nearly all comparisons were performed for reactant mixtures that are nearly diffusionally neutral. The reactants often chosen are methane and air having equivalence ratios between 0.7 and 1.0. To answer the question “how well can we predict the turbulent burning velocity?” it is necessary to first answer the question: “how important are thermodiffusive effects for fully turbulent conditions?” For the case of a laminar flame, thermodiffusive effects are characterized by a Markstein number ( $Ma_L$ ) that appears in the following relation:

$$\frac{S_L}{S_{L0}} = 1 - Ma_L \frac{K}{(S_{L0}^2/\alpha_0)}. \quad (35)$$

The history of the development of the theory of flame stretch is described in the review paper by Law and Sung [49].  $S_L$  is the stretched laminar burning velocity. In turbulent flames it is necessary to define two additional Markstein numbers:

$$\frac{S_{F,C}}{S_{L0}} = 1 - Ma_F \frac{K}{(S_{L0}^2/\alpha_0)}, \quad (36)$$

$$\frac{\bar{S}_{F,C}}{S_{L0}} = I_0 = 1 - Ma_T \frac{u'/\ell}{(S_{L0}^2/\alpha_0)}. \quad (37)$$

$Ma_F$  is the flamelet Markstein number and  $Ma_T$  is the turbulent Markstein number. It would be convenient if all three Markstein numbers were found to be equal, but there is not sufficient evidence to say if they are equal or not. For a flamelet the value of  $Ma_F$  would be expected to equal the laminar value ( $Ma_L$ ) if conditions are quasi-steady and the flamelet truly is analogous to a counterflow laminar flame. However, if the scalar gradients do not respond rapidly to the high frequency components of the imposed velocity gradients,  $Ma_T$  could be significantly smaller than  $Ma_L$ . The turbulent Markstein number relates the stretch factor  $I_0$  to the characteristic strain rate  $u'/\ell$  so there is no compelling reason to expect that  $Ma_T$  should equal  $Ma_L$ . Note that the right side of Eq. (36) contains the stretch rate  $K$  which can be positive or negative, while the right side of Eq. (37) contains only a characteristic stretch rate  $u'/\ell$  which is always positive. In addition, the left side of Eq. (37) contains a propagation speed that is averaged over time and space, so it represents the sum of the competing effects of positive and negative stretch. It might be expected that fuel-air equivalence ratios that lead to diffusionally neutral laminar flames ( $Ma_L = 0$ ) would also lead to neutral turbulent flames ( $Ma_T = 0$ ).

Figs. 35 and 36 illustrate values of  $Ma_L$  that have been measured for laminar flames [51,102–109]. For methane-air mixtures the curve in Fig. 35 has a positive slope, and for propane-air mixtures the slope of the curve in Fig. 36 is negative, which is consistent with the theory [49].

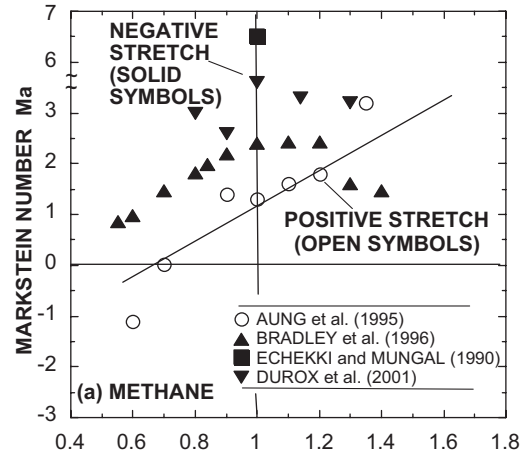


Fig. 35. Laminar flame Markstein numbers ( $Ma_L$ ) for methane–air counterflow and spherical geometries [51,102–109].

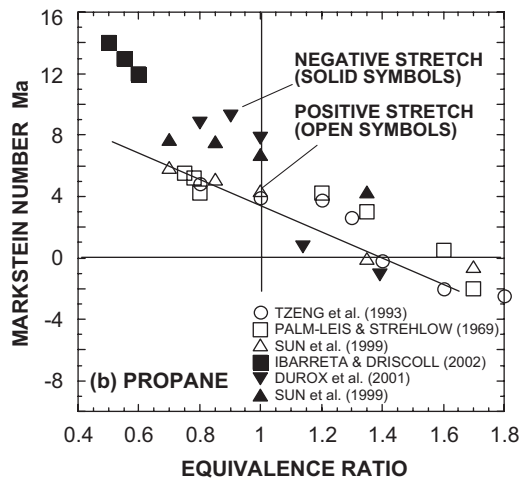


Fig. 36. Laminar flame Markstein numbers ( $Ma_L$ ) for propane–air counterflow and spherical geometries [51,102–109].

These two curves can be represented by

$$Ma_L = 3.3\phi - 2.3 \text{ methane–air}, \quad 0.5 < \phi < 1.4, \\ = -8.6\phi + 12.0 \text{ propane–air}, \quad 0.5 < \phi < 1.7. \quad (38)$$

Fig. 37 is a schematic diagram that helps to explain how thermodiffusive effects alter both the propagation speed and the flamelet surface area. Theory [49] predicts that lean hydrogen–air flames are diffusionally unstable. Consider the segment of a lean hydrogen–air flamelet that is near the dotted line in Fig. 37 and has a negative curvature—it is convex toward the products. Hydrogen will preferentially diffuse out of the reactants and make the reactants leaner as they approach the reaction zone. This causes a decrease in the local propagation speed so the segment near the dotted line will move farther away from the mean flame position. Conversely, a segment where the curvature is positive will propagate faster. It too will move farther away

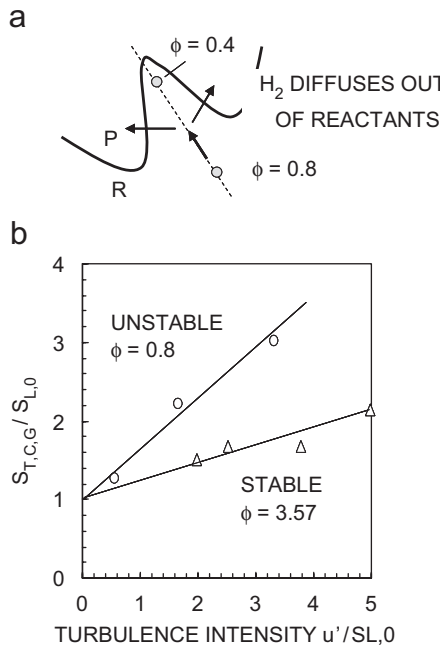


Fig. 37. (a) Schematic showing why lean hydrogen–air flames are unstable. Hydrogen diffuses away from the dotted line, so the rear portion of the wrinkle propagates more slowly and the front propagates more rapidly, which amplifies the wrinkle magnitude. (b) Measured turbulent burning velocities of lean and rich hydrogen–air turbulent jet flames of Wu et al. [110], showing that Markstein number effects are important even at large Reynolds numbers.

from the mean flame position. Thus, the initial wrinkle will be amplified, which illustrates how thermodiffusive effects play a role in the creation of flamelet surface area.

We now ask the question—does the theory of flame stretch apply to flames that experience very high levels of turbulence? The data reviewed in Section 2 indicate that the flamelet regime extends to Karlovitz numbers that exceed 20, which is larger than previous predictions. In the flamelet regime the molecular diffusion within the layers dominates over turbulent diffusion. Therefore it is not surprising that thermodiffusive effects (which are caused by molecular diffusion) are observed even when the turbulence intensity and the Karlovitz number are large. Fig. 37b is a plot of the measurements Wu et al. [110] that verify that thermodiffusive effects are significant for a Bunsen flame that is subjected to large velocity fluctuations ( $u'/S_{L,0} = 5$ ,  $Ka = 1–4$  based on Eq. (21),  $u' = 6–10$  m/s,  $u'\ell/v = 2300$ ). All conditions were held constant (including  $u'$  and  $\ell$ ) while two values of equivalence ratio (0.8 and 3.57) were considered. For these two values of  $\phi$  the values of  $S_{L,0}$  for the hydrogen–air reactants were the same. The lean (unstable) flame was noticeably more wrinkled and had much finer-grained wrinkles than the rich (stable) case. Fig. 37b shows that the turbulent burning velocity ( $S_{T,GC}$ ) of the lean case was twice as large as the rich case, indicating that even highly turbulent flames have a strong dependence on Markstein number. Additional evidence is provided by Bradley [42] who showed that measured values

of burning velocity display a strong dependence on Lewis number. He later decided to use Markstein number rather than Lewis number to correlate the data. The review paper of Lipatnikov and Chomiak [41] describes other studies that found that thermodiffusive effects are important even for highly turbulent conditions.

Numerous DNS studies also have concluded that the theory of flame stretch correctly explains some of the general trends that were computed. Im and Chen [111] and Hawkes and Chen [96] computed local flamelet velocity  $S_{F,C}$  and stretch rate at many locations within their turbulent flame in a box.  $S_{F,C}$  was determined by integrating the volumetric reaction rate  $\omega_R$  across each flamelet using Eq. (3) and the flamelet Markstein number ( $Ma_F$ ) can be deduced from Eq. (36). They considered diffusionally stable, neutral and unstable mixtures, and they attempted to correlate other parameters (besides  $S_{F,C}$ ), including the displacement speed and the curvature and strain components of the stretch rate. They found that in all cases the general trends were in agreement with theory; i.e., stable and unstable mixtures yielded values of  $Ma_F$  that were positive and negative, respectively. However, in only a few cases did they achieve quantitative agreement between flamelet Markstein number  $Ma_F$  and the laminar value  $Ma_L$ .

DNS work of Bell et al. [112] also provides flamelet consumption speeds for hydrogen–air, methane–air and propane–air reactants. Several computed trends were in agreement with the theory (Eq. (36)). For example, Fig. 38 shows that local extinction occurred in regions of negative curvature (where cusps point toward the products) for a lean hydrogen–air mixture.  $S_{FC}$  was found to decrease/increase as the local curvature increased for stable/unstable mixtures, respectively. It can be concluded from DNS studies [111–117] that  $Ma_F$  and  $Ma_L$  have the same sign and that they change from positive to negative values at approximately the same values of  $\phi$ .

It is not yet possible to perform measurements of the flamelet Markstein number in turbulent flames because of difficulties in determining the instantaneous propagation speed and stretch rate of a three-dimensional interface. However, it has been possible to determine the Markstein number of a laminar flame in a flame–vortex experiment that mimics the turbulent wrinkling process. Fig. 39 shows a single toroidal vortex interacting with the laminar flame of Sinibaldi et al. [118]. Local displacement speeds and stretch rates could be measured as a function of time and distance along the layer because the interaction is axisymmetric, two-dimensional and repeatable. All of the necessary information is contained in the plane of the laser sheet. To determine the local propagation speed it was necessary to measure the difference between the local velocity of the flame in the lab coordinates and the local velocity of the reactants in the lab coordinates at each location on the interface. These two velocities were determined from shadowgraph movies and PIV. The time history of the interaction could be obtained because the

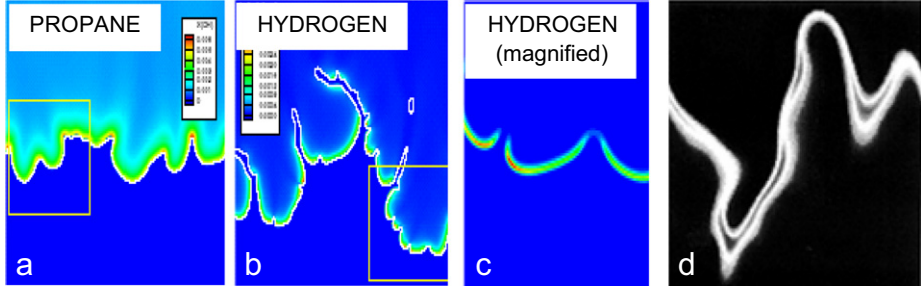


Fig. 38. DNS of turbulent flames by Bell et al. [95,112] showing that the diffusionaly stable lean propane–air case (a) has large wrinkles and no extinction, while the unstable lean hydrogen–air case (b) has small wrinkles and extinction occurs in the negatively curved cusps. In (d) the flamelets becomes thicker in positive curvature regions (at bottom of image) and thinner in negative curvature regions (at top of image). All of these observations are in agreement with the theory of flame stretch.

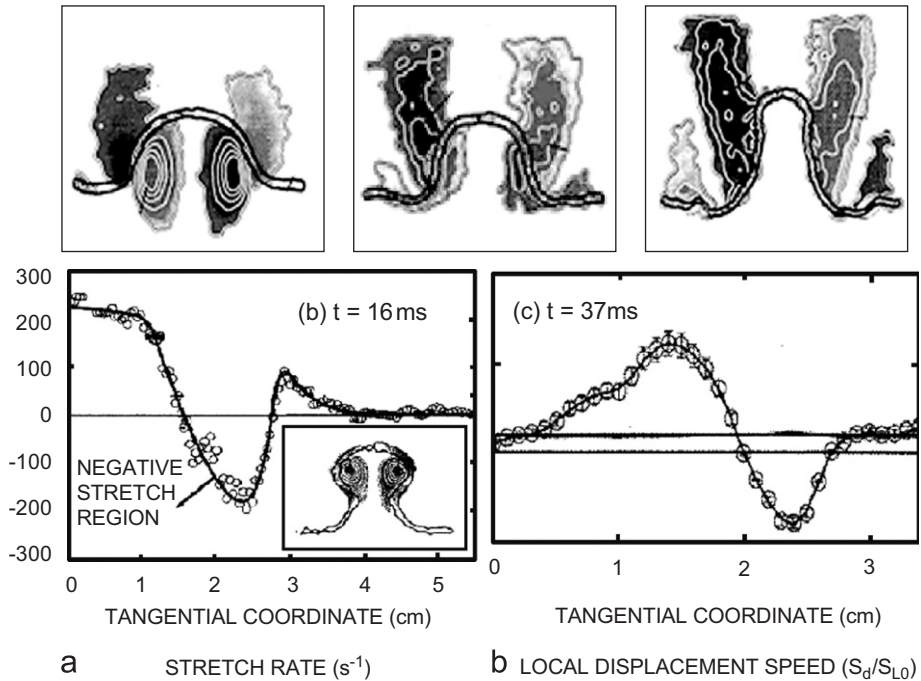


Fig. 39. Assessment of the theory of flame stretch by the flame–vortex experiments of Sinibaldi et al. [118] and Mueller et al. [77]. Upper images: vorticity contours as vortex moves upward through flame: (a) local stretch rate is maximum on centerline, decreases then increases in the tangential direction and (b) for rich methane, the local flame speed displays the opposite trend, which is in agreement with the theory. However, the measured magnitude of Markstein number is considerably larger than for steady counterflow flames.

experiment is repeatable; for each run a different time during the interaction was selected for the measurements.

Fig. 39 indicates that stretch rates cause large changes in the displacement speed in the flame–vortex experiment. The displacement speed is plotted in Fig. 39b and the stretch rate is plotted in Fig. 39a versus the tangential distance along the interface. Displacement speed is seen to increase to six times its unstretched value at a location where the stretch rate reaches its largest negative value. The general trends that were measured are consistent with the theory [49]. That is, the stretch rate in Fig. 39a first decreases and then it increases toward the right (away from the centerline). Fig. 39b shows that the local displacement speed displays an opposite trend; it increases and then it

decreases toward the right. In this case the reactants are a fuel-rich mixture of methane and air and they have a positive Markstein number. Eq. (35) predicts that the stretch rate and flame speed should display opposite trends and this is observed. A lean methane–air case also was considered in Ref. [118] and the measured trends are opposite to that of the rich case. While these general findings agree with the theory, it was noted that for all conditions the magnitude of Markstein number of the flame–vortex interaction was considerably larger than of a steady counterflow flame. The flame–vortex interaction is unsteady and consists of regions where the strain rate and curvature are positive and negative. The counterflow case is steady and has zero curvature and only positive strain.

More research is needed in order to determine if two Markstein numbers are required—one associated with the strain rate and one associated with the curvature [51].

#### 4.4. What turbulent burning velocity measurements to use for model assessment?

There are two ways that have commonly been used to assess the values of turbulent burning velocity predicted by a model. One method is to compare the predictions to the correlation curve of Bradley [42]. This correlation represents an “average over many geometries”, since measurements from Bunsen, spherical and V-flame geometries are plotted on the same graph. A second method is to compare predictions obtained for one specific burner geometry to an experiment that has an identical geometry and has identical boundary conditions. The latter method is preferable because it has been found that when correlation curves are generated, the scatter is so large that the resulting average value of  $S_T$  may not accurately represent any one experiment.

Fig. 40a displays the correlation that was reported by Bradley [42]; for each curve the product of Karlovitz

number and Lewis number is constant. Fig. 40b represents a replot of the curves in Fig. 40a, but the Lewis number is held constant for each curve. To plot Fig. 40b, first an acceptable curve fit to Fig. 40a was generated by setting  $S_T/S_{L0}$  equal to  $1 + 0.15(Ka Le)^{-1}(u'/S_{L0})^2$ . Bradley defines his Karlovitz number to be  $0.157(u'/S_{L0})^2(u'/\ell/v)^{-0.5}$ , and combining these last two relations yields the curves plotted in Fig. 40b, which are

$$\frac{S_T}{S_{L0}} = 1 + 0.95Le^{-1}\left(\frac{u'}{S_{L0}}\frac{\ell}{\delta_{L0}}\right)^{1/2}. \quad (39)$$

Eq. (39) is a correlation that averages over measurements of both consumption speeds and displacement speeds that were obtained in Bunsen, spherical and V-flame geometries.

Rather than rely on correlation curves such as Eq. (39), new methodologies are needed to make meaningful comparisons of DNS and LES predictions [1–4] to the large amount of data that have been made available by new laser diagnostics. A more complete database of measurement is required to achieve improved assessment of models.

- (a) There is a need to carefully record the spatial variations of burning velocity ( $S_T$ ) along the flame brush, and the spatial variations in  $u'$  and integral scale  $\ell$  at many locations upstream of the brush for Bunsen, low-swirl, counterflow and V-flames. For spherical flames, it is necessary to record  $S_T$ ,  $u'$  and  $\ell$  as a function of time.
- (b) Flame surface density and brush thickness need to be determined at all locations.
- (c) Boundary conditions should be measured, including profiles of  $U$ ,  $V$ ,  $W$ ,  $u'$ ,  $v'$ ,  $w'$ ,  $\ell_x$ ,  $\ell_y$ ,  $\ell_z$  to account for any non-uniformities on the boundary.

To date only a small number of experiments come close to meeting these goals. Table 6 lists a number of such studies but there are others which have not been included. Bunsen burners were operated by Cheng and Shepherd [119,120], Chen and Bilger [66], Gulder et al. [121], Filatyev et al. [53], Kobayashi et al. [122] and others [123–131].

Flat flames were stabilized in low-swirl burners by Cheng, Shepherd and coworkers [13,132] stagnation point geometries [12,133] or in the diffuser burner of Lawn and Schefer [14]. Measurements in V-flames were provided by Cheng and Ng [134], Goix et al. [94], Shepherd [82], Smith and Gouldin [16] and Namazian et al. [135], while spherical flames were studied in Refs. [16], [17] and [136].

Figs. 18, 25, 41–46 are plots of some of the burning velocities that were measured in the studies listed in Table 6. Laser diagnostics provided images of the  $\bar{c} = 0.5$  contour and values of the integral scale and turbulence intensities. Fig. 41 is a plot of global consumption speeds  $S_{T,GC}$  determined by Filatyev et al. [53] and other researchers [119,126–130]. For all cases shown in Fig. 41 a Bunsen flame was operated with nearly stoichiometric methane-air reactants. It is seen that for moderate turbulence intensities

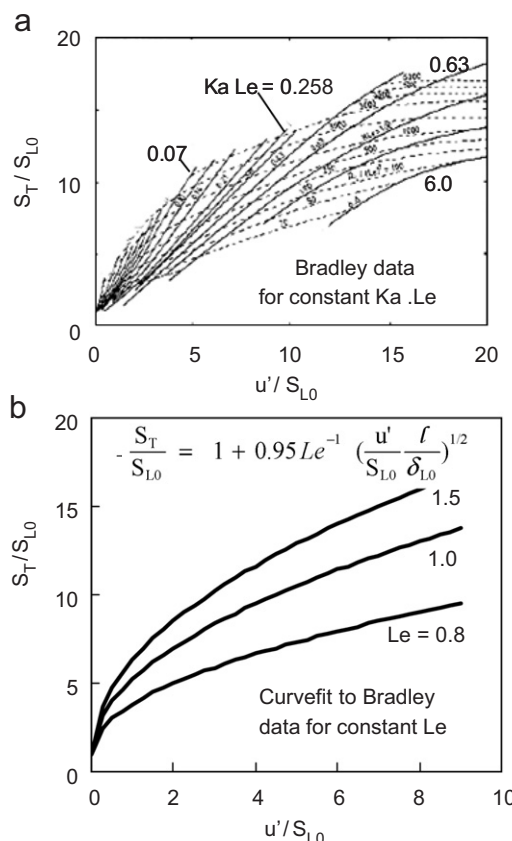


Fig. 40. (a) Bradley's correlation of turbulent burning velocity data [42]. For each curve in (a) the product of Karlovitz number and Lewis number was held constant. (b) A set of curves that are fit to Bradley's data and are given by Eq. (39). Note that (b) is plotted in a different way than (a) for each curve in (b)  $Le = \text{constant}$ .

Table 6

Some experimental studies that provide detailed measurements of turbulent burning velocities, integral scales, and boundary conditions that are useful for the assessment of models

Authors	Type	Fuel
Cheng and Shepherd [119]	Bunsen	C <sub>2</sub> H <sub>4</sub>
Cheng and Shepherd [120]	Bunsen	CH <sub>4</sub> , C <sub>2</sub> H <sub>4</sub>
Gulder et al. [121]	Bunsen	C <sub>3</sub> H <sub>8</sub>
Chen and Bilger [66]	Bunsen	CH <sub>4</sub> , C <sub>3</sub> H <sub>8</sub>
Filatyev et al. [53]	Bunsen	CH <sub>4</sub>
Lee et al. [122]	Bunsen	CH <sub>4</sub> , C <sub>2</sub> H <sub>4</sub>
Wu et al. [110]	Bunsen	H <sub>2</sub>
Shepherd and Cheng [13]	Flat low-swirl	CH <sub>4</sub>
Bedat et al. [131]	Flat low-swirl	CH <sub>4</sub>
Cheng [132]	Flat low-swirl	CH <sub>4</sub> , C <sub>2</sub> H <sub>4</sub>
Cho et al. [133]	Flat counterflow	CH <sub>4</sub>
Lawn and Schefer [14]	Flat diffuser	CH <sub>4</sub>
Cheng and Ng [134]	V-flame	C <sub>2</sub> H <sub>4</sub>
Smith and Gouldin [16]	V-flame	CH <sub>4</sub> , C <sub>3</sub> H <sub>8</sub>
Bradley et al. [136]	Spherical	CH <sub>4</sub> , C <sub>3</sub> H <sub>8</sub>
Kido et al. [17]	Spherical	H <sub>2</sub> , CH <sub>4</sub>
Lawes et al. [16]	Spherical	CH <sub>4</sub> , C <sub>8</sub> H <sub>18</sub>

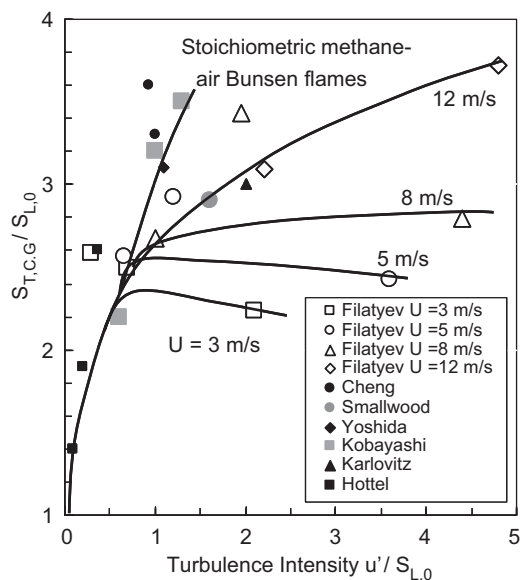


Fig. 41. Measured turbulent burning velocity of Filatyev et al. [53] compared to six other studies of Bunsen flames [119,126–130]. For all cases: stoichiometric methane-air. For each solid curve the mean velocity  $U$  was held constant, leading to a “bending” of the curves.

( $u'/S_{L,0}$ ) below 1.5, the burning velocity values are similar despite the fact that the integral scales differed somewhat. It also is seen that when the turbulence intensity exceeds 1.5 the curves in Fig. 41 are no longer linear but display some “bending” [53]. A similar bending was seen in the experimental measurements of Bradley [42] which appear in Fig. 40, as well as in many other studies [17,24,30,34,42,43,122,127] some of which appear in Figs. 28, 29 and 31. There have been several explanations for the observed bending. Burning velocity is proportional to  $\Sigma_{\max}$

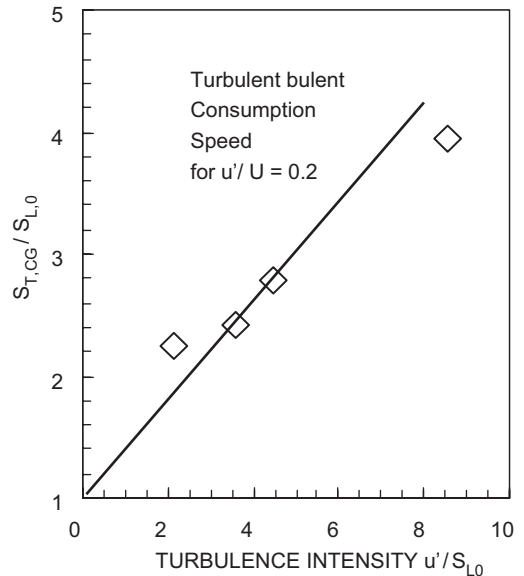


Fig. 42. Measured turbulent burning velocity  $S_{T,CG}$  of Fig. 41 replotted for a constant value of  $u'/U = 0.2$ , so that  $u'$  and  $U$  are not independently varied. If  $u'$  and  $U$  are not independently varied, as has been done in the past, the plot incorrectly hides the true nonlinear bending behavior.

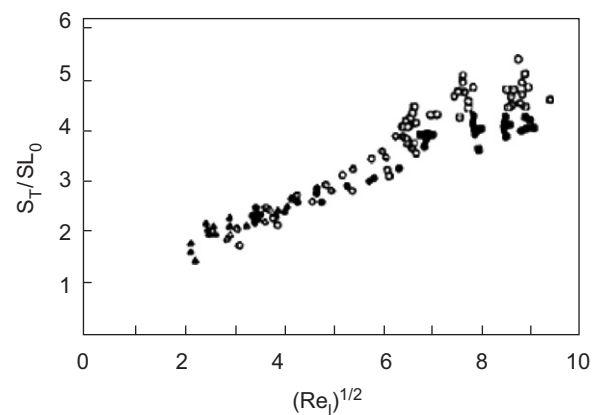


Fig. 43. Turbulent burning velocities measured in the V-flame of Smith and Gouldin [16].

$\delta_T$  and it is expected that as  $u'$  is increased the surface density and the brush thickness cannot grow indefinitely. Flamelets eventually merge and extinguish due to strain. Duclos et al. [24] increased  $(u'/S_{L,0})$  above 5 and their computed merging rate ( $\bar{M}$  in Eq. (10)) was large enough to cause bending of the curves shown in Fig. 31. Gas expansion also creates divergent velocity fields that prevents the interface from becoming too densely wrinkled. Geometric factors also can lead to the bending phenomenon, as shown by the analysis in Ref. [53]. Bunsen flames, for example, are limited in their height because of the finite burner width and the fact that flames from each side of the burner merge in the center. Increasing  $u'$  will tend to make the interface more wrinkled, but it also tends to make the brush propagate faster, which makes the brush shorter.

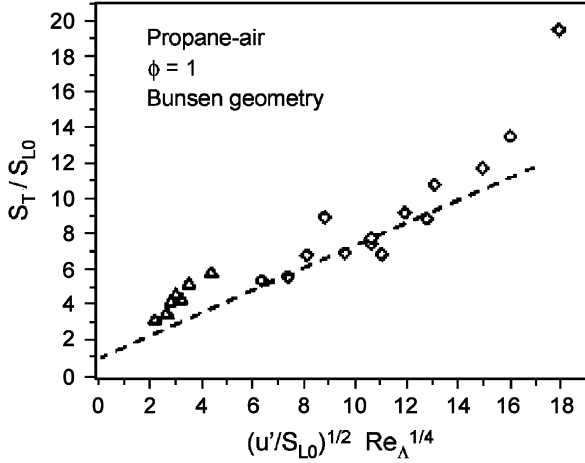


Fig. 44. Turbulent burning velocity  $S_{T,CG}$  of Bunsen flames of Gulder et al. [121]; propane-air,  $\phi = 0.9$ .

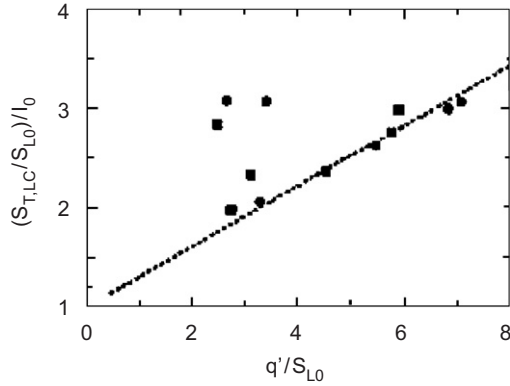


Fig. 45. Measurements of Chen and Bilger [66] of normalized turbulent burning velocity  $(S_{T,LC}/S_{L0})/I_0$  using Eq. (16). Profiles of surface density were integrated across the brush of a Bunsen flame. Fuels were methane and propane,  $\phi = 0.65\text{--}1.0$ .

The shorter flame brush has less distance over which the wrinkling process occurs. These two competing effects also may lead to the bending of the curves in Fig. 41.

Fig. 42 is presented to show that the bending phenomenon is observed when the proper precautions are taken to vary  $u'$  and  $U$  independently, but the bending is not observed if the ratio  $u'/U$  is forced to be constant. Data points in Fig. 41 were replotted for a fixed value of  $(u'/U)$  equal to 0.2. The linear curve in Fig. 42 is misleading; it represents results that would be obtained if a single grid is employed and only the mass flow rate was varied, which often has been done in the past. In such studies both the turbulence level and the residence time of eddies in the flame brush incorrectly were varied simultaneously. As  $u'$  increases the eddies become stronger, but if  $U$  is also increased, the eddy-flame residence time is reduced, and these two competing processes can counteract each other. This can mask the “bending” process, and may explain why it has not always been observed.

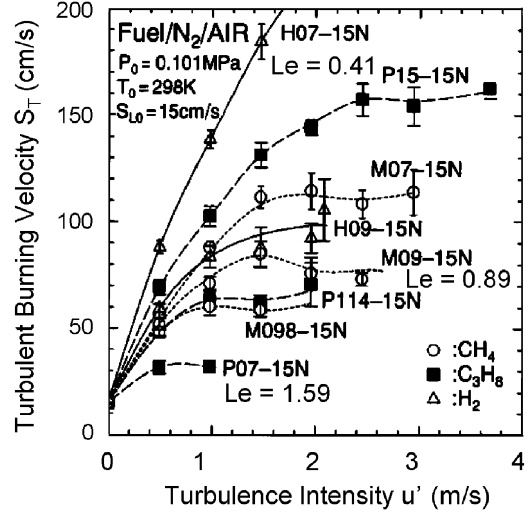


Fig. 46. Measured turbulent burning velocities for the spherical expanding flames of Kido et al. [17]. Circles = methane, squares = propane, triangles = hydrogen.  $S_{L0} = 15 \text{ cm/s}$  for all cases. The lowest curve has the largest  $Le = 1.59$ , while the highest curve has the lowest  $Le = 0.41$ .  $S_{T,L0}$  equals  $(\rho_p/\rho_R) dR/dt$ , where  $R$  is the flame radius.

Filatyev et al. [53] fit their measured turbulent burning velocities with the relation:

$$\frac{S_{T,C,G}}{S_{L0}} = 1 + 0.0021 \left[ \left( \frac{u'}{S_{L0}} \right) - 0.16 \left( \frac{u'}{S_{L0}} \right)^2 \right]^{1/2} \times \left[ \frac{U}{S_{L0}} \right] \left[ \frac{\ell}{\delta_{L0}} \right]^{1/2} \left[ \frac{W}{\delta_{L0}} \right]^{1/2} f(Ma). \quad (40)$$

This is a complicated formula because it provides a fit the nonlinear “bending” when the turbulence intensities are large. If we only consider smaller values of  $u'/S_{L0}$ , it is seen that the  $(u'/S_{L0})^2$  term can be neglected and Eq. (40) reduces to

$$\frac{S_{T,C,G}}{S_{L0}} = 1 + A_2 \left( \frac{u'}{S_{L0}} \frac{\ell}{\delta_{L0}} \right)^{1/2}. \quad (41)$$

This is similar to Bradley’s relation (Eq. (39)) except that  $A_2$  is not a constant but is

$$A_2 = 0.00077 \left[ \frac{\bar{U}}{S_{L0}} \right] \left[ \frac{W}{\delta_{L0}} \right]^{1/2} f(Ma). \quad (42)$$

The function  $f(Ma)$  was not measured in Ref. [53] because Markstein number was not varied. Analysis was provided in Ref. [53] that explains the nonlinear ‘bending’ of their burning velocity curves, and the analysis indicates the reason why the new parameters  $\bar{U}$  and  $W$  are important. The analysis also shows that Eq. (40) can be estimated by solving the flame surface density equation, providing that a number of simplifying assumptions are made. The reason why Bunsen flames depend on the mean velocity ( $\bar{U}$ ) and the burner width ( $W$ ) is because these quantities affect the wrinkling process. If  $W$  or  $\bar{U}$  is increased, the flame becomes taller. The flame therefore

Table 7  
Maximum turbulent burning velocities reported

Category	Reference	$u'/S_{L0}$	Maximum consumption speed $S_{T,GC}/S_{L0}$ or $S_{T,LC}/S_{L0}$	Maximum displacement speed $S_{T,LD}/S_{L0}$
Bunsen	Filatyev et al. [53]	8.0	4.0	—
Low swirl	Shepherd and Cheng [13]	7.5	4.7	14.8
Low swirl	Bedat and Cheng [123]	11.5	—	24.5
Spherical	Bradley [42]	20.0	—	18.0

becomes more wrinkled, since the degree of wrinkling increases with the distance from the attachment point.

Burning velocities of the V-flame of Smith and Gouldin [16] appear in Fig. 43 while the Bunsen data of Gulder et al. [121] appear in Fig. 44. Fig. 45 displays values of  $S_{T,LC}/I_0$  measured in a Bunsen burner by Chen and Bilger [66] by integrating profiles of flame surface density across the brush. Spherical flames were studied by Kido et al. [17] and typical measurements are shown in Fig. 46; other spherical flames were studied by Bradley et al. [136]. With spherical flames analysis indicates that the displacement speed  $S_{T,LD}$  equals  $(\rho_p/\rho_R) dR/dt$  where  $R$  is the measured radius of the  $\bar{c} = 0.5$  contour.

There has been considerable debate about the largest turbulent burning velocities that can be achieved. Bradley addressed this issue in his 1996 paper [42] that was entitled: How Fast Can We Burn? Within internal-combustion engines or afterburners it is possible to achieve very large values of  $S_T$  if the laminar burning velocity is increased by a factor of ten or more by preheating the reactants. Preheating often is caused by piston that adiabatically compresses the reactants, or by a recirculation zone that mixes hot products with the reactants. During a deflagration-to-detonation transition very large values of  $S_{L0}$  are caused by compressive heating. However, a related question is what is the largest value of the normalized consumption speed ( $S_{T,LC}/S_{L0}$ ) that is associated with the largest possible degree of flamelet wrinkling? Table 7 lists some of the largest values of the normalized consumption speed that were recorded in laboratory-scale burners. The largest normalized consumption speed of 4.7 was recorded in the low-swirl burner of Shepherd and Cheng [13], while Filatyev et al. [53] report a value of 4.0 and Chen and Bilger [66] measured values up to 3.0.

The flat flame of Shepherd and Cheng was not stabilized behind a rim or a rod, so it was free to oscillate violently and this might have created a larger flamelet surface area than in other burners that impose confining boundary conditions. It is noted that in most practical devices such as automobile engines or afterburners the brush normally would be confined to conform to a spherical or V-shape and would not be flat.

Table 7 also indicates that the normalized displacement speed can be as large as 24 and can be much larger than the normalized consumption speed. This difference is due, in part, to the divergence of streamlines within the brush and

the definition of the flame area, which was discussed in Section 1. Bradley [42] correlated values of  $S_T/S_{L0}$  that were as large as 17, but these values are displacement speeds; none of the values in Ref. [42] were determined by integrating the flame surface density across the brush. It can be concluded that intense wrinkling has been shown to cause the flamelet area (and consumption speed) to be approximately as large as five times the laminar value. It is expected that there exists an upper limit to the area ratio  $A_T/A_L$  that is imposed by layer merging, extinction and by gas expansion effects, but the value of this upper limit is not known.

## 5. Some research issues

Sections 1–4 indicate that recent advances in DNS, LES and laser diagnostics have created many new opportunities to make progress in our understanding of premixed turbulent combustion. It is now suggested that some research issues that need to be addressed are the following.

1. There is a need to separate premixed turbulent flames into different categories and to develop (for each category) a modern database that includes the turbulent burning velocity, flame surface density and brush thickness. The reader is referred to discussions on this topic in the proceedings of the Workshop on Premixed Turbulent Combustion that has been organized by R.K. Cheng and F.C. Gouldin [137]. The following fundamental geometries have been identified:

- (a) envelope flames (in a 2-D slot and axisymmetric Bunsen burners),
- (b) oblique flames (rod-stabilized),
- (c) unattached flat flames (in low swirl, diffuser or counterflow burners),
- (d) spherical flames (in a fan-stirred chamber).

For each category the wrinkling process and boundary conditions are different, so it is expected that for each category there will be a different relation for the turbulent burning velocity. Unfortunately, many of the previous measurements of burning velocity need to be excluded from a modern database because they have employed ambiguous definitions of burning velocity, integral scales were not always recorded, and lasers were not available to image the contours of mean reactedness. More detailed

Table 8

Quantities that are suggested to be included in a database of premixed turbulent combustion properties

	Criteria to assess simulations	Diagnostics now available	Refs.
$\Sigma$	Surface density—large scale	Mie, Rayleigh, CH or OH PLIF	[53,66,80,81]
$\Sigma_{SG}$	Surface density—subgrid scale	Mie, Rayleigh, CH or OH PLIF	—
$\delta_T$	Brush thickness	Mie, Rayleigh, CH or OH PLIF	[66,13,81]
$\delta_{CH}$	Reaction zone thickness of flamelets	CH or $CH_2O$ PLIF	[53–56]
$\delta_{TH}$	Preheat zone thermal thickness of flamelets	Rayleigh scattering	[1–12]
$\lambda$	Wrinkle wavelength	CH PLIF or Rayleigh	[58–61]
$K$	Stretch rate—large scale	CH PLIF + PIV	[53,78]
$K_{SG}$	Stretch rate—subgrid scale	CH PLIF + PIV	—
$\Gamma$	Stretch efficiency factor	CH PLIF + PIV	[53]
$Q$	Local quenching rate	CH or $CH_2O$ PLIF	[53–56]

measurements of the boundary conditions are needed. If the same burner is operated in different laboratories, the experimental results can be compared to better quantify the uncertainty. This approach has been demonstrated previously by participants of the turbulent non-premixed flame (TNF) workshops that are described on the website of Barlow [138]. Table 8 lists some of the suggested quantities that should be included in the premixed combustion database.

Subgrid surface density is a quantity that appears in LES subgrid reaction rate models. It can be measured by applying a spatial filter of size  $\Delta$  to the measured images of the flamelets. The subgrid scale stretch rate can be determined by applying a spatial filter to simultaneous CH PLIF-PIV data such as that of Ref. [53].

## 2. Agree on definitions of the turbulent burning velocity.

The consumption speed and the displacement speed are both useful quantities that allow for comparisons of experiments to other experiments or to simulations. However, some agreed-upon definitions are needed to avoid ambiguities. When consumption speed is measured, it is important to state how 3-D values of surface density are deduced from the 2-D laser sheet measurements. Measurements of  $\Sigma$  also require that the wrinkled interface be represented by an infinitely thin contour using an accurate curvefitting algorithm. If the contour has a finite thickness, the measurement of  $\Sigma$  may depend on the interrogation box size which leads to experimental error. Ambiguities can arise when the displacement speed of the leading edge of the brush is measured so it would be useful for researchers to agree on the value of  $\bar{c}$  that defines the leading edge. It also would be useful to record how the turbulent burning velocity varies in space along the brush of Bunsen and V-flames, and how it varies in time for spherical flames. This information is needed to make meaningful comparisons with simulations.

## 3. Understand the roles of the integral scale ( $\ell$ ), mean velocity ( $U$ ) and burner width ( $W$ ) in the relation for burning velocity.

Even after many years of research, there is little experimental evidence available that conclusively shows how the integral scale affects the turbulent burning

velocity. Adbel-Gayed et al. [43] attempted to correlate measured values of  $S_T$  using the parameter  $(u'\ell/v)^{1/2}$ , but the scatter in the data makes it impossible to draw a convincing conclusion. Lipatnikov and Chomiak [37] review some data plots which also indicate that burning velocity increases as the integral scale is increased.

One problem is that the integral scale normally can not be varied in an experiment while maintaining constant values of all other quantities such as turbulence level. For example, if a turbulence-producing grid is modified, usually both the integral scale and  $u'$  will vary. Another issue is that integral scale varies in space; some studies report their integral scale values at the burner exit, which may be far from the actual flame brush. In other studies there was no attempt to include the integral scale [6] when correlating burning velocity data.

Several theories and models predict that  $S_T$  should be proportional to  $(\ell)^{1/2}$ . For example, it is argued in Refs. [6,9] that since laminar flame speed is proportional to the square-root of the molecular diffusivity  $D$ , it can be assumed that in the thick flame regime the molecular diffusivity can be replaced by the turbulent diffusivity  $D_T$  which is proportional to  $u'\ell$ . Using a different approach, Peters [30] developed a  $G$ -equation model for conditions in the flamelet regime and he varied the integral scale. Fig. 30 shows that his predicted values of  $S_T$  approximately scale as  $(\ell)^{1/2}$ . The CFM [26] also predicts that  $S_T$  depends on the integral scale because source terms in the surface density balance (Eqs. (10), (13), (14)) are proportional to  $(u'/\ell)$ .  $\Gamma_K$  and  $\Gamma_K$  also depends on  $\ell$ . The role of the integral scale has been explained by two entirely different physical arguments. In the thick flame regime it is assumed that eddies enter the preheat zone and increase the diffusion of enthalpy inside the flamelets [6], whereas in the flamelet regime the integral scale primarily controls the degree of wrinkling and flamelet surface area [19,30]. Perhaps the best way to understand the role of the integral scale is to use DNS to systematically vary the integral scale while keeping all other parameters constant. Two other parameters that are of interest for the case of Bunsen flames are the mean velocity  $U$  and the burner width  $W$ . Ref. [53] indicates that burning velocity depends on these

parameters because they control the residence time of the flame–vortex interactions and the overall height of the flame, which affects the degree of wrinkling.

#### 4. Understand the role of Markstein number in the relation for burning velocity.

It sometimes has been assumed that the turbulent Markstein number ( $Ma_T$ ) that appears in Eq. (37) (which is used to determine the stretch factor  $I_0$ ) is equal to the laminar Markstein number ( $Ma_L$ ) that is defined by Eq. (35). This assumption is disputed by the DNS results of Im and Chen [111] and Hawkes and Chen [96]. However, their results do show that for the special case when  $Ma_L$  is zero (i.e., for a diffusionally neutral fuel–air ratio) their computed flamelet Markstein number  $Ma_F$  is approximately zero, and this suggests that  $Ma_T$  also is zero. There is a need for future DNS and experimental efforts to determine values of  $Ma_T$ . To do so, it would be necessary to perform DNS simulations or experiments for a range of values of  $u'$  using a Bunsen burner geometry, for example. Values of  $I_0$  can be determined by combining Eq. (29) with values of  $\Sigma$  and the known mass flow rate of reactants. Once  $I_0$  is known, Eq. (37) provides the turbulent Markstein number  $Ma_T$ .

#### 5. Develop high-resolution cinema-PIV and cinema-PLIF methods to take movies of the turbulent eddy–flamelet interactions and compare them to DNS.

Since the flame–eddy interaction is fundamental to the stretching and wrinkling of turbulent flames, there is a need to visualize the time–history of the interactions. As described in Section 2.2, Steinberg et al. [73] recorded cinema–stereo PIV movies of flame–eddy interactions for fully turbulent conditions; in some cases the classical wrinkling process that was predicted by Damkohler [6] was observed. In other cases eddy–eddy interactions negate any attempts to wrinkle the flame, while sometimes the wrinkling process is clearly affected by flame generated vorticity. While it is possible to use DNS, LES and  $G$ -equation simulations to generate movies of flame–eddy interactions, there has been little information reported to date.

Another research need is to achieve improved spatial resolution of Rayleigh scattering and PLIF diagnostics and then accurately measure the thickness of flamelets over a wide range of Karlovitz numbers. The current controversy concerning the boundary between the laminar flamelet regime and the thick flame regime is due, in part, to difficulties in achieving the necessary spatial resolution of 50–100  $\mu\text{m}$ . New micro-PIV, micro-Rayleigh scattering and micro-PLIF diagnostics are needed, but these diagnostics require extremely thin laser sheets and improved signal-to-noise. A related challenge is to image eddies that are of the same size as the flame thickness in order to determine if they enter the preheat and reaction zones.

#### 6. Assess DNS simulations—boundary conditions, resolution requirements

Even though DNS provides solutions to the exact form of the conservation equations, problems can arise when the

results are compared to measurements. Realistic boundary conditions must be known on all boundaries. It is not known if the incoming turbulence field of an experiment can be characterized by just a few measured parameters such as the profiles of mean velocity  $U$ , velocity fluctuations ( $u'$ ) and integral scale ( $\ell$ ). It may be acceptable for the DNS boundary conditions to be based on the assumption that the incoming turbulence is isotropic and has a corresponding power spectrum. If these assumptions are not adequate, then it is necessary to measure all three integral scales, profiles of the fluctuations of all three velocity components and a measured power spectrum at the inlet. Grid resolution continues to be another important issue. In recent DNS work a grid resolution of 20–79  $\mu\text{m}$  has been achieved [1,3,75,95] but reaction layer thickness may be as small as 200  $\mu\text{m}$ . Another complication can arise if local flame extinction occurs; it may not be adequate to use the current complex chemistry mechanisms that contain typically 20 species and 84 reactions. To achieve better agreement with measurements, additional attention may be required to simulate, pressure fluctuations, radiative heat losses and buoyancy forces.

#### 7. Improve methods to measure 3-D flame surface area from 2-D images.

Several experimental errors can arise when measurements of flame surface density are performed. Wrinkled flamelets are measured to have a finite thickness that may be larger than the true value, due to the pixel size of the camera or due to the spatial averaging (the binning of pixels) that is needed to achieve an acceptable signal-to-noise ratio. To determine  $\Sigma$ , it is necessary to represent the interface by an infinitely thin contour, using an appropriate curve fitting algorithm, so that the measured values of  $\Sigma$  can be shown to be independent of the interrogation box size in the limit as interrogation box size is decreased. Another issue is that some approximation is necessary to estimate the 3-D surface area from 2-D images. Three approximations that have been employed are (i) the 2-D surface density assumption, (ii) the flame perimeter assumption and (iii) the fractal dimension assumption. When the surface density assumption is employed,  $\Sigma$  is assumed to equal the average flame perimeter within an interrogation box located in the plane of the laser sheet, divided by the interrogation box area. DNS results of the DNS of Bell et al. [1] that appear in Fig. 15 showed that this 2-D value should be multiplied by 1.35 to achieve the correct value of  $\Sigma$ . The second method to estimate  $A_T/A_L$  is to assume that it equals  $(P_T/P_L)^2$ .  $P_T$  is the perimeter of the reaction layers that appear in a 2-D laser sheet image and  $P_L$  is the perimeter if there was no wrinkling, which is determined by superimposing many instantaneous images of the wrinkled flame surface to obtain the smooth time-averaged surface and determining its perimeter. To assess this method, first consider the hypothetical case for which all wrinkles are rectangular in shape. Each wrinkle has a height  $H$  and has a base that is a square having dimensions  $L$  by  $L$ . For this example  $A_T$  can be shown to be related to

$P_T$  by

$$(A_T/A_L)/(P_T/P_L)^2 = (1 + 4H/L)/(1 + 2H/L)^2. \quad (43)$$

This function is plotted as the thick solid line in Fig. 47. Now consider the wrinkles to be prisms that have triangular sides, a height  $H$  and a base that is a square having dimensions  $L$  by  $L$ . The area ratio  $(A_T/A_L)$  in this case is  $(1 + 4H^2/L^2)^{1/2}$ . The perimeter ratio is determined by considering all possible intersections of a laser sheet with the wrinkled interface. For this geometry the results are indicated by the dashed line in Fig. 47. It is expected that for realistic wrinkles the values of  $(A_T/A_L)/(P_T/P_L)^2$  can be approximated by the thin solid line that lies between the other two curves in Fig. 47. Since the ratio of height to length ( $H/L$ ) rarely exceeds unity, Fig. 47 shows that the flame perimeter method to estimate the 3-D surface area has a typical uncertainty of less than 20%. A third way to estimate the 3-D surface area is the fractal dimension assumption.  $A_T/A_L$  is assumed to be equal the ratio of the outer fractal scale to the inner fractal scale, raised to the power of  $D$ , where  $D$  is the 3-D fractal dimension [121,126].  $D$  is assumed to be the measured 2-D fractal dimension plus 1.0. This method has not been used often because results that are plotted in Ref. [121] do not appear to be realistic. Gulder et al. [121] point out that ambiguities still exist in the way that the fractal dimension is determined.

#### 8. Understand the role of hydrodynamic instabilities.

It has been noted that the wavelengths of the flamelet wrinkles often are larger than the integral scale of the turbulence, and they almost never are as small as the Taylor scale [58–61]. Instead, there is some evidence that the wrinkle wavelength is proportional to the cell size associated with hydrodynamic instabilities. However, there is little experimental information available to determine if the role of hydrodynamic instabilities is comparable to the role of turbulent eddies in the wrinkling process. Kobaya-

shi, et al. [15] showed that increasing the gas pressure to 10 atm causes a marked decrease in the wrinkle wavelength while they maintained a constant value of the integral scale. This work shows that the wrinkle wavelength does not scale with the integral scale but scales with the flame thickness, which is inversely proportional to the gas pressure. The theory of hydrodynamic instability predicts that cell sizes are proportional to the laminar flame thickness [45], so it is possible that the fine-grained wrinkling observed by Kobayashi at high pressures is caused, in part, by hydrodynamic instabilities. Paul and Bray [101] modeled the flame wrinkling caused by hydrodynamic instabilities by adding a term to the flame surface density equation.

#### 9. Determine the limits of the flamelet regime

The previous discussion has focused on measurements and models that are appropriate for the flamelet regime. In a very few cases there is evidence that premixed combustion occurs in distributed reaction zones and for these conditions flamelets do not exist. The boundaries between the regimes of flamelets, thick flames and distributed reactions have not been quantified experimentally. Distributed reaction zones are created by rapidly raising the temperature of a large region of the reactants to a value that is above the ignition temperature. After an ignition delay the reactions will begin at many locations simultaneously. If the reactants are above the ignition temperature, there is no need for a flame because a flame is a layer within which heat diffuses upstream in order to preheat the reactants to the ignition temperature. The criterion required for distributed reactions to occur is that over a large region in space the following relation must hold:

$$\tau_{\Delta T} < \tau_{ig}, \quad (44)$$

$\tau_{\Delta T}$  is the time required to raise the temperature of the reactants to a temperature above the ignition temperature and  $\tau_{ig}$  is the chemical ignition delay time. Two methods have been used in order to attempt to create this rapid temperature rise: (a) rapid adiabatic compression and (b) rapid turbulent mixing of hot products into the reactants. While it has been demonstrated that rapid adiabatic compression can create distributed reactions in homogeneous charge compression-ignition (HCCI) engines and in shock tubes [139–141], there appears to be no conclusive proof that the second method (rapid turbulent mixing) can create a documented distributed reaction zone. A documented distributed reaction zone is defined to be a set of measured images of the heat release region or images of radicals such as CH that are spread out over distances that are many times larger than the thickness of a laminar flame. The reaction zone is defined to be the primary reaction zone that is associated with heat release and fuel decomposition, and the reaction zone does not include post-flame  $\text{NO}_x$  and  $\text{OH}/\text{water}$  dissociation reactions which often are distributed in space but are not part of the flame. It is not argued that distributed reaction zones created by rapid turbulent mixing are not possible to

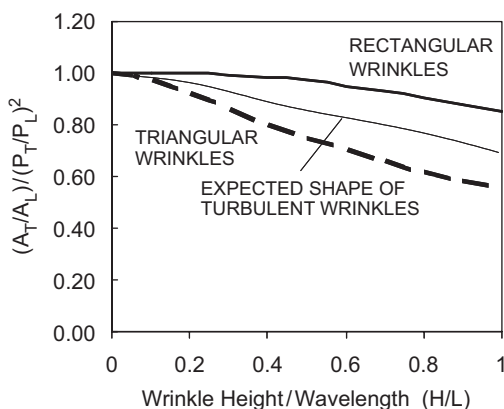


Fig. 47. Ratio of the square of the 2-D flame perimeter ratio to the 3-D area ratio for different wrinkle heights  $H$  and wavelengths  $L$ . A value of unity on the  $y$ -axis implies that measured  $(P_T/P_L)^2$  is a good estimate of the 3-D area ratio. Dashed line: wrinkles are rectangular with height  $H$  and base  $L$  by  $L$ ; solid line: wrinkles are tetrahedral prisms. Conditions for realistic wrinkles are expected lie between the two curves.

achieve; to this author's knowledge they have not yet been documented.

When rapid compression is used to heat the reactants, there is experimental proof that distributed reactions occur in a HCCI device [139,140] or in a shock tube [141]. These few cases do not represent new regimes of turbulent combustion, since it is rapid compression and not turbulence that causes the distributed reactions. He et al. [139] employed a rapid-compression facility in which compressed gases drive a piston into the iso-octane-air reactants. The adiabatic compression rapidly raised the reactants to a temperature that exceeds the ignition temperature. Chemiluminescence that was recorded with a high-speed camera was observed to be uniformly distributed in space as the reaction progresses. There was no visible evidence of flamelets. Aleiferis et al. [140] obtained images in an HCCI engine showing that under some conditions there were many islands where reactions simultaneously occurred. It is noted that spark-ignited internal combustion engines and gas turbine engines do not experience the rapid compression–ignition process that occurs in HCCI engines. Based on the limited images available, flame structure in spark-ignited and gas turbine engines appears to consist of thin reaction layers [142–145].

Some attempts to achieve distributed reaction zones due to rapid turbulent mixing have led to the development of “well-stirred” reactors [146–148], strong recirculation zones [149–150], the quasi-equilibrium distributed reactor [151], “flameless oxidation [152]” and moderate and intense low oxygen dilution (MILD) [153] devices. However, to date there is no experimental proof (i.e., there are no images of radicals) that demonstrate that distributed reactions exist in these devices. On the contrary, when a strong recirculation zone is used to increase the mixing rates, the images of Ratner et al. [74], Meier et al. [56] and Rasmussen et al. [76] indicate that flamelets still exist. These CH images indicate that very large turbulence intensities exert strain rates which keep the layers thin, so that the layers “extinguish before they broaden”.

An active area of research has been the determination of the boundary of the flamelet regime. Since the experimental evidence described in Section 2 disputes the prediction that boundary of the flamelet regime occurs when Karlovitz number exceeds unity (and the Kolmogorov scale equals the laminar flame thickness), it is reasonable to look for another criterion. In order to cause broadening, an eddy should have a rotational velocity large enough to create a turbulent diffusivity ( $D_T$ ) that exceeds the molecular diffusivity ( $D$ ), so that the transport of heat is enhanced by the turbulence. This suggests that the criterion should be

$$D_T \geq D. \quad (45)$$

The turbulent diffusivity of eddies that have diameters  $d$  equal to  $\delta_{L0}$  depends on the rotational velocity ( $u_{\theta,F}$ ) of these eddies, so  $D_T$  can be set equal to  $u_{\theta,F} \delta_{L0}$ . The rotational velocity  $u_{\theta,F}$  of the eddy is estimated to equal  $u'(\delta_{L0}\ell)^{1/3} (\rho_P/\rho_R)$ . The factor  $u'(\delta_{L0}\ell)^{1/3}$  comes from the

energy cascade concept. The density ratio ( $\rho_P/\rho_R$ ) is suggested by flame–vortex experiments [77] which show that as an eddy passes through a flame, its volume after gas expansion is  $(\rho_R/\rho_P)$  times its volume before gas expansion. The circulation associated with the eddy is conserved, so the eddy rotational velocity decreases during passage. The gas expansion elongates the fluid element only in one direction (normal to the flame); it follows that the rotational velocity is estimated to be  $(\rho_P/\rho_R)$  times its original rotational velocity. Combining these relations leads to

$$D = u'(\delta_{L0}/\ell)^{1/3}(\rho_R/\rho_P)^{-1}\delta_{L0}. \quad (46)$$

Solving this equation for  $u'$  and inserting it into Eq. (45) yields a new criterion for flamelet broadening:

$$Ka > (\rho_R/\rho_P)^{3/2}, \quad (47)$$

$Da$  has been eliminated by setting it equal to  $D/S_{L0}$ . The right side of Eq. (47) is typically 17. Therefore, high intensity turbulence would be required to broaden a flamelet. However broadening may never occur at all if the “flamelets tend to extinguish before they are broadened”. Evidence that extinction occurs before any broadening is provided by Ratner et al. [74] who achieved very high intensity turbulence within a strong recirculation zone. Their images were shown in Fig. 11. The CH layers are seen to remain thin but become “shredded” due to frequent local extinction. Their conditions were partially premixed in the combustion zone and were initially non-premixed. For the premixed case no imaging studies of shredded reaction layers have been conducted.

#### 10. Determine the role of large eddies versus small eddies

In the past it has been argued that small eddies control the dissipation rates and the stretch rates and therefore play a dominant role in turbulent combustion. The argument is that small eddies have a larger ratio of rotational velocity to eddy diameter ( $u_\theta/d$ ) than do large eddies because energy cascade concepts [9] predict that  $u_\theta$  scales as  $u'(d/\ell)^{1/3}$  so  $(u_\theta/d)$  should scale as  $d^{-2/3}$ . In some studies it has been assumed that stretch rates are proportional to  $(u_\theta/d)$  but recent research casts doubt on this assumption. It is more difficult for a vortex to wrinkle and stretch a flame surface than to stretch a scalar isocontour within a non-reacting flow. DNS and flame vortex experiments show that combustion adds a new complication; heat release superimposes velocity vectors that diverge away from the reaction layer. In the product gases the additional velocity is 5–7 times the laminar burning velocity. Small eddies typically do not have a rotational speed large enough to compete against this new velocity field. In addition, the volume of each eddy expands by a factor of 5–7 as it crosses a reaction layer. Since the circulation tends to remain constant, this means that the mean vorticity decreases by a factor of 5–7, as was shown by the flame–vortex experiments of Mueller et al. [77]. In addition, the residence time during which a large eddy is in contact with the flamelet is expected to exceed the residence

time of a small eddy. The role of large eddies has important implications for modeling efforts. Small eddies are assumed to act in a universal way that can be modeled in RANS equations by terms that have been averaged in time. Large eddies often introduce unsteady motions (such as vortex shedding) that are not universal but depend on the geometry of shear layers. The occurrence of large-scale unsteadiness may require the use of LES or DNS.

The stretch efficiency factor  $\Gamma_K$  defined by Eq. (13) is a useful way to quantify the role of eddy size. Meneveau and Poinsot [19] used DNS to determine that  $\Gamma_K$  is approximately equal to  $C_1(\ell/\delta_{L0})^{1.0}$  where  $C_1$  is a constant. They found that  $\Gamma_K$  did not significantly depend on  $u'/S_{L0}$ . Measurements of stretch rates and  $\Gamma_K$  were made in the turbulent premixed Bunsen flame of Filatyev et al. [53] and they obtained a somewhat different result:

$$\Gamma_K = C_2 \left( \frac{\ell}{\delta_{L0}} \right)^{2.0} . \quad (48)$$

The quantity  $C_2$  is proportional to  $(\bar{U}/S_{L0})^2$ . It is not surprising that the turbulent Bunsen flame results differ from the DNS result obtained for a flat flame interacting with a toroidal vortex. In the Bunsen flame not all of the vortices are toroidal, and they do not pass over the flame in a direction that is normal to the flamefront.

There is additional evidence that suggests that small eddies are too weak to perturb a flame: it is observed that wrinkles in the flame surface are almost never as small as the Taylor scale. Table 9 is a list of the wavelengths of the smallest wrinkles measured in recent experiments. The values indicate that for eddies to wrinkle the flame, they must be at least as large as 20–50% of the integral scale and must be ten times larger than the Taylor scale. It follows that eddies at the Kolmogorov scale are far too weak to create wrinkles. Wrinkles are never observed to be as small as the Kolmogorov scale. Kolmogorov eddies are so weak that they are dissipated by viscosity after about one revolution, so they cannot perturb the flame, which acts a source that produces velocities in the products on the order of 240 cm/s.

There also is some evidence that large eddies are more effective than small eddies in causing local extinction.

Roberts et al. [154] propagated a laminar flame over a strong vortex and varied the vortex size and rotational velocity. They found that extinction occurred when the vortex Karlovitz number exceeded:

$$(u_\theta/S_{L0})/(d/\delta_{L0}) = 2.2 + 9.2(d/\delta_{L0})^{-2}. \quad (49)$$

Non-dimensional vortex diameters  $d/\delta_{L0}$  were varied from 1 to 5. Eq. (48) indicates that if the eddy size is made larger it is easier to cause local extinction since a smaller non-dimensional stretch rate is required. DNS results of Meneveau and Poinsot [19] displayed a similar trend. To understand the role of large and small eddies, it would be useful to apply spatial filters to DNS results and identify the degree of flamelet wrinkling, stretching and extinction associated with eddies of different size ranges.

A final example of how DNS can identify the role of turbulent eddies is given by Fig. 48. It is a schematic showing two counter-rotating eddies on the left that exert a positive stretch rate, while the two eddies on the right are rotating in the opposite direction. It is clear that the eddies on the left will increase the surface area of the flame because they induce the velocity field shown by the arrows that exerts a positive stretch rate. The eddies on the right would decrease the surface area if the flame remained flat because the arrows drawn indicate that they exert a negative stretch rate. However, they also induce a rotational velocity field that forces the flame to propagate downward between the eddies. This has the net effect of increasing the surface area. This process causes the correlation between stretch rate and flame curvature to be negative; the eddies on the left exert positive stretch and negative curvature, while the eddies on the right do the opposite. The DNS work of Chakraborty and Cant [89] quantified this negative correlation. The example shows that even turbulent eddies that initially exert a negative stretch rate may end up exerting a positive stretch rate at later times because the unsteady flame does not remain flat but becomes distorted. For these reasons the counterflow flame analogy may be valid only for unrealistically small perturbations and images of the actual eddy–flame interactions are needed.

Table 9

Wavelengths ( $\lambda_{\min}$ ) of the smallest wrinkles of premixed turbulent flames, which are 12–25 times the Taylor scale, indicating that eddies smaller than ten Taylor scales do not cause wrinkles

Reference	Wavelength of smallest wrinkle $\lambda_{\min}$ (mm)	Integral scale $\ell$ (mm)	$\lambda_{\min}/\ell$	$\lambda_{\min}/\lambda_{\text{Taylor}}$	$\lambda_{\min}/\delta_{L0}$
Filatyev et al. [53]	2	5.2	0.4	20	6.7
Cheng et al. [58]	2	10.4	0.2	24	4.0
Lachaux et al. [59]	4	3.0	1.3	25	3.1
Lachaux et al. [59]	2	3.1	0.6	12	3.1
Shepherd et al. [60]	1.5	3.0	0.5	13	5.0
Buschmann et al. [61]	2	12	0.2	22	5.0

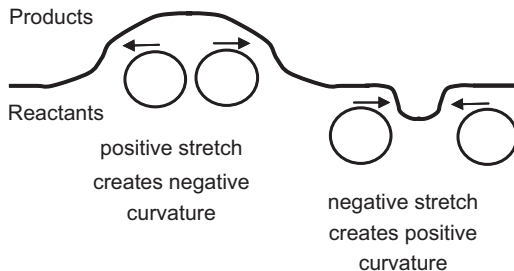


Fig. 48. Schematic of counter-rotating vortices on the left that exert positive stretch but create negative curvature. Vortices on the right initially exert negative stretch but create positive curvature. Even the vortices on the right eventually create more surface area because the flame does not remain flat but is free to wrinkle. DNS results of Chakraborty and Cant [89] have quantified this negative correlation.

## 6. Conclusions

DNS results of Bell et al. [1,2] have demonstrated that it is now possible to predict reasonable values of the turbulent burning velocity, using no modeling constants, of the Bunsen experiment of Filatyev et al. [53] and the V-flame of Cheng and Shepherd [2] for realistic Reynolds numbers. The 3-D DNS work employed complex chemistry and an adaptive mesh refinement. Differences between predictions and measurements were 4% and 19%, respectively. LES and RANS models also provide realistic curves of turbulent burning velocity as the turbulence intensity and integral scale are varied, but a few modeling constants are required. The universality of these constants needs to be assessed. We now have available many images of the reaction layers that are associated with fuel decomposition and with heat release. These images are made available by recent advances in CH and CH<sub>2</sub>O/OH PLIF diagnostics as well as DNS. Thin flamelets are found to occur even when the Karlovitz number greatly exceeds unity. The preheat zone average thickness is no larger than the laminar value in many studies, while in some cases it is 2–4 times larger. Better spatial resolution is needed to see if the thickening of the preheat zone is due to turbulence or is due to strain rates, the orientation of the reaction layer with the laser sheet, merging of segments near cusps, or resolution limitations. Significant thermodiffusive (Markstein number) effects occur even for high intensity turbulence; the theory of flame stretch now provides a qualitative but not yet a quantitative explanation. Research has identified improved ways to define and quantify the turbulent burning velocity and the flame surface density. A modern database that contains several suggested quantities is needed for each of several flame categories.

## Acknowledgments

The author is grateful for discussions with many colleagues, including: R.K. Cheng, I.G. Shepherd, N. Peters, J.B. Bell, J.F. Grcar, M.S. Day, J.H. Chen, H. Pitsch, C.K. Law, T. Poinsot, S. Candel, M.C. Drake, F.

Gouldin, C.D. Carter, S.A. Filatyev, A.M. Steinberg, J.M. Donbar, A. Ratner, W.L. Roberts, C.J. Mueller, A.F. Ibarreta, J.O. Sinibaldi, M.S. Wu and A. Gulati. Support has been provided by National Science Foundation Grants CTS-0203140, CTS-9904198, CTS-9123834 and CPE-8213319.

## References

- [1] Bell JB, Day MS, Grcar JF, Lijewski MJ, Driscoll JF, Filatyev SA. Numerical simulation of a laboratory-scale turbulent slot flame. *Proc Combust Inst* 2006;31:1299–307.
- [2] Bell JB, Day MS, Shepherd IG, Johnson MR, Cheng RK, Grcar JF, et al. Numerical simulation of a laboratory scale turbulent V-flame. *Proc Natl. Acad. Sci.* 2005;102(29):10006–11.
- [3] Sankaran R, Hawkes ER, Chen JH. Structure of a spatially-developing turbulent lean methane-air Bunsen flame. *Proc Combust Inst* 2006;31:1291–8.
- [4] Pitsch H, Duchamp de Lagenest L. Large-eddy simulation of premixed turbulent combustion using a level-set approach. *Proc Combust Inst* 2002;29:2001–8.
- [5] Bray KNC, Cant RS. Some applications of Kolmogorov turbulence research in the field of combustion. *Proc R Soc London A* 1991;434:217–27.
- [6] Damköhler G. Jahrb. deut. Luftfahrtforsch., Z. Electrochem. 1940;46(601):113; also see Lewis B, von Elbe G. Combustion, flames and explosions of gases. New York: Academic Press; 1961.
- [7] Bray KNC, Peters N. In: Libby PA, Williams FA, editors. Turbulent reacting flows. London: Academic Press; 1994. p. 63–114.
- [8] Peters N. Laminar flamelet concepts in turbulent combustion. *Proc Combust Inst* 1986;21:1231–50.
- [9] Peters N. Turbulent combustion. Cambridge: Cambridge University Press; 2000.
- [10] Poinsot T, Veynante D. Theoretical and numerical combustion. Philadelphia, PA: Edwards Pub; 2005.
- [11] Ashurst WT. Darrieus-Landau instability, growing cycloids and expanding flame acceleration. *Combust Theory Model* 1997;1(4): 405–28.
- [12] Wu AS, Bray KNC. A coherent flame model of premixed turbulent combustion in a counterflow geometry. *Combust Flame* 1997;109: 43–64.
- [13] Shepherd IG, Cheng RK. The burning rate of premixed flames in moderate and intense turbulence. *Combust Flame* 2001;127: 2066–75.
- [14] Lawn CJ, Schefer RW. Scaling of premixed turbulent flames in the corrugated regime. *Combust Flame* 2006;146:180–99.
- [15] Kobayashi H, Kawahata T, Seyama K, Fujimari T, Kim J-S. Relationship between the smallest scale of flame wrinkles and turbulence characteristics of high pressure, high temperature turbulent premixed flames. *Proc Combust Inst* 2002;29:1793–800.
- [16] Smith KO, Gouldin FC. Turbulence effects on flame speed and flame structure. *AIAA J* 1979;11,5:1243–50.
- [17] Kido H, Nakahara M, Nakashima K, Hashimoto J. Influence of local flame displacement velocity on turbulent burning velocity. *Proc Combust Inst* 2002;29:1855–61.
- [18] Veynante D, Duclos JM, Piana J. Experimental analysis of flamelet models for premixed turbulent combustion. *Proc Combust Inst* 1994;25:1249–56.
- [19] Meneveau C, Poinsot T. Stretching and quenching of flamelets in premixed turbulent combustion. *Combust Flame* 1991;86:311–32.
- [20] Baritaud TA, Duclos JM, Fusco A. Modeling turbulent combustion and pollutant formation in stratified charge SI engines. *Proc Comb Inst* 1996;26:2627–35.
- [21] Musculus MP, Rutland CJ. Coherent flamelet modeling of diesel engine combustion. *Combust Sci Technol* 1995;104:295–337.

- [22] Teraji A, Tsuda T, Noda T, Kubo M, Itoh T. Development of a novel flame propagation model (UCFM: universal coherent flamelet model) for SI engines and its application to knocking prediction. *Soc Automot Engr* 2005; paper 2005-0100199.
- [23] Boudier P, Henriot S, Poinsot T, Baritaud T. A model for turbulent flame ignition and propagation in spark ignition engines. *Proc Combust Inst* 1992;24:503–10.
- [24] Duclos JM, Veynante D, Poinsot T. A comparison of flamelet models for premixed turbulent combustion. *Combust Flame* 1993; 95:1–16.
- [25] Veynante D, Piana J, Duclos JM, Martel C. Experimental analysis of flame surface density models for premixed turbulent combustion. *Proc Combust Inst* 1996;26:413–20.
- [26] Prasad ROS, Paul RN, Sivathanu YR, Gore JP. An evaluation of combined flame surface density and mixture fraction models for nonisenthalpic premixed turbulent flames. *Combust Flame* 1999; 117:514–28.
- [27] Emery P, Maroteaux F, Sorine M. Modeling of combustion in gasoline direct injection engines. *ASME J Fluids Eng* 2003;125: 520–32.
- [28] Choi C, Huh K. Development of a coherent flamelet model for a spark ignited turbulent premixed flame in a closed vessel. *Combust Flame* 1998;114:336–48.
- [29] Brandl A, Pfitzner M, Mooney JD, Durst B, Kern W. Comparison of combustion models and assessment of the applicability to the simulation of premixed turbulent combustion in IC engines. *Flow Turb Combust* 2005;75:335–50.
- [30] Peters N. The turbulent burning velocity for large-scale and small-scale turbulence. *J Fluid Mech* 1999;384:107–32.
- [31] Peters N. A spectral closure for premixed turbulent combustion in the flamelet regime. *J Fluid Mech* 1992;242:611–29.
- [32] Hawkes ER, Cant RS. Implications of a flame surface density approach to large eddy simulation of premixed turbulent combustion. *Combust Flame* 2001;126:1617–29.
- [33] Weller HG, Tabor G, Gosman AD, Fureby C. Application of a flame wrinkling LES combustion model to a turbulent mixing layer. *Proc Combust Inst* 1998;27:899–907.
- [34] Charlette F, Meneveau C, Veynante D. A power law flame wrinkling model for LES of premixed turbulent combustion Part I—non-dynamic formulation and initial tests. *Combust Flame* 2002;131:159–80.
- [35] Pitsch H. A consistent level set formulation for large-eddy simulation of premixed turbulent combustion. *Combust Flame* 2005; 143:587–98.
- [36] Pope SB, Cheng WK. Statistical calculations of spherical turbulent flames. *Proc Combust Inst* 1986;21:1473–81.
- [37] Lipatnikov AN, Chomiak J. Turbulent flame speed and thickness: phenomenology, evaluation, and application in multi-dimensional simulations. *Progr Energy Combust Sci* 2002;28(1):1–74.
- [38] Zimont VL, Battaglia V. Joint RANS/LES approach to premixed flame modeling in the context of the TFC combustion model. *Flow Turb Combust* 2006;77:305–31.
- [39] Lindstedt RP, Vaos EM. Modeling of premixed turbulent flames with second moment methods. *Combust Flame* 1999; 116:461.
- [40] Mongia HC, Held TJ, Hsiao GC, Pandalai RP. Challenges and progress in controlling dynamics in gas turbine combustors. *J Propul Power* 2003;19:822–9.
- [41] Lipatnikov AN, Chomiak J. Molecular transport effects on turbulent flame propagation and structure. *Progr Energy Combust Sci* 2005;31:1–73.
- [42] Bradley D. How fast can we burn? *Proc Combust Inst* 1992;24: 247–53.
- [43] Abdel-Gayed RG, Bradley D, Hamid MN, Lawes M. Lewis number effects on turbulent burning velocity. *Proc Combust Inst* 1984;20: 505–12.
- [44] Gulder OL, Smallwood GJ, Wong R, Snelling DR, Smith R, Deschamps BM, et al. Flame front surface characteristics in turbulent premixed propane/air combustion. *Combust Flame* 2000;120:407–19.
- [45] Kadewaki S, Hasegawa T. Numerical simulations of dynamics of premixed flames: flame instability and vortex–flame interaction. *Prog Energy Combust Sci* 2005;31:193–241.
- [46] Veynante D, Vervisch L. Turbulent combustion modeling. *Prog Energy Combust Sci* 2002;28:193–266.
- [47] Pitsch H. Large-eddy simulation of turbulent combustion. *Annu Rev Fluid Mech* 2006;38:453–82.
- [48] Poinsot T, Candel S, Trouve A. Applications of direct numerical simulation to premixed turbulent combustion. *Prog Energy Combust Sci* 1995;21(6):531–76.
- [49] Law CK, Sung CJ. Structure, aerodynamics, and geometry of premixed flamelets. *Progr Energy Combust Sci* 2000;26:459–505.
- [50] Williams FA. Progress in knowledge of flamelet structure and extinction. *Progr Energy Combust Sci* 2000;26:657–82.
- [51] Poinsot T, Echekki T, Mungal MG. A study of the laminar flame tip and implications for premixed turbulent combustion. *Combust Sci Technol* 1992;81:45–59.
- [52] Ghenni C, Gouldin FC, Golokalp I. Mass flux measurements for burning rate determination of premixed turbulent flames. *Proc Combust Inst* 1998;27:979–87.
- [53] Filatyev SA, Driscoll JF, Carter CD, Donbar JM. Measured properties of turbulent premixed flames for model assessment, including burning velocities, stretch rates and surface densities. *Combust Flame* 2005;141:1–21.
- [54] Mansour MS, Peters N, Chen Y-C. Investigation of scalar mixing in the thin reaction zones regime using a simultaneous CH-LIF/Rayleigh laser technique. *Proc Combust Inst* 1998;27: 767–73.
- [55] Ayoola BO, Balachandran R, Frank JH, Mastorakos E, Kaminski CF. Spatially resolved heat release rate measurements in turbulent premixed flames. *Combust Flame* 2006;144:1–16.
- [56] Meier W, Duan XR, Weigand P. Reaction zone structures and mixing characteristics of partially premixed swirling CH<sub>4</sub>-air flames in a gas turbine model combustor. *Proc Combust Inst* 2005;30: 835–42.
- [57] Shepherd IG, Cheng RK, Plessing T, Kortschik C, Peters N. Premixed flame front structure in intense turbulence. *Proc Combust Inst* 2002;29:1833–40.
- [58] Cheng RK, Shepherd IG, Bedat B, Talbot L. Premixed turbulent flame structures in moderate and intense isotropic turbulence. *Combust Sci Technol* 2002;174:29–59.
- [59] Lachaux T, Halter F, Chauveau C, Gokalp I, Shepherd IG. Flame front analysis of high pressure turbulent lean premixed methane air flames. *Proc Combust Inst* 2005;30:819–26.
- [60] Shepherd IG, Cheng RK, Goix PJ. The spatial scalar structure of premixed turbulent stagnation point flames. *Proc Combust Inst* 1990;23:781–7.
- [61] Buschmann A, Dinkelacker F, Schafer T, Schafer M, Wolfrum J. Measurement of the instantaneous detailed flame structure in turbulent premixed combustion. *Proc Combust Inst* 1996;26:437–45.
- [62] Dinkelacker F, Soika A, Most D, Hofmann D, Leipertz A, Polifke W, et al. Structure of locally quenched highly turbulent lean premixed flames. *Proc Combust Inst* 1998;27:857–65.
- [63] Soika A, Dinkelacker F, Leipertz A. Measurement of the resolved flame structure of turbulent premixed flames with constant Reynolds number and varied stoichiometry. *Proc Combust Inst* 1998;27:785–92.
- [64] Soika A, Dinkelacker F, Leipertz A. Pressure influence on the flame front curvature of turbulent premixed flames: comparison between experiment and theory. *Combust Flame* 2003;132:451–62.
- [65] Dinkelacker F. Experimental validation of flame regimes for highly turbulent premixed flames. In: Proceedings of European Combustion Meeting (ECM2003) of The Combustion Institute, 2003. p. 158–64.
- [66] Chen Y-C, Bilger RW. Experimental investigation of three dimensional flame front structure in premixed turbulent combustion-I:

- hydrocarbon air Bunsen flames. *Combust Flame* 2002;131: 400–35.
- [67] Chen Y-C, Bilger RW. Experimental investigation of three dimensional flame front structure in premixed turbulent combustion—II: lean hydrogen air Bunsen flames. *Combust Flame* 2004; 138:155–74.
- [68] Chen Y-C, Bilger RW. Detailed measurements of local scalar front structures in stagnation type turbulent premixed flames. *Proc Combust Inst* 2005;30:801–8.
- [69] Chen Y-C, Kalt PAM, Bilger RW, Swaminathan N. Effects of mean flow divergence on turbulent scalar flux and local flame structure in premixed turbulent combustion. *Proc Combust Inst* 2002;29: 1863–71.
- [70] O'Young F, Bilger RW. *Combust Flame* 1997;109:682–700.
- [71] Chen Y-C, Peters N, Schneemann GA, Wruck N, Renz U, Mansour MS. The detailed flame structure of highly stretched turbulent premixed methane air flames. *Combust Flame* 1996;107:223–44.
- [72] de Goeij LPH, Plessing T, Hermanns RTE, Peters N. Analysis of the flame thickness of turbulent flamelets in the thin reaction zones regime. *Proc Combust Inst* 2005;30:859–66.
- [73] Steinberg AM, Driscoll JF, Filatov S, Carter CD. High resolution cinema stereo PIV system for the measurement of turbulent flame dynamics, Paper B-13. In: The 5th US Sections meeting of the Combustion Institute, San Diego, CA, 2006.
- [74] Ratner A, Driscoll JF, Donbar JM, Carter CD, Mullin JA. Reaction zone structure of nonpremixed turbulent flames in the intensely wrinkled regime. *Proc Combust Inst* 2000;28:245–51.
- [75] Tanahashi M, Nada Y, Ito Y, Miyuchi T. Local flame structure in the well stirred reactor regime. *Proc Combust Inst* 2002;29: 2041–9.
- [76] Rasmussen CC, PhD thesis University of Michigan, Department of Aerospace Engineering, Ann Arbor, MI, 2006.
- [77] Mueller CJ, Driscoll JF, Reuss D, Drake MC. Vorticity generation and attenuation as vortices convect through a premixed flame. *Combust Flame* 1998;112:342–58.
- [78] Upatnieks A, Driscoll JF, Rasmussen CC, Ceccio SL. Liftoff of turbulent jet flames—assessment of edge flame and other concepts using cinema PIV diagnostics. *Combust Flame* 2004;138:259–72.
- [79] Donbar JM, Driscoll JF, Carter CD. Strain rates measured along the wrinkled flame contour within turbulent nonpremixed jet flames. *Combust Flame* 2001;125:1239–57.
- [80] Deschamps BM, Smallwood GJ, Prieur J, Snelling DR, Gülder OL. Surface density measurements of turbulent premixed flames. *Proc Combust Inst* 1996;26:427–39.
- [81] Lee GG, Huh KY, Kobayashi H. Measurement and analysis of flame surface density for turbulent premixed combustion on a nozzle-type burner. *Combust Flame* 2000;122:43–57.
- [82] Shepherd I. Flame surface density and burning rate in premixed turbulent flames. *Proc Combust Inst* 1996;26:373–9.
- [83] Veynante D, Duclos JM, Piana J. Experimental analysis of flamelet models for premixed turbulent combustion. *Proc Combust Inst* 1994;25:1249–56.
- [84] Renou B, Mura A, Samson E, et al. Characterization of the local flame structure and the flame surface density for freely propagating premixed flames at various Lewis numbers. *Combust Sci Technol* 2002;174:143–79.
- [85] Shy SS, Lee EI, Chang NW, et al. Direct and indirect measurements of flame surface density, orientation, and curvature for premixed turbulent combustion modeling in a cruciform burner. *Proc Combust Inst* 2000;28:383–90.
- [86] Lee SY, Seo S, Broda JC, Pal S, Santoro RJ. An experimental estimation of mean reaction rate and flame structure during combustion instability in a lean premixed gas turbine combustor. *Proc Combust Inst* 2000;28:775–80.
- [87] Domingo P, Vervisch L, Payet S, et al. DNS of a premixed turbulent V flame and LES of a ducted flame using a FSD-PDF subgrid scale closure with FPI-tabulated chemistry. *Combust Flame* 2005;143: 566–86.
- [88] Boger M, Veynante D, Bouhanem H, Trouve A. Direct numerical simulation analysis of flame surface density concept. *Proc Combust Inst* 1998;27:917–23.
- [89] Chakraborty N, Cant RS. Effects of strain rate and curvature on surface density function transport in turbulent premixed flames in the thin reaction zone regime. *Phys Fluids* 2005;17: 065108.
- [90] Knikker R, Veynante D, Meneveau C. A dynamic flame surface density model for large eddy simulation of turbulent premixed combustion. *Phys Fluids* 2004;16(11):L91.
- [91] Tang BHY, Chan CK. Simulation of flame surface density and burning rate of a premixed turbulent flame using contour advection. *Combust Flame* 2006;147:49–66.
- [92] Lam JSL, Chan CK, Talbot L, et al. On the high-resolution modeling of a turbulent premixed open V-flame. *Combust Theory Model* 2003;7:1–28.
- [93] Hinze JO. *Turbulence*. New York: McGraw-Hill; 1975.
- [94] Goix P, Paranthoen P, Trinite M. A tomographic study of measurements in a V-shaped H<sub>2</sub> air flame and a lagrangian interpretation of the turbulent flame brush evolution. *Combust Flame* 1990;81:229–41.
- [95] Bell JB, Day MS, Grcar JF. Numerical simulation of premixed turbulent methane combustion. *Proc Combust Inst* 2002;29:1987–93.
- [96] Hawkes ER, Chen JH. Comparison of direct numerical simulation of lean premixed methane-air flames with strained laminar flame calculations. *Combust Flame* 2006;144:112–25.
- [97] Kerstein AR, Ashurst WT, Williams FA. Field equation for interface propagation in an unsteady homogeneous flow field. *Phys Rev A* 1988;37(7):2728–31.
- [98] Sivashinsky GI. Non-linear analysis of hydrodynamic instability in laminar flames. 1. derivation of basic equations. *Acta Astronaut* 1977;4:1177–206.
- [99] Ashurst WT. On flame propagation through periodic flow fields. *Combust Sci Technol* 1991;80:159.
- [100] Peters N, Wenzel H, Williams FA. Modification of the turbulent burning velocity by gas expansion. *Proc Combust Inst* 2000;28:235–43.
- [101] Paul RN, Bray KNC. Study of premixed turbulent combustion including Landau-Darrius instability effects. *Proc Combust Inst* 1996;26:259–66.
- [102] Aung KT, Tzeng L-K, Ismail MA, Faeth GM. Response to comment by S.C. Taylor and D.B. Smith on laminar burning velocities and Markstein numbers of hydrocarbon/air flames. *Combust Flame* 1995;102:526–30.
- [103] Bradley D, Gaskell PH, Gu XJ. Burning velocities, Markstein lengths, and flame quenching for spherical methane-air flames: a computational study. *Combust Flame* 1996;104:176–98.
- [104] Echekki T, Mungal MG. Flame speed measurements at the tip of a slot burner: effects of flame curvature and hydrodynamic stretch. *Proc Combust Inst* 1990;23:455.
- [105] Durox D, Dueruix S, Candel S. Experiments on collapsing cylindrical flames. *Combust Flame* 2001;125:982.
- [106] Tzeng L-K, Ismail MA, Faeth GM. Laminar burning velocities and Markstein numbers of hydrocarbon/air flames. *Combust Flame* 1993;95:410–26.
- [107] Palm-Leis A, Strehlow RA. On the propagation of turbulent flames. *Combust Flame* 1969;13:111–29.
- [108] Ibarreta AF, Driscoll JF, Feikema DA. Markstein numbers of negatively stretched premixed flames: microgravity measurements and computations. *Proc Combust Inst* 2002;29: 1435–43.
- [109] Sun CJ, Sung CJ, He L, Law CK. Dynamics of weakly stretched flames: quantitative description and extraction of global flame parameters. *Combust Flame* 1999;118:108–28.
- [110] Wu MS, Kwon S, Driscoll JF, Faeth GM. Turbulent premixed hydrogen-air flames at high Reynolds numbers. *Combust Sci Technol* 1990;73:327–50.

- [111] Im HG, Chen JH. Preferential diffusion effects on the burning rate of interacting turbulent premixed hydrogen-air flames. *Combust Flame* 2002;131:246–58.
- [112] Bell JB, Cheng RK, Day MS, Shepherd IG. Numerical simulation of Lewis number effects on lean premixed turbulent flames. *Proc Combust Inst* 2006;31:1309–17.
- [113] Hawkes ER, Chen JH. Direct numerical simulation of hydrogen-enriched lean premixed methane-air flames. *Combust Flame* 2004;138:242–58.
- [114] Chen JH, Echekki T, Kollmann W. The mechanism of two dimensional pocket formation in lean premixed methane-air flames with implications to turbulent combustion. *Combust Flame* 1999;116:15–48.
- [115] Chen JH, Im HG. Stretch effects on the burning velocity of turbulent premixed hydrogen/air flames. *Proc Combust Inst* 2000;28:211–8.
- [116] Peters N, Terhoeven P, Chen JH, Echekki T. Statistics of flame displacement speeds from computations of 2-D unsteady methane air flames. *Proc Combust Inst* 1998;27:833–9.
- [117] Rutland CJ, Trouve A. Direct numerical simulation of premixed turbulent flames with nonunity Lewis numbers. *Combust Flame* 1993;94:41–57.
- [118] Sinibaldi JO, Mueller CJ, Driscoll JF. Local flame propagation speeds along wrinkled unsteady stretched premixed flames. *Proc Combust Inst* 1998;27:827–32.
- [119] Cheng RK, Shepherd IG. The influence of burner geometry on premixed turbulent flame propagation. *Combust Flame* 1991;85:7–26.
- [120] Cheng RK, Shepherd IG. Intermittency and conditional velocities in premixed conical turbulent flames. *Combust Sci Technol* 1987;52:353–75.
- [121] Gulder OL, Smallwood GJ, Wong R, Snelling DR, Smith R, Deschamps BM, et al. Flame front surface characteristics in turbulent premixed propane/air combustion. *Combust Flame* 2000;120:407–16.
- [122] Kobayashi H, Seyama K, Hagiwara H, Ogami Y. Burning velocity correlation of methane/air turbulent premixed flames at high pressure and high temperature. *Proc Combust Inst* 2005;30:827–34.
- [123] Bedat B, Cheng RK. Experimental study of premixed flames in intense isotropic turbulence. *Combust Flame* 1995;100:485–94.
- [124] Cheng RK, Shepherd IG, Talbot L. Reaction rates in premixed turbulent flames and their relevance to the turbulent burning speed. *Proc Combust Inst* 1988;22:771–80.
- [125] Bourguignon E, Kostiuk LW, Michou Y, Gokalp I. Experimentally measured burning rates of premixed turbulent flames. *Proc Combust Inst* 1996;26:447–52.
- [126] Smallwood GJ, Gulder OL, Snelling DR, Deschamps BM, Gokalp I. Characterization of flame front surfaces in turbulent premixed methane/air combustion. *Combust Flame* 1995;101:461–70.
- [127] Yoshida A, Gunther R. Experimental investigation of thermal structure of turbulent premixed flames. *Combust Flame* 1980;38:249–58.
- [128] Kobayashi H, Tamura T, Maruta K, Niioka T, Williams F. Burning velocity of turbulent premixed flames in a high pressure environment. *Proc Combust Inst* 1996;26:389–96.
- [129] Karlovitz B, Denniston D, Wells F. Investigation of turbulent flames. *J Chem Phys* 1951;19(5):541–7.
- [130] Hottel HC, Williams GC, Levine RS. The influence of isotropic turbulence on flame propagation. *Proc Combust Inst* 1953;4:636–44.
- [131] Driscoll JF, Gulati A. Measurement of various terms in the turbulent kinetic energy balance within a flame and comparison with theory. *Combust Flame* 1988;72:131–52.
- [132] Cheng RK. Velocity and scalar characteristics of premixed turbulent flames stabilized by weak swirl. *Combust Flame* 1995;101:1–14.
- [133] Cho P, Law CK, Hertzberg JR, Cheng RK. Structure and propagation of turbulent premixed flames stabilized in a stagnation flow. *Proc Combust Inst* 1986;21:1493–9.
- [134] Cheng RK, Ng TT. On defining the turbulent burning velocity in premixed V-shaped turbulent flames. *Combust Flame* 1984;57:155–67.
- [135] Namazian M, Shepherd IG, Talbot L. *Combust Flame* 1997;108:349.
- [136] Bradley D, Haq MZ, Hicks RA, Kitagawa T, Lawes M, Sheppard CGW, et al. Turbulent burning velocity, burned gas distribution, and associated flame surface definition. *Combust Flame* 2003;133:415–30.
- [137] Cheng RK. Workshop on premixed turbulent combustion, website: <<http://eetd.lbl.gov/aet/combustion/workshop/Mainz/10thWorkshop.html>> and <<https://cmcs.ca.sandia.gov/cmcs/>>.
- [138] Barlow RS. Turbulent nonpremixed flame workshop website: <<http://www.ca.sandia.gov/TNF/>>.
- [139] He X, Zigler BT, Walton SM, Wooldridge MS, Atreya A. A rapid compression facility to study OH time histories during iso-octane ignition. *Combust Flame* 2006;145:552–70.
- [140] Aleiferis PG, Charalambides AG, Hardalupas Y, Taylor AMKP, Urata Y. Autoignition initiation and development of h-heptane HCCI combustion: an optical investigation. SAE paper 2006-01-3273, American Society of Automotive Engineers.
- [141] Huang J, Hill PG, Bushe WK, Munshi SR. Shock-tube study of methane ignition under engine-relevant conditions: experiments and modeling. *Combust Flame* 2004;136:25–42.
- [142] Hult J, Richter M, Nygren J, Alden M, Hultqvist A, Christensen M, et al. Application of a high-repetition-rate laser diagnostic system for single-cycle-resolved imaging in internal combustion engines. *Appl Opt* 2002;41:24–9.
- [143] Trautwein SE, Grudno A, Adomeit G. The influence of turbulence intensity and laminar flame speed on turbulent flame propagation under engine like conditions. *Proc Combust Inst* 1990;23:723–8.
- [144] Bracco FV. Structure of flames in premixed charge IC engines. *Combust Sci Technol* 1988;58:209–30.
- [145] Dec JE, Coy EB. OH radical imaging in a DI diesel engine and the structure of the early diffusion flame. *Soc Automot Eng* 1996: SAE paper 9608311996.
- [146] Vaughn CB, Su WH, Howard JB, Longwell JP. Measurements and modeling of light hydrocarbons in rich C<sub>2</sub>H<sub>4</sub> combustion in a jet-stirred reactor. *Combust Flame* 1991;84:38–46.
- [147] Blust JW, Ballal DR, Sturgess GJ. Fuel effects on lean blowout and emissions from a well-stirred reactor. *J Propul Power* 1999;15:216–23.
- [148] Rutar T, Malte PC, Kramlich JC. Investigation of NO<sub>x</sub> and CO formation in lean premixed, methane air, high intensity, confined flames at elevated pressures. *Proc Combust Inst* 2000;28:2435–41.
- [149] Weber R, Orsino S, Lalleman N, Verlaan A. Combustion of natural gas with high-temperature air and large quantities of flue gas. *Proc Combust Inst* 2000;28:1315–21.
- [150] Plessing T, Peters N, Wunning G. Laser optical investigation of highly preheated combustion with strong exhaust gas recirculation. *Proc Combust Inst* 1998;27:3197–204.
- [151] Bilger RW, Yip B, Long MB, Masri A. An atlas of QEDR flame structures. *Combust Sci Technol* 1990;72:137–49.
- [152] Wunning JA, Wunning JG. Flameless oxidation to reduce thermal NO formation. *Progr Energy Combust Sci* 1997;23:81–92.
- [153] Cavaliere A, de Joannon M. Mild combustion. *Progr Energy Combust Sci* 2004;30:329–66.
- [154] Roberts WL, Driscoll JF, Drake MC, Goss LP. Images of the quenching of a flame by a vortex—to quantify regimes of turbulent combustion. *Combust Flame* 1993;94:58–69.